COMMERCIAL BUILIDNG THERMAL MASS PRECOOLING FOR CONDITIONING LOAD REDUCTION UNDER THE OPERATIVE TEMPERATURE METRIC

by

Christopher Raghubar

BSc, Southern Alberta Institute of Technology, 2016

A thesis

presented to Ryerson University

in partial fulfillment of the

requirements for the degree of

Master of Applied Science

in the program of Building Science

Toronto, Ontario, Canada, 2019

AUTHOR'S DECLARATION FOR ELECTRONIC SUBMISSION OF A THESIS

I hereby declare that I am the sole author of this thesis. This is a true copy of the thesis, including any required final revisions, as accepted by my examiners.

I authorize Ryerson University to lend this thesis to other institutions or individuals for the purpose of scholarly research

I further authorize Ryerson University to reproduce this thesis by photocopying or by other means, in total or in part, at the request of other institutions or individuals for the purpose of scholarly research.

I understand that my thesis may be made electronically available to the public.

COMMERCIAL BUILIDNG THERMAL MASS PRECOOLING FOR CONDITIONING LOAD REDUCTION UNDER THE OPERATIVE TEMPERATURE METRIC

By

Christopher Raghubar

Master of Applied Science – Building Science, 2019

Ryerson University, Toronto, Canada

Abstract

Building thermal mass precooling is highly variable due to the uncertainty of the convective heat transfer coefficient, and current research neglects the radiative cooling effects of reduced interior surface temperatures. The research presented aims to address the shortcomings of current research by modelling night ventilation through concrete slab hollow cores, increasing confidence in the heat transfer coefficient estimate; and modelling the operative temperature experienced by an occupant in an open office with simplified geometry. The cooling load of a baseline non-ventilated slab was determined through a custom numerical model and the operative temperature of the baseline was assigned to the same model with hollow core slab ventilation to determine the ambient air setpoint temperature associated cooling load. The ventilated model was found to achieve 35% cooling energy savings compared to the baseline, with compromised occupant comfort in the early morning, and improved occupant comfort for the rest of the day.

Acknowledgements

I'd like to express my deepest gratitude to my friends and family for supporting me throughout this endeavour and tolerating my constant talk of activated thermal mass and Fanger's comfort theory.

I would also like to thank Dr. Damien David and Dr. Frédéric Kuznik for welcoming me to INSA Lyon and providing instrumental support in applied heat transfer. This work would not be possible without you.

Finally, to my supervisor Dr. Umberto Berardi and my review committee, thank you for your support and guidance.

Table of Contents

List of Figures

List of Tables

Nomenclature

Variable	Unit	Description
α	m^2/s	Thermal Diffusivity
β	$1/K$	Coefficient of Thermal Expansion
δ	M	Characteristic length
ε	-	Emissivity
η	K	Degree of charging
μ	m^2/s	Dynamic Viscosity
ν	$m^5/kg\,s$	Kinematic Viscosity (μ/ρ)
ρ	kg/m^3	Density
σ		Stefan-Boltzmann constant (5.67×10^{-8})
A	m^2	Area
Bi	-	Biot Number
c_p	$J/kg\,K$	Specific Heat Capacity
E	W/m^2	Irradiance
F_v or $F_{j\rightarrow i}$	-	View Factor
G	W	Gains (internal, solar, etc)
Gr	-	Grashof Number
h	$W/m^2\,K$	Heat Transfer Coefficient
H	m	Height
J	W/m^2	Radiosity
k	$W/m\,K$	Thermal Conductivity
l	M	Length
$\dot{m}$	kg/s	Mass flow rate
M	W/m^2	Radiation
Nu	-	Nusselt Number
P	W/m^2	Power
Pr	-	Prandtl Number
Q	W/m^2	Heat Flux
q	$J/s\,K$	Energetic flow rate ($\dot{m}c_p$)
R	$m^2\,K/W$	Thermal Resistance
Re	-	Reynolds Number
T	K	Temperature
t	s	Time
U	$W/m^2\,K$	Heat Transfer Coefficient of Assembly
V	m^3	Volume
v	m/s	velocity
x	m	x-direction

1.0: Introduction/Motivation for Research

Space conditioning accounts for over 40% of energy consumption in buildings, and accounts for 15% of overall energy consumption in the US (Thompson, 2011). Coupled with the effects of climate change and recent trends towards sustainability, there is an urgent demand to reduce our energy consumption.

Passive design provides an opportunity to reduce the conditioning load of buildings through the use of solar energy, free cooling, and thermal mass, among others. These passive strategies can be coupled with active technology such as sensors and fans to fully exploit the potential of the passive system. In the case of cooling, heat from internal gains, solar radiation, and transmission though the building envelope must be purged by the cooling system in order to achieve the desired interior air temperature. Conventionally, these heat sources are matched by the cooling system, essentially removing the same amount of energy that was introduced to the interior environment in order to achieve thermal equilibrium. However, it is possible to store this energy in the building mass during occupancy and purge it to the external environment at night when temperatures are comparatively cooler, reducing the amount of cooling required during the day and providing a free cooling source at night.

Environment as Heat Source/ Sink

The built world exists in a diurnal environment experiencing high air temperatures and solar radiation during the day, and reduced temperatures with zero solar radiation at night. Similarly, many occupied buildings experience diurnal occupancy – commercial buildings are typically occupied during the day during business hours, and residential buildings are typically occupied at night outside of business hours. This results in the majority of the conditioning load occurring primarily during the day for commercial buildings, and at night for residential buildings. Considering that the exterior temperature is typically higher than the desired interior air temperature and that occupants as well as equipment act as heat sources in the interior space, commercial buildings are well suited to storing excess thermal energy during the day and purging it to the exterior at night. Conversely, residential buildings are more suited to absorbing solar gains during the day and re-emitting them to the interior at night when temperatures might drop below the desired ambient air temperature. The exterior environment acts as an inexhaustible heat source during the day, and an infinitely large heat sink at night.

Building as Thermal Capacitor

Due to the immense dead and live loads imposed on occupied structures, buildings are inherently constructed from heavyweight materials including steel and concrete. Although these materials contribute to the dead load of the structure and thus necessitate supporting its own self weight, the high thermal mass of these materials can be exploited to store and release thermal energy as desired, increasing the utility of the system.

Exterior Air as a Heat Transfer Fluid

Given the ability of air to move freely as a fluid, the exterior air can act as a heat transfer fluid (HTF) if it is directed by a fan to the hollow core heat transfer path. The fan-controlled velocity allows for augmentation of the heat transfer rate between the heat sink/source and HTF, facilitating control over the heat transfer rate.

Coupling the exterior heat sink/source with the building mass thermal capacitor via the exterior air HTF creates as complete thermal network in which the heat transfer rate from the building to the exterior can be effectively evaluated and controlled (to some degree) though the HTF mass flow rate.

2.0: Literature Review

2.1: Thermal Mass in Buildings

Thermal mass has been used to achieve occupant comfort for as long as humans have sought shelter, and since well before high performance enclosures and active building systems have been used. Early primitive humans resided in caves to shelter from not only precipitation but also the extreme hot and cold of the outdoors; and ancient civilizations lived in man-made dwellings constructed primarily out of stone and masonry. The heavyweight materials used in these early shelters have inherently high specific heat capacities, allowing for a large amount of thermal energy to be stored for a small increase in material temperature. This allowed early shelters to absorb solar radiation during the day and release it to the outdoors at night, keeping the shelter cool in the summer; as well as absorb occupant-borne and solar thermal gains during the day and release it at night when the temperature is comparatively cooler, keeping the shelter warm in the winter.

Storing and releasing thermal energy in accordance with fluctuating exterior temperatures allows for daily and annual interior temperature ranges to be tempered, contributing to occupant comfort without the use of an active conditioning system. This can be leveraged in modern building systems where the quantity of thermal storage can be controlled using active building systems and systems integration to minimize the energy required to achieve occupant comfort.

The use of thermal mass in buildings to reduce energy consumption and conditioning energy costs associated with time of use pricing for electricity has been extensively evaluated by Braun in a review (Braun J. E., 2003), where a method for determining optimal temperature setpoints is presented, and past works of the author and other authors are contrasted and compared. Cited in this work is a simulated study (Braun J. E., 1990) in which a building is “optimally cooled” – referring to a method that cools the building during the unoccupied night period in order to precool the building thermal mass, then allows the building to rise in temperature prior to occupancy. This contrasts the conventional “night setup” method in which the building is allowed to rise in temperature during the unoccupied night period (essentially preheating the building thermal mass), then cooling the building prior to occupancy. The simulation found total energy costs savings to be 0 – 35% and peak electrical demand reduction potential to be 15 – 25% and 30 – 35% for lightweight and heavyweight constriction respectively, as seen in Fig 2.1.

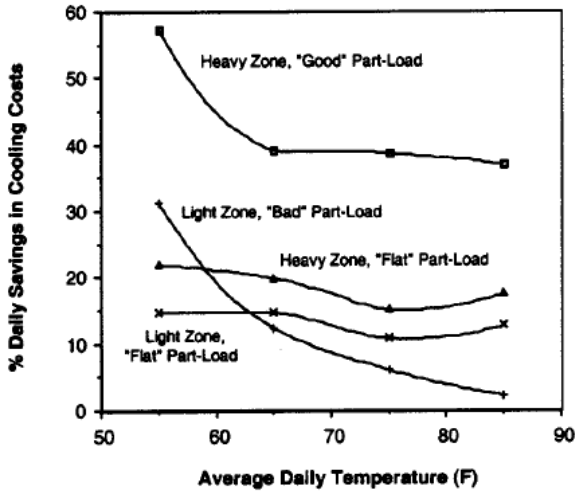

Figure 2.1 – *Average Temperature vs % Cooling Load Savings by Construction Type (Braun J. E., 2003)*

Peak load reduction through night precooling was also simulated in (Rabl & Norford, 1991), finding that peak load can be reduced by 10 – 20% depending on the cooling duration; and up to 50% (Andresen & Brandemuehl, 1992) when optimal convection between the air and thermal mass occurs. Agreeing with Braun (1990), Snyder and Newall (1990) found the optimally cooled model could reduce cooling costs by 18% compared to the night setup model. The simulated studies revealed that heavyweight buildings are more suited to night cooling than lightweight buildings, and that optimal cooling yields reduced total energy consumption and peak cooling demand, resulting in reduced cooling costs (Braun J. E., 2003).

A laboratory experiment of night cooling was performed by Morris et al. (1994) in which a building was cooled to below the occupant comfort range during the unoccupied period, then allowed to rise in temperature to the occupant comfort range just prior to occupancy; essentially precooling the building mass. Compared to the night setup approach, precooling was found to reduce both total cooling load and peak cooling demand by 40%. Evaluation of night cooling in a laboratory setting was also conducted (Braun, Lawrence, Klaassen, & House, 2002) considering the building's interior environment interaction with the exterior environment, including temperature difference, solar radiation, etc. Considering interior, south, east, and west zone locations and orientations of zones, the study found that cooling load reductions can be achieved in the range of 18 – 31%, and peak cooling demand reductions in the range of 3 – 15%.

Given the effects of thermal coupling discussed above, a Chicago field study (Keeney & Braun, 1997) compared the thermal behaviour of a building employing precooling against that of a building using a conventional night setup during a power outage. The study found that the building employing precooling only required the chiller to work at 75% capacity after a 20-minute loss of power to the chiller, compared to the chiller working at 100% in the case of the building without precooling. This not only results in reduced energy consumption associated with cooling, but also decreases the energy required per unit of cooling as the cooling systems operates at a higher efficiency. Furthermore, the precooled building maintained a consistent thermal comfort rating (PMV = 0.20) during the duration of the occupied period, suggesting that targeting a dynamic thermal comfort rating within the acceptable range of ($-0.50 < PMV < 0.50$) would result in further reduced peak load demand (Braun J. E., 2003).

The results of the Chicago field study were modelled by Braun et al. (2001) to determine how interior setpoints strategies affect cooling demand, and thus cooling cost based on time of use pricing in Chicago. The study explored 6 “cooling energy” release strategies and found savings of 17 – 22% for methods using interior setpoints primarily at 23°C. One method achieved a cost savings of over 40%, however, the interior setpoint was set at 25°C, compromising occupant comfort. The study was repeated with time of use pricing in Boston, Miami, Phoenix, and Seattle to determine the effects of location-based time of use pricing on total cooling cost. It was found that savings is directly proportional to the peak to off-peak ratio, and that locations with peak rates equal to off peak rates could experience negative savings (increased costs) as occurred in Seattle. This suggests that the night cooling strategy consumes greater energy than that of the regular night setup in the Seattle climate, also suggesting that cooler climates are less suited to night cooling.

The review conducted by Braun (2003) found that savings in terms of cost and energy are dependent on the type of mechanical system used and its ability to vary cooling demand as necessary; utility rate structuring; occupancy; desired comfort; as well as type of construction. Ultimately, large heavyweight buildings occupied during peak period pricing and situated in broad time of use pricing locations are ideal candidates for night precooling.

Zhang et al. (2006) evaluated thermal conductivity in conjunction with heat capacity under the constraint of time to determine ideal material properties yielding minimal “integrated discomfort degree hours” (seasonal sum of difference between average hourly temperature and setpoint temperature) outside the occupant comfort range in the absence of an active conditioning system. The energy balance of the analyzed room considered conduction through the wall, as well as interior and

exterior convection and radiation; and yielded interior conditions (described in terms of degree-hours of discomfort in summer and winter) based on varying material properties (conductivity and heat capacity) on the exterior and interior face of the wall assembly. The study found that foremost, the heat capacity of the assembly must be sufficiently large to absorb the excess enthalpy delivered to the system. If the heat capacity isn't sufficiently large, thermal conductivity has little effect on discomfort degree-hour minimization due to a lack of storage capacity once the energy is conducted through the material. Similarly, if the heat capacity of the assembly is sufficiently large, thermal conductivity has a significant effect on degree-hour minimization as it dictates the rate at which energy can be absorbed and stored by the system. The study also resolved that low conductivity materials at better suited for exterior applications, and high conductivity materials are more suited for interior applications. From this, the ideal volumetric heat capacity was found to be 50 $MJ/m^3*°C$ to optimize free cooling of a building, and 100 $MJ/m^3*°C$ to optimize year-long conditioning (heating and cooling).

The results of the parametric assessment of heat capacity and thermal conductivity discussed above was applied to a simplified model (Zeng, Wang, Di, Jiang, & Zhang, 2011) in order to determine the ideal specific heat capacity as a function of temperature, given that density is essentially constant in the temperature range explored. Performance was measured using the integrated discomfort degree metric used in the original study. As in the original, the required heat capacity of the system was defined as equal to the excess enthalpy that the system experiences, and excess enthalpy was distributed within a temperature range equal to the thermal comfort range such that that ambient air temperature does not exceed or fall below the upper and lower temperature limits for summer and winter respectively. The study found that the ideal volumetric specific heat for free cooling is 80 MJ/m^3 at 26.75°C, and 220 MJ/m^3 at 19.3°C. This reveals that the ideal behaviour of volumetric specific heat is similar to that of the phase change process in which a system is capable of absorbing and releasing energy with no change in system temperature.

A theoretical and experimental study was conducted by Ulgen in (2002) on various wall assembly types for maximizing the cooling load time shift (difference in time of peak load occurring) and amplitude reduction (decrease in peak load) for daily sine function temperature fluctuations (outlined in Figure 2.4), considering thermal conductivity, specific heat capacity, density and mass of material. The study found that both increases in mass density and specific heat of a material improve the thermal performance of wall assemblies, however, optimal conductance for maximized cooling load time shift and amplitude reduction is dependent on the wall assembly composition as well as surrounding

environmental conditions. This is due to the tendency of increased heat transfer through conduction to increase the amount of energy that can be stored in a given timestep, but also increase the amount of energy that can be conducted through the material. The authors concluded that wall assemblies of high mass density and specific heat capacity with small thermal diffusivity yield the best interior conditions. Moreover, buildings that experience diurnal occupancy are more suited to single layer wall assemblies and lower thermal energy storage (TES), while buildings that experience continuous occupancy are more suited to layered wall assemblies and higher energy storage.

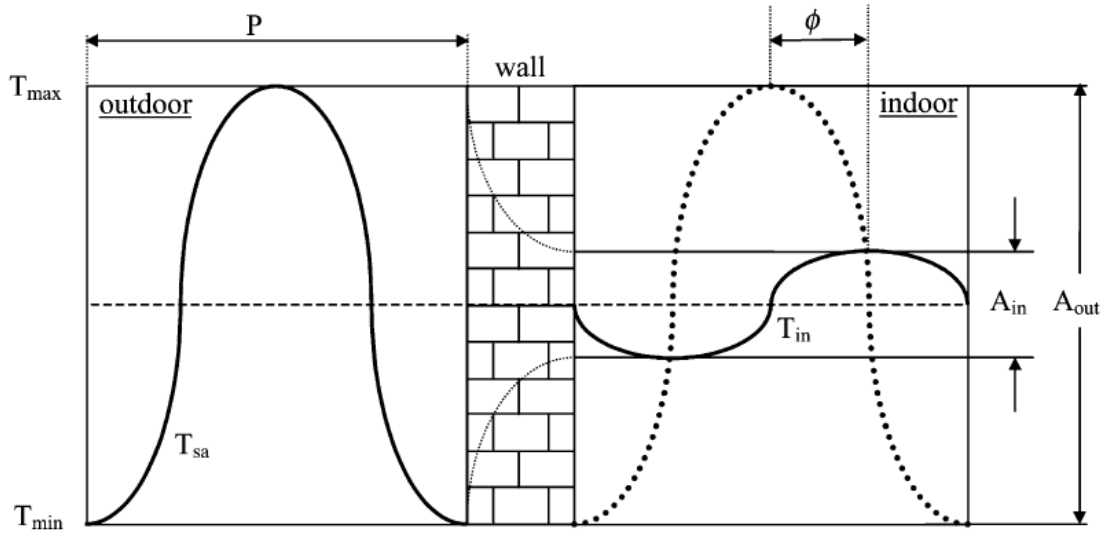

***Figure 2.2**: Peak Load Shift and Amplitude Decrement (Ulgen, 2002)*

A review of peak load shifting using various TES techniques was conducted by Sun et al. (2013) where the authors explore thermal management systems including building thermal mass (BTM) and phase change material (PCM), among others. The BTM method found that simulated precooling of a building can reduce peak loading by 30% in a 5-hour on peak period as reported in (Braun J. E., 1990), (Keeney & Braun, 1997) and (Braun & Kyoung-Ho, 2006). A small, lightweight commercial building was modelled by Lee and Braun (2004) using a simplified thermal network that is typical to that of the building type being explored, and found that peak cooling loads can be reduced by 25 – 45% using precooling depending on the start time and duration of the on-peak period. This building simulated in (Lee & Braun, 2004) was experimentally studied in (Lee & Braun, 2006) and found that the peak cooling load was reduced by 30% in a 5 hour on-demand period, agreeing with simulated studies. The PCM method of TES reported almost 20% reduction in peak load and almost 15% reduced annual cooling load though the addition of 10% PCM by weight in concrete sandwich panel walls in a simulated study (Kissock & Limas, 2006), and a numerical study found that night ventilation (free cooling) coupled with

PCM wallboards resulted in almost 30% reduction in peak cooling load when outdoor temperatures are below 18C during ventilation (Stetiu & Feustel, 2014).

It is evident that the use of thermal energy storage in buildings coupled with night ventilation/ free cooling has the potential to reduce cooling load and demand in buildings of sufficient thermal mass and of appropriate use. Lightweight buildings are less suited to thermal energy storage as the thermal capacity of the buildings must be equal to or greater than the excess energy burdened on the system via heat flux though the assembly as well as solar and occupant borne gains. In addition, it can be seen that buildings that experience occupancy during the day are ideally suited to thermal energy storage as excess heat can be absorbed during the day and purged to the outdoors at night. Buildings that experience continuous occupancy are not suited to thermal energy storage due to lack of opportunity to cool below the occupant comfort range, as well as continuous occupant-borne gains.

2.2: Phase Change Material (PCM) in Buildings

Latent TES utilizes the latent heat of fusion and latent heat of vaporization in solid-liquid and liquid-gas phase changes respectively, allowing for a large emission/absorption of thermal energy with little change in temperature. The most common example of phase-change energy storage is that of ice in a beverage, in which the later heat of fusion of water is used to absorb the excess energy from the surroundings, maintaining the phase change temperature of the mixture – in this case, 0C. Although this example considers a phase change region of 0C for water, materials that change phase in the occupant comfort range, referred to as Phase Change Materials (PCMs), can be used to achieve occupant comfort with reduced reliance on active mechanical systems.

PCM TES is especially useful in situations exposed to cyclical temperature profiles with respect to time, such as day/night diurnal temperature swings as well as seasonal temperature oscillation. These temperature changes allow for the thermal mass to be charged during periods of temperature greater than the phase change temperature range (melting; endothermic), and discharged during periods less than the phase change temperature range (solidification; exothermic), resulting in a system temperature within the phase change temperature range while exposed to temperatures outside of said range. This allows the system to continuously experience a temperature within the phase change temperature range while energy is being added or removed from the system.

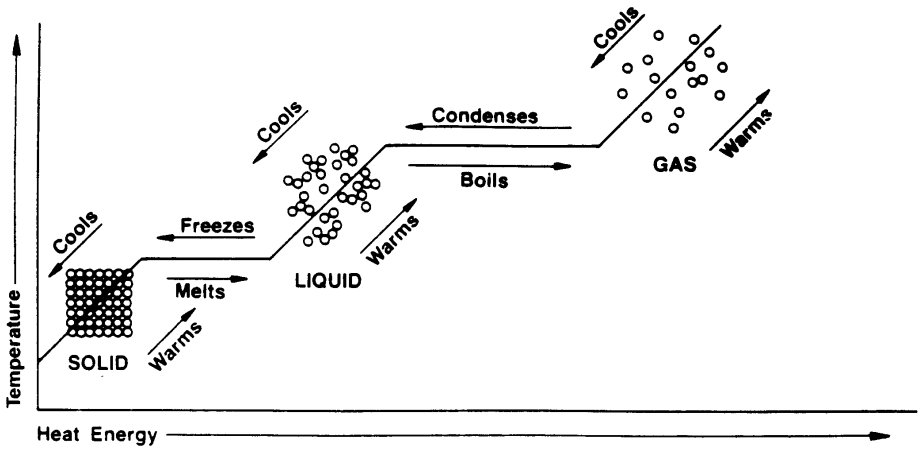

Figure 2.3 – *Phase Change Enthalpy vs Temperature (Eames, 2016)*

As discussed in the previous section, thermal mass in buildings presents an opportunity to attenuate daily and seasonal temperature fluctuations, as well as shift peak loading forward in time (hours for daily; months for seasonal) through thermal inertia. The use of PCMs in building systems increases the thermal mass of the system, as well as introduces the ability to control the amount of energy being stored and released by the mass though the proper selection of PCM properties, including but not limited to phase change temperature range, heat of fusion, thermal conductivity, and quantity of PCM. The selection criteria as well as effects of using PCM as thermal mass in buildings to reduce energy costs and peak loads are discussed herein.

The phase change temperature range of the selected PCM dictates the temperature that is maintained within the space, considering the rate of energy flow with respect to latent heat of fusion and thermal conductivity. In an exploration of passive solar design, Xu et al. (2005) found that optimal melting temperature is dependent on the surrounding climate, especially solar radiation when considering solar heat gain; while Whiffen & Riffat (2012) report that melting temperature should be 1°C to 3°C greater than average ambient air temperature to optimize the benefits of diurnal temperature cycles. Drake (1987) defines optimal melting temperature based on heat flux, heat transfer coefficient, storage time, and weighted average of day and night temperatures.

Apart from appropriate phase change temperature range, the selected PCM must also have sufficient thermal conductivity and heat of fusion for the volume employed in order to absorb the excess energy imposed on the system in the given timeframe. Due to the constraint of time and desire to exploit diurnal temperature cycles, specific heat and thermal conductivity should be as high as possible in order to maximize the amount of energy storage available. In addition to these

thermophysical properties, ideal PCMs must also satisfy kinetic, chemical, and economic criteria outlined in Table 2.1 (Pasupathy A. V., 2008).

PCMs come in a variety of types including organic, inorganic, and eutectics. Organics include paraffins, fatty acids, and ethylene glycol; inorganics include salt hydrates; and eutectics include organic-organic, inorganic-organic, and inorganic-inorganic mixtures. Eutectics combine the benefits of different PCMs to yield a mixture with specific properties designed for its application. Although these mixtures have the benefit of narrow melting temperature range and high volumetric heat capacity, there is lack of thermophysical data available in literature (Whiffen & Riffat, 2012), resulting in a lack of experimental validation. The pros and cons of various types PCMs are summarized in Table 2.2.

Table 2.1: Desirable properties for PCM energy storage in buildings (Pasupathy A. V., 2008)

Property	**Desirable Attribute**
Thermodynamic	1. Melting temperature in the desired operating temperature range 2. High latent heat of fusion per unit volume 3. High specific heat, high density, high thermal conductivity 4. Small volume change during phase change and small vapour pressure at operating temperature to reduce containment problems 5. Congruent melting
Kinetic	1. High nucleation rate 2. High rate of crystal growth/decay
Chemical	1. Chemical stability 2. Reversible freeze/melt cycle 3. No degradation after many freeze/melt cycles 4. Non-corrosive; non-toxic; non-flammable; non-explosive
Economic	1. Low cost 2. Large-scale availability

Table 2.2: Pros and Cons of Various Types of PCM

Organics (Kuznik, David, Johannes, & Roux, 2011)	**Inorganics** (Kuznik, David, Johannes, & Roux, 2011)	**Eutectics** (Pasupathy A. V., 2008)
Pros: 1. Available in large temperature range 2. Lack of supercooling 3. Congruent melting 4. Self-nucleating 5. Compatible with common construction materials 6. No segregation 7. Chemical stability 8. High heat of fusion 9. Safe, non-reactive 10. Recyclable	*Pros*: 1. High volumetric heat capacity 2. Low cost; market availability 3. Narrow phase change temperature range 4. High thermal conductivity 5. Non-flammable	*Pros*: 1. Narrow phase change temperature range 2. Volumetric storage density greater than organics
Cons: 1. Low thermal conductivity as solid 2. Low volumetric heat capacity 3. Flammability	*Cons*: 1. High volume change 2. Supercooling 3. Segregation	*Cons*: 1. Limited data available; use of material new to thermal storage applications

2.3: Ventilation and Thermal Mass (Forced Convection)

The effectiveness of thermal mass in buildings for thermal energy storage is constrained by the timeframe in which the thermal mass can collect and purge thermal energy. Given that the thermal mass must absorb/emit significant energy in the defined timeframe, the rate of heat transfer to/from the thermal mass must be quite large. Given that heat flux is proportional to the heat transfer coefficient and the negative temperature gradient, the temperature difference or the heat transfer coefficient must be increased in order to increase heat flow. In an existing system exposed to ambient climactic conditions, both the heat transfer coefficient (inherent to material) and change in temperature (inherent to climate/weather) are already defined; however, additional heat transfer can be introduced in the form of convection if a pressure source is available.

In buildings, HVAC and ventilation systems move air throughout the building systems through fan-driven pressure differential. The velocity induced through this fan pressure can be used to increase

heat transfer between the heat transfer fluid (HTF) and the thermal mass (storage media) via convection, and can be further increased if the fluid flow is turbulent. The use of convection, specifically ventilation activated thermal mass, has been explored in a variety of literature and has found positive results in increasing thermal exchange between incoming air flows and thermal storage media. A simulated study conducted by Park & Krarti (2015) found that the heat transfer rate between the hollow core slab and room air is directly proportional to the temperature difference between the ventilation air and the slab. The study also found a linear relationship between inlet air temperature and heat flux, as well as a logarithmic relationship between air inlet velocity and heat flux (i.e. increase in velocity increases heat flux at a decreasing rate) and that mass flow rates greater than 1kg/s don't significantly affect the heat transfer coefficient. Furthermore, it was found that an increase in hollow core depth increases and decreases slab surface temperatures in cooling and heating modes respectively due to the insulative effects of interstitial concrete.

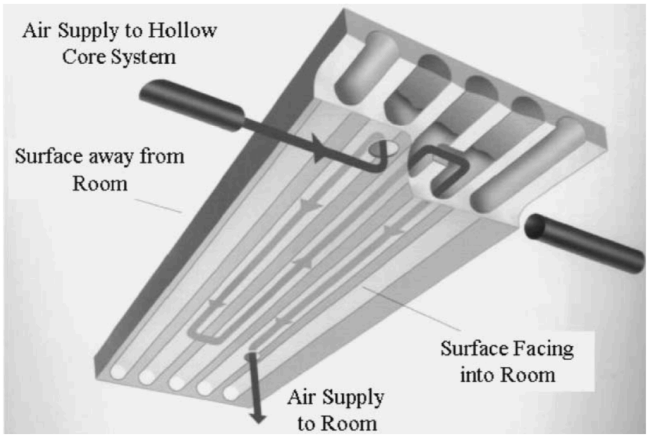

Figure 2.4 – *Termodeck system* (Barton & Beggs, 2002)

A numerical model of a TermoDeck system (Figure 2.5) cooled through night ventilation was analyzed in (Barton & Beggs, 2002) to determine the effects of turbulent flow on heat transfer rate in the bend sections of the hollow cores. The study found that although the heat transfer rate increased significantly in the bend sections, the length of the bend section is small compared to the length of straight sections, resulting in little impact on total heat transfer within the hollow core voids. In addition to the low bend length compared to the straight, heat transfer in the hollow cores is also hindered by the low conductivity of the concrete compared to that of the turbulent heat transfer coefficient. The heat transferred between the airstream and the bend surface is much greater than that of the heat transferred within the concrete, causing the bend surface temperature to approach that of the air stream, reducing the heat transfer rate.

Considering the use of PCM as thermal mass coupled with ventilation, the first study on free cooling was reported in (Raj & Velraj, 2010) and was conducted by Turpenny et al. in (2000), in which cool night air was ventilated through heat pipes embedded in PCM to increase the heat transfer rate. Given a temperature difference of 5°C, the study found a heat transfer rate of 40W over 19 hours. Raj & Velraj (2010) also concluded that the Stefan number (ratio of sensible to latent heat) should be minimized to avoid sub cooling, and that the optimum phase change temperature is equal to that of the desired ambient air temperature plus 2°C to ensure complete solicitation in warm climates.

The effects of PCM placement in temperature amplitude reduction was explored in (Zhuang, 2015) where the authors subjected two blocks, one with PCM on the inner most void (setup A) and one with PCM on the outermost void (setup B), to identical ambient conditions (ventilation velocity and ambient air conditions). The study found that setup A produced significantly better results in terms of thermal attenuation, yielding a maximum interior temperature amplitude of 3.84°C, compared to 6.59°C in setup B. In addition, the study also found that a ventilation velocity of 2 m/s resulted in the greatest benefit, and that ventilation velocity was directly proportional to the heat transfer rate.

Barzin et al. (2015) experimentally evaluated the use of PCM in wallboards with both active cooling and free cooling, analyzing both gross energy and cost savings associated with time of use pricing. The study used direct integration of 22% by weight PCM (phase change temperature = 20°C; heat of fusion = 180 J/g) in gypsum, and compared two test huts – one without PCM (H1) and one with PCM (H2). When exposed to night temperatures, the temperature of H1 dropped below 17°C; while H2 remained above 19°C due to increased thermal inertia, requiring active cooling to effectively precool the structure. With precooling of H2 to 17°C, exposure to solar radiation during the day resulted in the temperature of H1 to increase to 26°C 3 hours earlier than H2, allowing H2 to save 60% of on-peak energy, but consuming 15% more energy than H1. Still, this resulted in a 5% energy cost savings of H2 due to off-peak use of AC energy. Using night ventilation (free cooling) starting at 9pm, H1 increased to 26°C almost 4 hours earlier than H2, allowing for 66% energy savings of H2 associated with the time lag. The study found that the type of assembly and position of PCM significantly affect charging potential, and degree of charging significantly affects energy savings potential.

An experimental investigation of the thermal storage potential of PCM-concrete mixture underneath a fluid loop heat sink embedded in a hollow core slab was conducted in (Pomianowski, Heiselberg, & Lund Jensen, 2012), where theoretical and experimental thermophysical properties (density, specific heat capacity, thermal conductivity) and PCM % content were applied to a model to

determine the effects of various mixture thicknesses on the cooling potential and convective and radiative heat transfer coefficient of the underside of a concrete slab. The study found that theoretical specific heat capacity PCM-integrated concrete was typically overestimated compared to experimental results, likely due to the reduced density of the PCM-concrete mixture; and that the theoretical thermal conductivity was also overestimated compared to experimental results, likely due to increased air content in the PCM-concrete mixture. Furthermore, due to PCM density being lower than that of concrete, density decreases as PCM % content increases. As outlined in Figure 2.6, the study found that the reduced thermal conductivity and density of the mixture counteract the increased heat capacity, resulting in decreasing cooling capacity for a given convective and radiative heat transfer coefficient as PCM-concrete mixture thickness increases. However, the study considered a heat flux boundary condition at the walls of the embedded heat sink, rather than a temperature boundary condition. This results in identical heat transfer in the reference concrete model and the PCM-embedded model, ignoring the temperature stabilizing effects of the PCM concrete and thus likely overestimating heat flow over time of the reference concrete model.

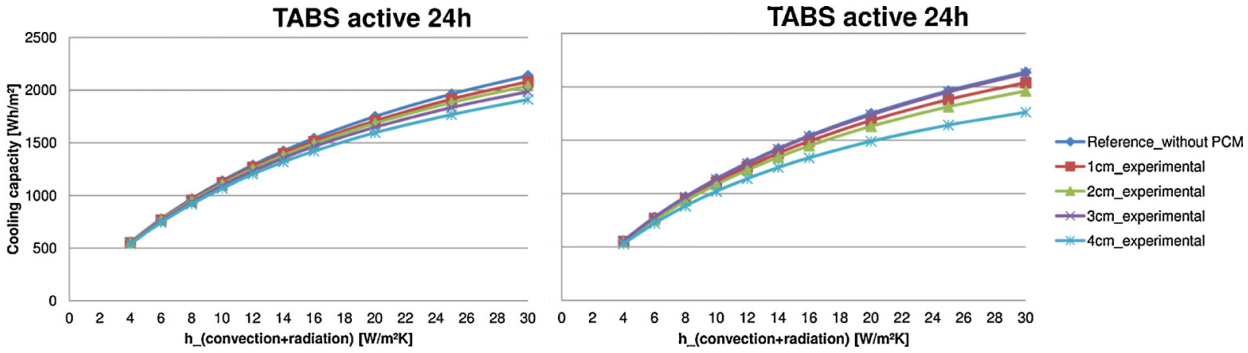

Figure 2.5 *– Experimental Cooling capacity of 4% wt. PCM (Left) and 6% wt. (Right)*

The cooling potential of a microencapsulated PCM enhanced concrete ventilated hollow core slab (VHCS) was numerically evaluated in (Ahmed Faheem, 2016), in which various PCM contents (0% - 20%) and phase change temperatures (18C – 21C) at a heat of fusion of 185 kJ/kg were integrated into a concrete mix to explore the cooling potential of the slab under varying ventilation rates. Two building types were explored, a high thermal mass building experiencing constant indoor air temperatures at night; and a low thermal mass building experiencing dynamic indoor air temperatures at night, associated with the dynamic outdoor night temperature. The high and low thermal mass buildings can be considered synonymous to efficient and inefficient building envelopes respectively. The study measured cooling potential as constant heat flux out of the slab during night cooling, neglecting the transient effects due to dynamic temperature; and omitted internal gains during daytime occupancy of

the buildings. It was found that low thermal mass buildings are much more suited to night cooling of VHCS compared to high thermal mass buildings due to the ability to cool through the hollow cores as well as the underside of the slab exposed to dynamic night temperatures that are cooler than the slab itself. The cooling effect of night ventilation through the hollow cores in high thermal mass buildings was countered by the warming effect of the underside of the slab exposed to constant night temperature that is greater than the slab temperature. Furthermore, the ideal PCM type in high thermal mass buildings was independent of ventilation rate and % content, while the ideal PCM type in low thermal mass buildings is dependent on both % content and ventilation rate. Results of the study are summarized in Figure 2.6.

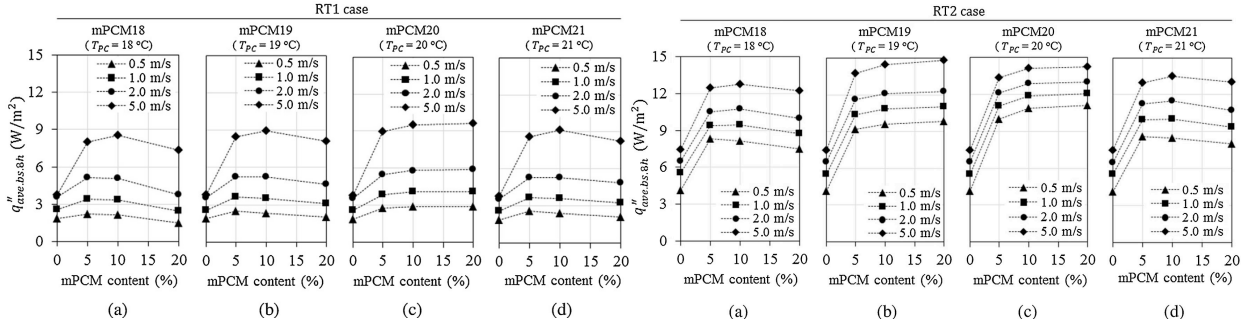

***Figure 2.6**– Cooling potential by PCM type, content, and ventilation rate in high (left) and low (right) thermal mass buildings*

From the literature, it can be seen that there is significant potential in using thermal mass to absorb excess heat introduced at both interior and exterior boundaries, reducing conditioning loads in the cooling season. Interior and exterior applications of thermal mass include PCM integration in gypsum wallboard for internal gains absorption and brick cladding for solar gains absorption respectively. In addition, material heat capacity can be augmented through the addition of PCM with various thermophysical properties to optimize the performance of the mass; and ventilation can be introduced to increase the heat transfer coefficient between the thermal mass and heat transfer fluid. Although active (HVAC induced) and passive (open fenestration) night ventilation techniques increase heat flux from the mass to the ventilated air, the effectiveness of both these techniques are difficult to predict due to the high variability of interior geometry and its effect on air stream turbulence and thus heat flux. Furthermore, past research focuses primarily on the heat transfer from cooled surfaces to the interior air and occupant via convection and radiation respectively, and neglects the radiative heat transfer occurring amongst interior surfaces and their collective effect on radiant heat transfer to the occupant.

3.0: Scope

This research aims to address the shortcomings of current research on activated building thermal mass by determining the radiant field of an interior space in order to solve for both the radiative heat transfer rate amongst building surfaces dictating surface temperature, as well as the mean radiant temperature experienced by an occupant in order to dictate the required air temperature for a given operative temperature. The operative temperature was then assigned to the same zone undergoing night ventilation through the hollow core slab (reduced mean radiant temperature) in order to solve for the air temperature yielding the same operative temperature. This allowed for the determination of cooling load savings associated with hollow core slab night ventilation based on heat transfer from the interior air to the cooled interior surfaces, as well as the increased allowable interior air temperature dictated by the desired operative temperature.

The research was executed through the following steps:

- Heat transfer rate to zone
- Heat transfer rate to occupant
- Operative temperature and required ambient air temperature analysis
- Cooling load determination

This research is a proof of concept for a ventilated hollow core slab system with the ultimate goal of quantifying the energy savings potential as well as the change in occupant comfort associated with radiative cooling to the occupant from surrounding surfaces as opposed to strictly conditioning the ambient interior air. The cooling energy savings was determined based on the change in the cooling load of the space. Cooling load was evaluated rather than cooling energy to allow for generalization of the results, independent of the type of conditioning system employed. Furthermore, the fan power consumption of the active hollow core ventilation system was neglected due to the high variability in the installed condition (single fan per core vs single fan serving multiple cores).

4.0: Simulated System

In order to evaluate the energy savings potential of night ventilation through hollow core slabs, a sample office building was simulated. The goal of the simulation was to determine the conditioning system energy consumption for the cooling season design week in two scenarios – (1) Smart Ventilation (SV) in which the slab hollow cores undergo ventilation via the use of fans when the exterior temperature is less than that of the hollow core surface temperature; and (2) No Ventilation (NV), which is a conventional scenario in which no night ventilation/free cooling is employed.

As a commonly used open-source software, EnergyPlus is a robust energy modelling software capable of evaluating the energy use of buildings of various construction, geometry, use, size, etc. However, the software lacks the ability to simulate non-isothermal flow induced by forced convection in the slab hollow core. The engine uses an adaptive convective heat transfer algorithm to define the heat transfer coefficient formula based on the attributes of the surface (i.e. type, orientation, location, etc.). The input of the IDF (input data file) is evaluated by the engine and defines the heat transfer formula to use. The formula is then executed to define the heat transfer rate based on the attributes and boundaries of the system. Given that the heat transfer rate in the hollow core is transient due to the temperature decay of the air stream, a new convective heat transfer function must be defined to reflect the transient behaviour of the system. Augmenting the EnergyPlus engine back end code introduces uncertainty in the effects of changing the adaptive convective algorithm on other parameters. For example, if the criteria for the slab forced convection algorithm is met by another component, the algorithm would be applied to the component, resulting in misrepresentation of the heat transfer imposed on said component. Furthermore, if this misrepresented component interacts with the slab, the temperature evolution of the slab would also be misrepresented. From this, it can be concluded that misrepresentation of heat transfer on a single component can result in significant error introduced to the simulation. For this reason, it was imperative to isolate the system of interest in order to maximize confidence in the simulated system.

A custom simulation engine was created in MATLAB to effectively model the ventilated slab thermodynamics and to evaluate the interaction between the ventilated hollow core slab and the surrounding environment. As in the EnergyPlus engine, the custom engine treated the simulated model as an array of thermal networks and evaluated the temperature evaluation of the network at each time step based on the respective boundary conditions and power sources. Given that the SV and NV scenarios are exposed to the same exterior environment and internal loads, the exterior boundary and

internal gains (internal-borne and solar) are the same, independent of the engine used. Therefore, the EnergyPlus engine was used to produce a baseline model of the building in DesignBuilder to determine the internal gain inputs for the custom-made engine created in MATLAB. The EnergyPlus model used a CN2014 design week weather data file for Pearson International Airport in Toronto, Canada. The file was created by Whitebox Technologies to reflect the most recent 2000-2014 climate data. The design week weather file was selected to consider the greatest cooling load, allowing for a conservative predication of cooling energy savings (associated with the greatest outdoor air temperature and therefore lowest free cooling potential) as well as the possibility of cooling system size reduction. The outputs of the EnergyPlus model that were used in the custom engine are the following:

- Exterior Temperature – Output of climate file
- Internal Gains – Equipment; lighting; and occupant borne gains based on schedule, distributed equally to all interior surfaces in numerical model
- Solar Gains – Incident solar radiation transmitted through transparent fenestration, dependent on building geometry, orientation, window size/placement, etc., distributed to floor in numerical model
- Incident Solar – the amount of solar radiation striking the exterior surface of the building

These values were then imported into the MATLAB engine in order to simulate the interior building thermodynamics in a completely controlled simulation environment, considering the interaction between the slab with the exterior environment during ventilation, as well as the interaction between the slab and the interior air and among all interior surfaces. This ultimately led to the cooling load reduction associated with night ventilation through concrete slab hollow cores. The process followed for building the numerical model is outlined herein.

4.1: Building Characteristics

The evaluated building is comprised of 5 stories, each 3m in height, with a footprint of 10m x 20m. The window to wall ratio is 40% with a continuous window strip around the perimeter of the building on each story placed at the top of the wall (1.2m in height placed from 1.8m to 3m.). The construction is typical of modern era commercial office buildings in North America. The building is oriented such that the main axis is in the north-south direction with no shading provisions. This orientation was chosen in order to consider the most extreme cooling condition associated with maximum solar gains. An axonometric view of the building can be seen in Figure 4.1.

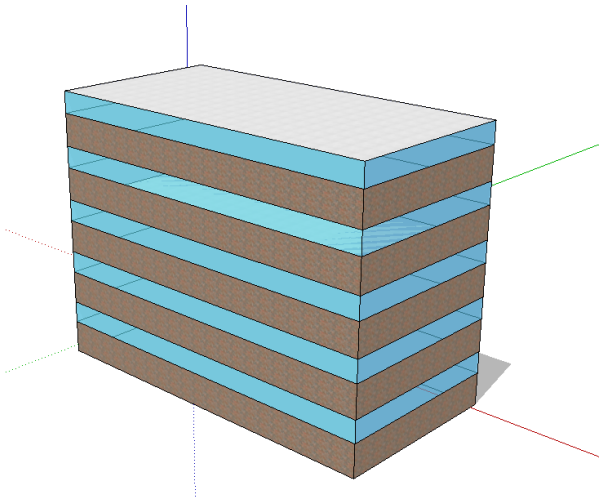

***Figure 4.1**: Axonometric view of modelled office*

The wall assembly is comprised of 10cm brick, 8cm XPS, 10cm concrete block, and 1.3cm gypsum board; typical of the post-war construction common in Toronto. The glazing units are dual pane low-e coated 6mm plate glass with an argon filled air void achieving an effective U-value of 1.978 W/m^2K. The floor finish is 2cm hardwood. The ceiling has no finish and is therefore represented by the hollow core slab. The slab is 0.27m in height with 0.135m radius hollow cores spaced at 0.23m on center, offset from the base and top of the slab by 0.045m as shown in Figure 4.2. It is assumed that there is sufficient insulation between the floor finish and slab to allow for an adiabatic boundary at the top of the slab in order to facilitate maximum heat transfer from the bottom of the slab to the room. Thermophysical properties of material employed can be found in Table 4.1 and were obtained from the DesignBuilder material database.

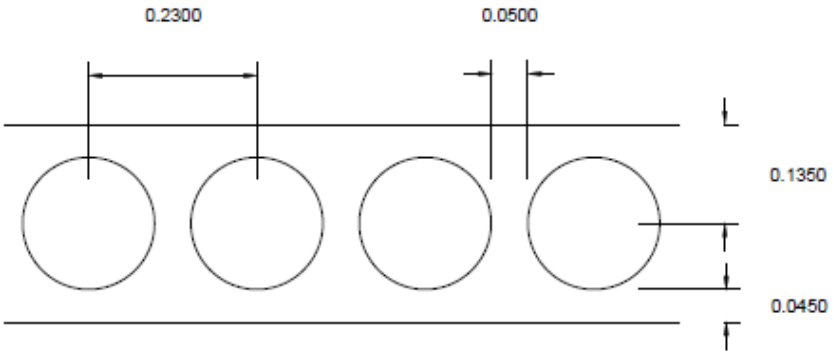

***Figure 4.2**: Termodeck Hollow Core Slab Geometry*

Table 4.1: Thermophysical properties of employed materials

Component	*Conductivity (k)* $\frac{\mathrm{W}}{m\,K}$	*Density (ρ)* $\frac{kg}{m^3}$	*Specific Heat Capacity (c_p)* $\frac{J}{kg\,K}$
Brick	0.84	1700	800
XPS	0.034	35	1400
Concrete Block	0.51	1400	1000
Gypsum Board	0.40	1000	1000
Concrete	1.8	2400	880
Hardwood	0.16	750	1750
Glass	0.80	2500	670
Air (window)	-	0	0

An interstitial floor was evaluated in order to neglect heat transfer from the floor and ceiling to the earth and sky respectively. The interior of the space is completely open with no interior partitions or furniture. Although this simplification isn't representative of typical office interiors, it is assumed that interior surfaces will have temperatures extremely close to the ambient air temperature, resulting in minimal impact on interior convective and radiative heat exchange. North-South and East-West section views of the analyzed room can be viewed in Figure 4.3. The dashed blue line denotes the adiabatic boundary between interior zones, achieved through insulation installed below the floor finish. Although a true adiabat does not exist, the heat transfer from the slab to the exterior air stream is primarily in the upward direction (from underside of slab upward to comparatively cooler air stream) due to the substantial thermal resistance of the floor finish/insulation combination compared to the exposed ceiling. Furthermore, the exposed ceiling required in this system to maximize heat transfer between the slab and interior space necessitates a raised floor for HVAC distribution, supporting the installation of below-floor insulation.

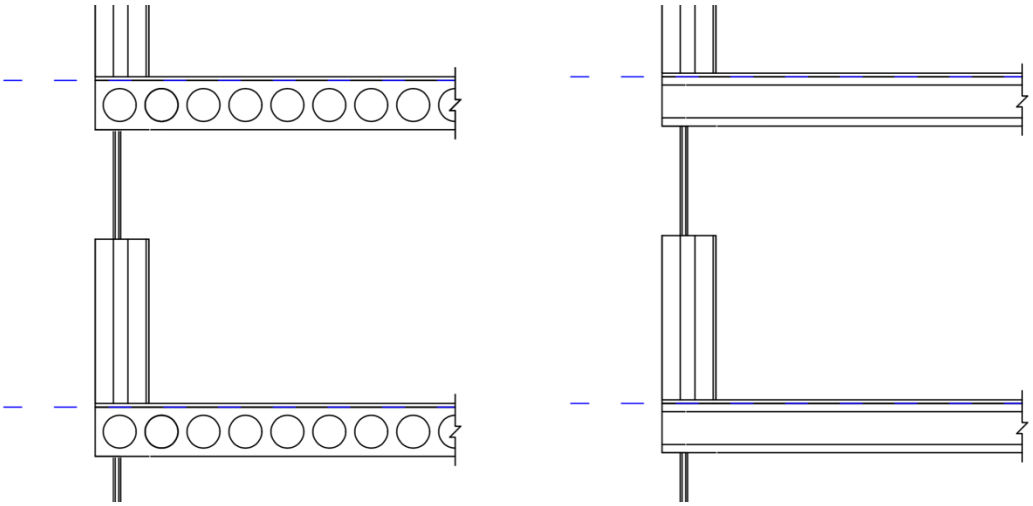

Figure 4.3 – *North-South (left) and East-West (right) Building Sections*

4.2: Boundary Conditions and Power Sources

The system being analyzed is exposed to two real temperature boundaries – the interior (T_a) and exterior (T_e) temperatures; as well as a fictitious sky temperature (T_{sky}) used to evaluate the amount of radiant exchange between the building and the surrounding environment.

The operative temperature was the metric for occupant comfort as shown in eq(1). The operative temperature of the non-ventilated scenario produced in the baseline EnergyPlus model was assigned to the ventilated scenario in order to consider the same level of occupant comfort amongst scenarios; the interior ambient air temperature of the ventilated scenario was then solved for. The interior ambient air temperature of the non-ventilated scenario was solved for base on an operative temperature of 24.8°C.

$$T_{op} = \frac{T_a h_c + T_{mr} h_r}{h_c + h_r} \qquad (1)$$

The equivalent sky temperature describes the temperature of an imaginary blackbody enclosure that would achieve the same heat exchange with the building as the actual (semi-transparent) atmosphere. The sky temperature was found based on the dry bulb and dew point temperatures (Straube & Burnett, 2005).

$$T_{sky} = T_{DB}\left(0.8 + \frac{T_{DP} - 273}{250}\right)^{\frac{1}{4}} \qquad (2)$$

The power sources considered in the simulation included internal gains from occupants, equipment, lighting; solar transmission through windows; and solar incident radiation at the exterior. Gains from occupants were distributed solely to the interior air, while gains from equipment and lighting were distributed to both the air and surrounding surfaces. This distribution was made assuming occupant surface temperatures similar to interior surface temperatures, and equipment and light fixture surface temperatures comparatively higher than interior surface temperatures. Equipment and lighting considered radiant fractions of 0.2 and 0.42 respectively, obtained from the DesignBuilder library database. The radiant fraction of equipment and lighting was distributed uniformly to all interior surfaces and the remaining power was distributed to the interior air. Solar transmission through windows was distributed solely to the floor node as the shortwave radiation would primarily strike the floor and be remitted to the surrounding surfaces as longwave radiation. The solar incident radiation was distributed to the exterior surfaces as dictated by the baseline EnergyPlus model.

4.3: Geometry Discretization

Walls, Windows and Floor

The geometry of the model was broken down into isothermal volumes in order to evaluate the system through the lumped element model in which the system is broken down into nodes separated by resistor. Apart from the slab, all materials within an assembly were treated as isothermal with a single node located in the center of the volume. This was done based on the linear temperature distribution observed in steady-state heat transfer across a material as shown in Figure 4.4.

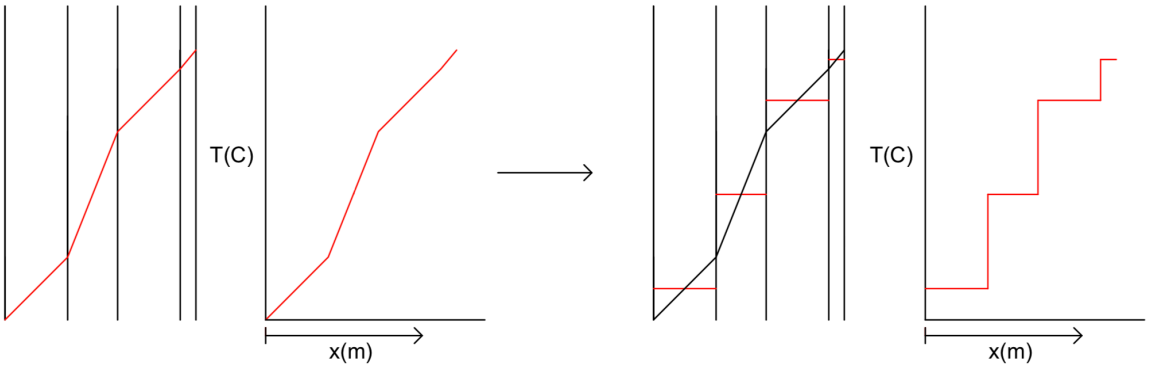

Figure 4.4 *– Linear Temperature (left) vs Constant Temperature (right) Distribution in Node*

It should be noted that the exterior surface experiences high solar heat gain during the day that would result in a non-linear temperature profile within the exterior cladding material (greater heat transfer rate at the boundary than within the volume). However, the XPS located inboard of the brick has substantially higher thermal resistance than the brick, resulting in large temperature change across the thickness of the XPS compared to across the thickness of the brick. Therefore, it is assumed that the error introduced by the overestimation of the brick temperature at the brick-XPS interface is low due to the temperature attenuating effects of the high thermal resistance XPS.

Slab

Due to the high heat transfer rate in the hollow core (forced convection) compared to at the ceiling (free convection), the slab was broken down into lumped elements under the Biot number criterion of Bi ≤ 0.1 (Cengel & Ghajar, 2015). The Biot number is a measure of the ratio of the convective heat flow resistance into a body to the conductive heat flow resistance through the body, and is thus the convective heat transfer coefficient (h) divided by the conductive heat transfer coefficient. As will be discussed in section 5.1, the conductive heat transfer coefficient is equal to the thermal conductivity (k) divided by the conduction path length (l). Therefore, the Biot number simplifies to the following:

$$Bi = \frac{h\, l_c}{k} \qquad (3)$$

The slab is exposed to two regions of convection – a free convection boundary at the underside of the slab exposed to the interior air; and a forced convective boundary at the upper side of the slab exposed to outdoor air when ventilated. The free and forced convective heat transfer coefficients were found to be 2 W/m^{2}K and 13 W/m^{2}K respectively, outlined in section 5.1. To evaluate the linear conductive heat flux across the height of the slab, the 2-dimensional circular hollow core geometry was simplified to a system of two parallel rectangular plates of uniform thickness separated by an air space (representing the hollow core) with the thermal resistance between the air space and bottom boundary equal to that of the hollow core slab; allowing for the heat transfer to be treated as 1-dimensional.

A 2D single core segment with a width of 0.23m was evaluated in COMSOL Multiphysics (Figure 4.5) and yielded a net heat flux of 68.354 W/m. The 2D model consisted of a concrete cross section with a thermal conductivity of 1.8 W/m^{2}K and considered a hollow a 10°C temperature differential between the hollow core and the bottom boundary (underside of the slab). The left, right, and top sizes of the geometry were set to adiabatic. Given the global net heat flux and concrete thermal conductivity, the hollow core section resulted in a parallel-plate system consisting of plates each 0.06m in thickness.

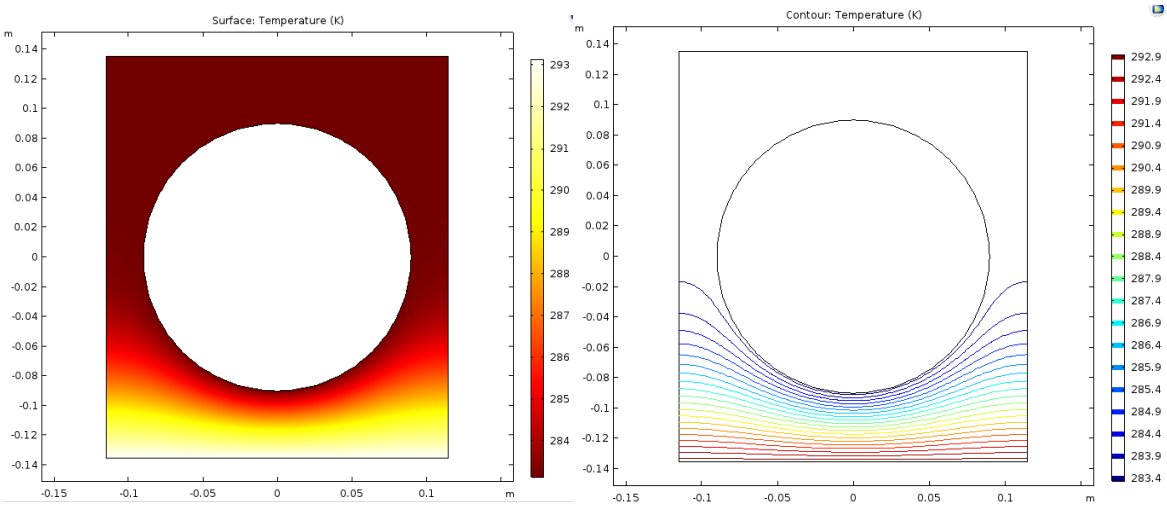

***Figure 4.5**: Slab Temperature Scheme (Left) and Isothermal Contours (Right)*

Based on the above-mentioned convection coefficients and maximum Biot number of 0.10, the maximum plate thickness exposed to the convective boundaries were found using eq(4). The maximum thicknesses for the free and forced convective boundaries were found to be 0.09 and 0.014m respectively, therefore the 0.06m equivalent height rectangle was subdivided to heights of 0.05m and 0.01m exposed to free and forced convection respectively.

$$l_C = \frac{Bi\ k}{h} \qquad (4)$$

4.4: Thermal Networks

The naming convention of the building material volume follows the form *i,j* where *i* represents the assembly in question (i.e. south window, east wall) and *j* represents the layer in the wall, with 1 denoting the material layer closest to the interior and material tags increasing outward. The *i* value tags for walls and windows can be found in Figure 4.6.

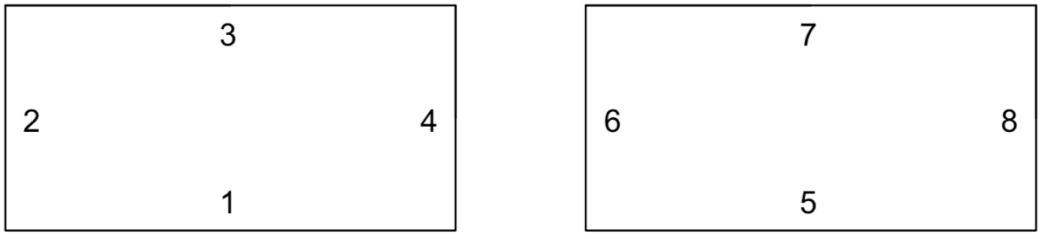

***Figure 4.6 –** Plan View; i Assembly Tags of Walls (left) and Windows (right)*

The geometry was broken down into 10 assemblies based on the above boundary conditions and discretization method – 4 walls (N, E, S, W), 4 windows (N, E, S, W), floor, and ceiling. These surfaces yielded 4 unique thermal networks corresponding to walls, windows, floors and ceilings. There are 4 wall and window networks with common structure but unique solar power at the exterior. As mentioned earlier, solar power was obtained from the baseline EnergyPlus simulation and is based on location, orientation, and building geometry. An east-west section view of the analyzed room with boundaries and nodes can be seen in Figure 4.7.

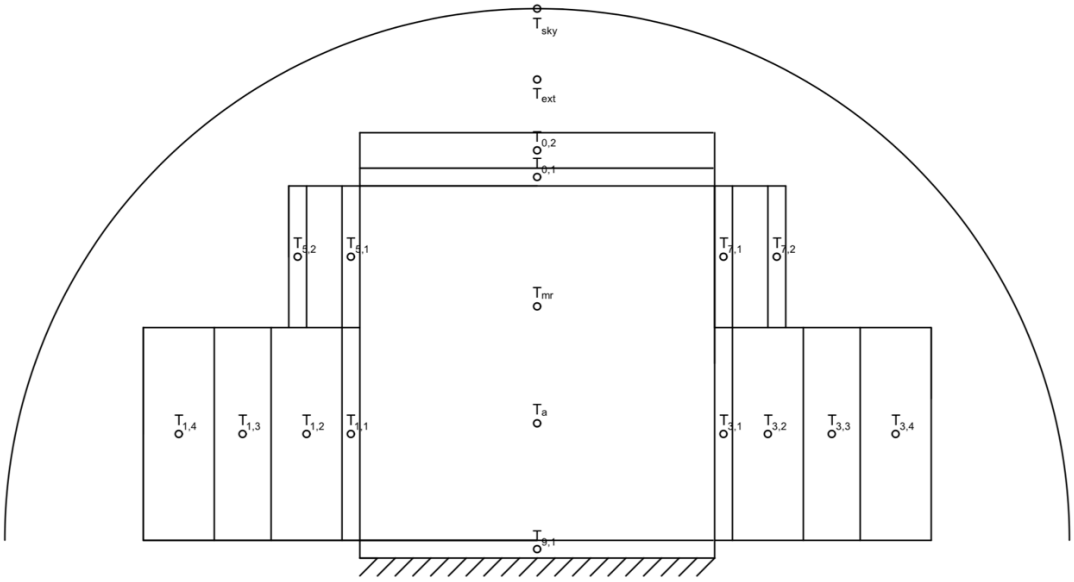

Figure 4.7 – *Section View of Room with Boundaries and Power Sources.*

Based on the isothermal volume assumption of the materials employed in building assemblies, the location of the node within the assembly is located at the midpoint of the materials parallel to the direction of heat flow, resulting in the thermal resistance in and out of the material being equal to half the thermal resistance of the cross section of the material. The general form of the net energy flow to an arbitrary node is outlined in eq(5). The thermal networks of all analyzed assemblies can be found in Figures 4.8 – 4.11.

$$Q_i = \frac{1}{\frac{R_{i-1}}{2} + \frac{R_i}{2}}(T_i - T_{i-1}) - \frac{1}{\frac{R_i}{2} + \frac{R_{i+1}}{2}}(T_{i+1} - T_i) + P_i \qquad (5)$$

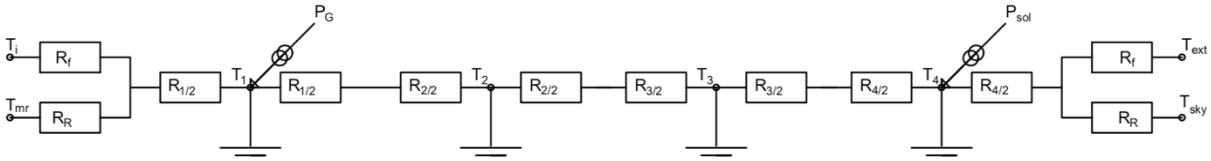

Figure 4.8 – *Wall Thermal Network (4 node)*

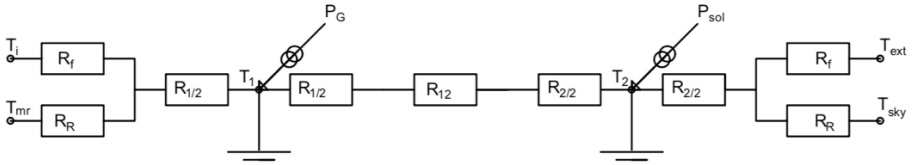

Figure 4.9 – *Window Thermal Network (2 node)*

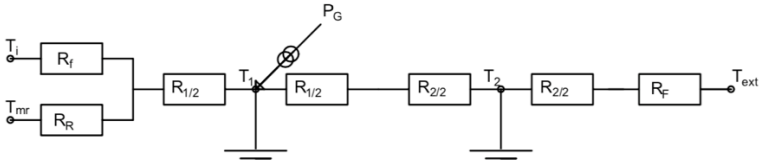

Figure 4.10 – *Slab Thermal Network (2 node)*

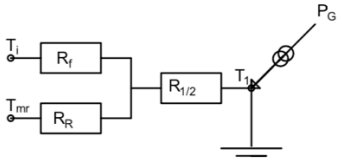

Figure 4.11 – *Floor Thermal Network (1 node)*

The wall thermal network (Figure 4.8) is exposed to the interior in the form of free convective exchange between the wall and the interior air, and radiative exchange between the wall and surrounding interior surfaces. An internal gains power source is present on the interior gypsum board node (T_1), and the node is separated from the interior by the convective and radiative resistors in parallel and a resistor equal to half the interior gypsum board node resistance in series, reflective of the single node per material volume discretization method discussed earlier. In the same fashion, the concrete block node (T_2) is separated from the adjacent interior gypsum board node by half the resistance of the adjacent node (R_1) and half the resistance of the node being evaluated (R_2), as are the XPS (T_3) and exterior brick (T_4) nodes. Similar to the interior, the exterior brick node is coupled to the

outdoor air through free convective exchange between the wall and the interior air, and through radiation between the wall and surrounding interior surfaces.

The window network (Figure 4.9) is similar to the wall network in that it is exposed to convective and radiative resistors in parallel at the interior and exterior with an internal gains and solar power sources at the interior and exterior nodes respectively. However, although the convective heat transfer boundary (interior and exterior air) is the same, the convective heat transfer coefficient is different for each assembly based on the average surface temperature. Similarly, the radiative heat transfer boundary at the exterior is the same for both networks (exterior sky temperature), but the radiative heat transfer coefficient will differ based on the assembly exterior surface temperature. Furthermore, due to the transparent nature of the glass to shortwave radiation, the absorption index of the exterior solar gains is substantially lower than the wall assembly. Unlike the walls, the window glass panes are coupled by a resistor (R_{12}) rather than a node. This resistor represents the air void separating the two panes of negligible heat capacity, hence the lack of capacitor associated with the node.

The hollow core slab (Figure 4.10) is exposed to the same interior boundary and power sources as the walls and windows, and nodes are coupled in the same fashion. Unlike the other networks, the concrete slab volume was subdivided into two nodes as discussed earlier. Furthermore, the exterior node of the slab is not exposed to radiative exchange with the exterior sky temperature as the node is located in the hollow core and therefore does not view the exterior. In reality a low amount of radiant exchange occurs due to the temperature difference between the top and bottom of the slab realized through the adiabatic boundary between the top of the slab and underside of the floor, however, the impact is suspected to be minimal and was therefore ignored.

The floor node (Figure 4.11) is exposed to the interior in the same method as all other networks, but is unique in that it is only exposed to an interior boundary without coupling to the exterior. This is due to the adiabatic boundary beneath the floor preventing any heat flow to/from the floor finish from the underside (top of slab on floor below).

All thermal networks share the same composition inboard of the interior node (convection and radiation in parallel), however, the convective heat transfer coefficient will vary by assembly based on average surface temperature and orientation. Similarly, the radiative heat transfer to the interior is dependant on the mean radiant temperature (MRT) that the surface experiences as well as the temperature of the surface.

5.0: Methodology

5.1: Heat Transfer Coefficients

Conduction

For material of thickness x, the effective conductance of the material is proportional to the conductivity of the material and inversely proportional to the thickness of the material parallel to the direction of heat flow

$$U = \frac{k}{\Delta x} \tag{6}$$

The inverse of thermal conductance yields thermal resistance, useful in determining the effective conductance of an assembly composed of multiple layers of materials

$$R = \frac{\Delta x}{k} \tag{7}$$

The resistance of materials in a wall assembly composed of homogeneous layers perpendicular to the direction of heat flow can be said to have thermal resistors placed in series. This results in the individual resistances of the materials to contribute to the total resistance of the assembly.

$$R_T = \sum R_i \tag{8}$$

Recalling that thermal resistance is the inverse of thermal conductance, the total thermal resistance can be used to determine the effective thermal conductance of the assembly.

$$U_T = \frac{1}{R_T} = \frac{1}{\sum R_i} = \left(\sum \frac{1}{U_i}\right)^{-1} \tag{9}$$

Convection

The general convection heat transfer coefficient formula described in eq(10) calls for the determination of the Nusselt (Nu) number, which describes the ratio of convection to conductive heat transfer within the fluid.

$$h_c = \frac{Nu\ k}{L} \tag{10}$$

Due to free convection's relation to fluid movement and fluid movements relation to buoyancy, the direction of heat transfer, as well as orientation of the surface, significantly impact the Nusselt number. The general form of the free convection Nusselt number for arbitrary geometry is described in eq(11) where the values of A and B are dependent on geometry and orientation. Heat and Mass Transfer (Cengel & Ghajar, 2015) stipulate a and b values for the determination of the Nusselt number for an upward facing heated plate or downward facing cooled plate (synonymous to ventilated slab) when GrPr (Rayleigh (Ra) number) is within the domain $0 < Ra < 2 \times 10^8$, as shown in eq(12).

$$Nu_f = a(GrPr)^b \tag{11}$$

$$Nu_f = 0.15(GrPr)^{\frac{1}{3}} \tag{12}$$

The Grashof (Gr) number describes the ratio of buoyant forces to viscous forces in a fluid, while the Prandtl (Pr) describes the ratio of momentum diffusion to thermal diffusion within a fluid. These dimensionless numbers are strictly related to fluid properties (density, specific heat, viscosity, etc.) and environmental factors (gravity and temperature of surface), and therefore describe fluid movement under no external forces.

$$Gr = g\beta\left(T_{avg} - T_s\right)\frac{\delta^3}{\upsilon^2} \tag{13}$$

$$\beta = \frac{1}{T_{avg}} \tag{14}$$

$$T_{avg} = \frac{T_\infty + T_s}{2} \tag{15}$$

$$Pr = c_p\,\rho\,\frac{\upsilon}{k} \tag{16}$$

In the case of forced convection, fluid velocity is imposed by external factors (i.e. forced air, occupant movement) rather than induced by buoyancy. Therefore, the velocity-dependent Reynolds (Re) number, described in eq(17), is introduced in place of the Grashof number within the Nusselt number. Dynamic viscosity is also introduced to consider the difference in temperature dependant viscosity of the fluid at in the center and at the bounds of the fluid flow. The Nusselt number formula for turbulent pipe fluid flow can be found in eq(18).

$$Re = \frac{\delta V}{\upsilon} \tag{17}$$

$$Nu_F = 0.27\, Re^{0.8}\, Pr^{\frac{1}{3}} \left(\frac{\mu_\infty}{\mu_s}\right)^{0.14} \quad (18)$$

5.1: Heat Transfer in Slab

The energetic flow rate of the ventilated slab air stream is a measure of the amount of energy that can be carried by the heat transfer fluid (HTF), which is defined as the product of the ventilation mass flow rate and heat capacity of the HTF.

$$q = \dot{m}\, c_p \quad (19)$$

The rate of energy flow in transient heat transfer can be related to fluid flow expressing the degree of charging in terms of the energetic flow rate.

$$q = \frac{c_p \rho V}{t} \quad (20)$$

$$\frac{-hAt}{c_p \rho V} = \frac{-hA}{q} \quad (21)$$

This results in a measure of the potential degree of charging of an HTF of known mass flow rate. U is used in place of h to represent the heat transfer coefficient of the HTF to the heat source/receptor system.

$$\eta(q) = exp\frac{-UA}{q} \quad (22)$$

A perfectly insulated fluid loop transferring heat from a source (T^S) to a receptor (T^R) experiences a temperature after passing the source (T_1) and after passing the receptor (T_2), as illustrated in Figure 5.1. q denotes the mass flow rate of the heat transfer fluid, while R^S and R^R represent the thermal resistance between the heat transfer fluid, and the heat source and receptor respectively.

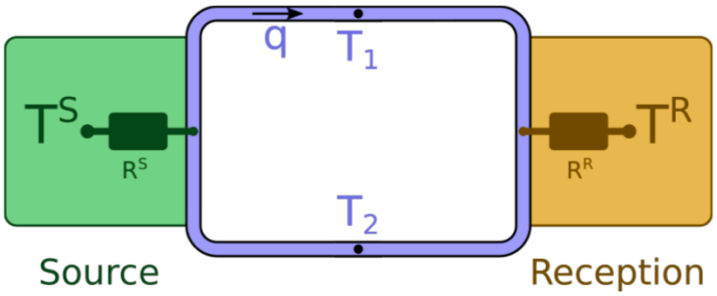

Figure 5.1 – *Scheme of Thermal Network Coupled by Heat Transfer Fluid (David et al., n.d.)*

Applying eq(22) to a fluid loop, the degree of charging of a HTF after heat exchange (i.e. after time t has elapsed) is equal to the ratio of temperature difference between the HTF and source after (temperature after time t has elapsed) and before (initial temperature) charging. Therefore, the degree of charging upon interaction with each the source (η_S) and the receptor (η_R) is as follows:

$$\eta_S = \frac{T_1 - T_S}{T_2 - T_S} \tag{23}$$

$$\eta_R = \frac{T_2 - T_R}{T_1 - T_R} \tag{24}$$

The power delivery from the source to the receptor is proportional to the difference in temperature of the heat transfer fluid before and after transferring heat to the receptor; and the mass flow rate of the fluid.

$$P_{S\to R} = q(T_1 - T_2) \tag{25}$$

Rearranging change in temperature of the heat transfer fluid in terms of temperature difference between the receptor and source yields the following (David et al., n.d.):

$$P_{S\to R} = q\frac{(1-\eta_S)(1-\eta_R)}{1-\eta_S\eta_R}(T_s - T_R) \tag{26}$$

Factoring out the temperature difference between the source and the receptor, the following equivalency is found

$$UA = q\frac{(1-\eta_S)(1-\eta_R)}{1-\eta_S\eta_R} \tag{27}$$

In the case of a night ventilated hollow core slab ($T_{slab} > T_{ext}$), the slab can be considered as the heat source and the exterior air as the receptor. The slab experiences thermal resistance associated with the equivalent heat transfer coefficient of forced convection and interstitial concrete between the node and hollow core boundary. However, heat transfer to the exterior air presents zero resistance as the air is the heat sink, therefore the power equation can be simplified.

$$US_{NW}(q) = q\left(1-\eta_R\right) \tag{28}$$

Ventilation Condition

Turbulent air flow is required in the hollow cores to maximize the heat transfer rate between the exterior air and the hollow core slab. In order to achieve this, the Reynolds number criteria of Re > 4000 was used. Rearranging eq(29) for velocity yields

$$V = \frac{Re\ \upsilon}{\delta} \qquad (29)$$

Considering a characteristic length equal to the radius of the hollow core and an average kinematic viscosity of 1.5 x 10^{-5} m^2/s at the temperature range being explored (EngineeringToolBox, 2003), the minimum velocity to achieve turbulent flow in the hollow core is 0.6635 m/s; resulting in a heat transfer rate of about 4.5 W/m^2*K. Heat transfer rate was found to increase at a decreasing rate with respect to air velocity, therefore, an air velocity of 2 m/s in accordance with (Zhuang, 2015) was selected to allow for a sufficient heat transfer rate while limiting fan power consumption.

5.3: Inter-Zone Heat Transfer

Within the analyzed zone, the primary methods of heat transfer are between the interior air and surrounding surfaces through convection; and between interior surfaces through radiation. Additionally, all surfaces in the room interact with the room air and all surfaces within view of each other interact with one another. For simplicity, heat transfer was only analyzed among interior surfaces and the interior air. To compare the ventilated and non-ventilated scenarios, the thermal interaction between an occupant and the surrounding environment (surfaces and ambient air) was analyzed. However, occupant-environment thermal interaction was analyzed independent of inter-environment thermal interaction, and therefore did not consider the shading caused by an occupant in the radiant field.

Radiant Field

Within the interior space of a room, the surfaces (including exterior walls, partition, furniture, equipment, etc.) have a heat capacity and therefore both absorb and emit heat through convection with the air and radiation to/from other opaque surfaces. The interior air is assumed to be well mixed and is therefore considered isothermal. It is also assumed that the building conditioning system meets the demand on the space instantaneously, resulting in no change in interior air temperature during thermal interaction. For these reasons, the convective heat transfer rates from building surfaces are rather simple to determine. In contrast, the radiative heat transfer amongst interior surfaces becomes complex

due to the quantity of unique surfaces and the view factors between them. The radiosity method was used to determine radiative hear transfer in the interior space as discussed herein.

All bodies at a temperature greater than 0K emits longwave thermal radiation. The magnitude of radiation emitted from a body is proportional to the temperature of the body raised to the fourth power, as well as the emissivity of the surface.

$$M_i = \varepsilon\sigma T^4 \tag{30}$$

In addition to the radiation produced by virtue of the temperature of the surface, the surface also reflects a portion of radiation that it receives from other surfaces emitting radiation (irradiance). For an opaque body (no transmitted radiation), the proportion of irradiance reflected is equal to one minus the emissivity of the surface

$$J_{i,r} = (1 - \varepsilon)E_i \tag{31}$$

The total radiation leaving a surface per unit area of the surface, herein referred to as radiosity, is the sum of the radiation produced by the temperature of the body and the reflected irradiance of the body.

$$J_i = M_i + J_{i,r} \tag{32}$$

Produced radiation (M) can be determined with ease if the temperature of the material is known. However, the irradiance of the surface requires the knowledge of the temperatures of all surrounding surfaces as well as the view factors of the surrounding surfaces to the surface in question. The irradiance is equal to the n^{th} sum of the products of the view factor multiplied by the radiosity of the surface with n representing the number of surfaces.

$$E_i = \sum_{j=1}^{n} F_{i\to j}\, J_{e,j} \tag{33}$$

The radiant heat flux experienced by a surface can then be defined as the difference in irradiance and radiosity of the surface multiplied by the area of the surface

$$Q_R = A_e(E_e - J_e) \tag{34}$$

$$Q_R = A_e[\,(\sum_{j=1}^{n} F_{i\to j}\, J_{e,j}) - J_e] \tag{35}$$

Inter-Zone Surface View Factors

The view factors amongst interior surfaces (F_v) took on the form F_{ij} where i denotes the surface in question and surface j denotes the surface being evaluated. That is to say, F_{ij} represents the view factor of surface i to surface j.

$$F_{i\to j} = \begin{bmatrix} F_{11} & F_{12} & \cdots & F_{1j} \\ F_{21} & F_{22} & \cdots & F_{2j} \\ \vdots & \vdots & \ddots & \vdots \\ F_{i1} & F_{i2} & \cdots & F_{ij} \end{bmatrix}$$

Given that the zone being analyzed is completely closed, the radiosity emitted from any given surface is received by all the surrounding surfaces with zero radiosity lost to the system. For this reason, the sum of the radiosity received by the j surrounding surfaces is equal to the radiosity emitted by surface i. Therefore, the sum of the view factors from surface i to the j^{th}surface is equal to 1.

$$\sum_{N=1}^{j} F_{i\to j} = 1 \qquad (36)$$

Additionally, recalling that the view factor is a measure of how much a given surface i "sees" another surface j, the view factor is applicable only to surfaces acting on a single plane. Complex geometries must be broken down into planar surfaces, and curved surfaces must be either simplified to planar geometry or the differential view factor between two differential areas (described in section 5.1) can be used. Given that radiation is emitted from a planar source, the source is unable to see itself, and therefore the view factor from any planar surface to itself is equal to 0.

$$F_{i\to i} = 0 \qquad (37)$$

An array of view factor charts and calculators are available online and in literature for the determination of the view factors among surfaces with defined relationships, namely parallel rectangles (rectangles of equal size separated by a length perpendicular to the plane of both rectangles), coaxial disks (circles of varying radii separated by a length perpendicular to the plane of both circles), and perpendicular rectangles (rectangles of equal width with a common edge at a right angle), illustrated in Figure 5.2.

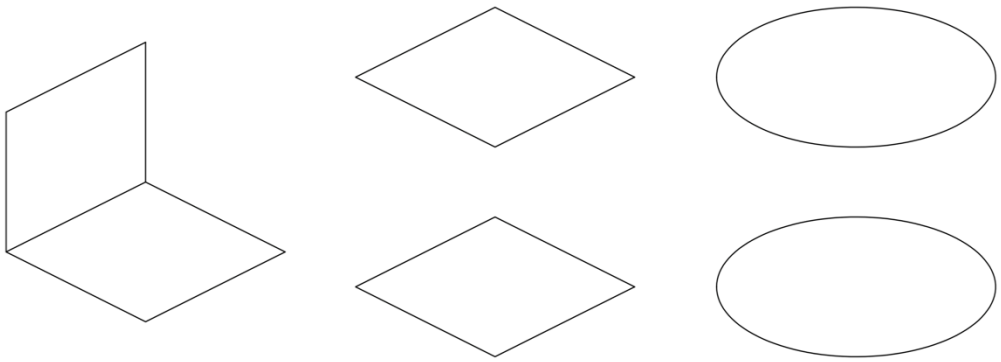

Figure 5.2 – *Standard View Factor Orientations – Perpendicular Rectangles (left); Parallel Rectangles (center); Coaxial Discs (Right)*

These resources provide view factors for simple shapes and arrangements, and therefore must be adapted to the system being analyzed. Since the analyzed zone consists of four walls, four windows, one ceiling and one floor oriented orthogonally, these arrangements were adapted to the simulated zone using view factor algebra, as outlined below in Figure 5.3 and eq(38).

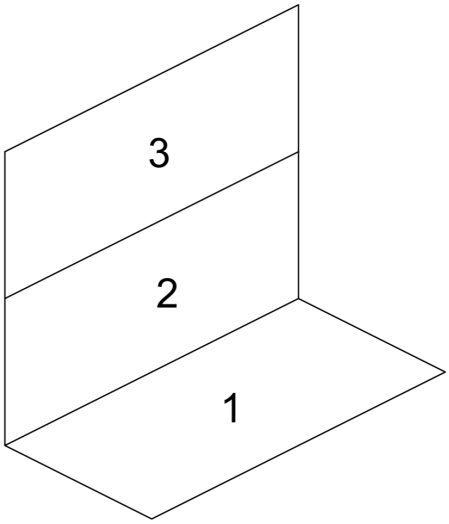

Figure 5.3 – *Surface tags for $F_{1\to3}$ algebraic determination*

$$F_{1\to3} = F_{1\to2+3} - F_{1\to2} \qquad (38)$$

Using a view factor calculator developed at the University of Laval (Lauzier, 2005) as well as eq(38), the view factors amongst all interior surfaces were determined, summarized in the matrix below. Rows denote the emitting surface while columns denote the receiving surface (i.e. Row 6 column 2 denotes the view factor from surface 6 to surface 2). Note that orthogonal orientation of the surfaces

is reflected in the zero value along the diagonal (surfaces viewing themselves) and between surfaces 1 and 5; 2 and 6; 3 and 7; and 4 and 8 (surface on same plane as other surface).

$$F_{vs} = \begin{bmatrix} 0.0000 & 0.0890 & 0.0132 & 0.0890 & 0.0000 & 0.0366 & 0.0087 & 0.0366 & 0.4044 & 0.3224 \\ 0.0445 & 0.0000 & 0.0445 & 0.0629 & 0.0183 & 0.0000 & 0.0183 & 0.0405 & 0.4241 & 0.3469 \\ 0.0132 & 0.0890 & 0.0000 & 0.0890 & 0.0087 & 0.0366 & 0.0000 & 0.0366 & 0.4044 & 0.3224 \\ 0.0445 & 0.0629 & 0.0445 & 0.0000 & 0.0183 & 0.0405 & 0.0183 & 0.0000 & 0.4241 & 0.3469 \\ 0.0000 & 0.0549 & 0.0131 & 0.0549 & 0.0000 & 0.0670 & 0.0084 & 0.0670 & 0.3056 & 0.4285 \\ 0.0275 & 0.0000 & 0.0275 & 0.0608 & 0.0335 & 0.0000 & 0.0335 & 0.0421 & 0.3297 & 0.4454 \\ 0.0131 & 0.0549 & 0.0000 & 0.0549 & 0.0088 & 0.0670 & 0.0000 & 0.0670 & 0.3056 & 0.4285 \\ 0.0275 & 0.0608 & 0.0275 & 0.0000 & 0.0335 & 0.0421 & 0.0335 & 0.0000 & 0.3297 & 0.4454 \\ 0.0364 & 0.0763 & 0.0364 & 0.0763 & 0.0183 & 0.0396 & 0.0183 & 0.0396 & 0.0000 & 0.6587 \\ 0.0290 & 0.0625 & 0.0290 & 0.0625 & 0.0257 & 0.0535 & 0.0257 & 0.0535 & 0.6587 & 0.0000 \end{bmatrix}$$

In addition to radiative heat transfer between interior surface, heat transfer also occurs via radiation with the occupants. The view factor from the surrounding surfaces to the occupant took on the form F_j which describes the view factor from surface j to the occupant.

$$F_j = \begin{bmatrix} F_1 \\ F_2 \\ \vdots \\ F_j \end{bmatrix}$$

Similar to the surface to surface view factors, the simulated zone is completely closed and therefor the sum of view factors to the occupant is equal to 1.

$$\sum_{N=1}^{j} F_j = 1 \qquad (39)$$

In order to determine the view factor between an occupant and the surrounding surfaces (F_{vo}), an algorithm developed by Cannistraro et al. (1992) based on the initial works of Fanger (1972) was used as outlined below. The values used in the view factor algorithm can be found in Table 5.1

$$F_{P\to i} = F_{max}(1 - exp\frac{-a}{c\,\tau})\,(1 - exp\frac{-b}{c\gamma}) \qquad (40)$$

Table 5.1: Coefficient Formulas and Inputs used in View Factor Calculation Algorithm (Cannistraro, Franzitta, & Giaconia, 1992)

Case	$\tau = A + B\frac{a}{c}$				$\gamma = C + D\frac{b}{c} + E\frac{a}{c}$			
	F_{max}	A	B	R^2	C	D	E	R^2
SEK1	*0.132*	*1.14505*	*0.14524*	*0.983*	*0.74379*	*0.10312*	*0.02967*	*0.837*
SEK2	*0.103*	*1.33522*	*0.14454*	*0.985*	*0.60637*	*0.14678*	*0.04628*	*0.906*
SEK3	*0.131*	*1.41607*	*0.09957*	*0.964*	*0.76196*	*0.07182*	*0.05578*	*0.858*
SEK4	*0.104*	*1.15253*	*0.13945*	*0.988*	*0.73371*	*0.09442*	*0.03688*	*0.856*
SEK5	*0.130*	*1.31858*	*0.12807*	*0.975*	*1.00432*	*0.03802*	*0.06189*	*0.783*
SEK6	*0.101*	*1.51966*	*0.12266*	*0.957*	*0.84923*	*0.10471*	*0.05704*	*0.948*

Table 5.2 – Description of cases used in Table 5.1

Case	Posture	Description
SEK1	Seated	Vertical rectangle on front wall of the person and above their center/back wall of person and below their center
SEK2	Seated	Vertical rectangle on front wall of the person and below their center/back wall of person and above their center
SEK3	Seated	Vertical rectangle on side wall of the person above and forward of their center/below and behind their center
SEK4	Seated	Vertical rectangle on side wall of the person below and forward of their center/above and behind their center
SEK5	Seated	Horizontal rectangle on ceiling and forward their center/on floor and behind their center
SEK6	Seated	Horizontal rectangle on ceiling and behind their center/on floor and forward their center

The occupant's position and orientation within the simulated zone has a substantial impact on the radiant heat transfer to the occupant due to the asymmetry of the human body (greater surface area facing front/back vs side) as well as the physical attributes of the room (distance to surface, emissivity, etc.). For the sake of comparison, the occupant was simulated as sitting at a height of 0.6 m in the centre of the room facing south. The works of Fanger (1972) simplify the cumulative view factor of the body's infinite differential planar area composition to the view factor of a single node located at the center of the body – 0.6m for a seated person and 1.0m for a standing person. This method considers the projected area from surfaces surrounding the node about the node, such that a surface around the node is broken down into four surfaces: bottom left (i), bottom right (ii), top left (iii), and top right (iv), as shown in Figure 5.4.

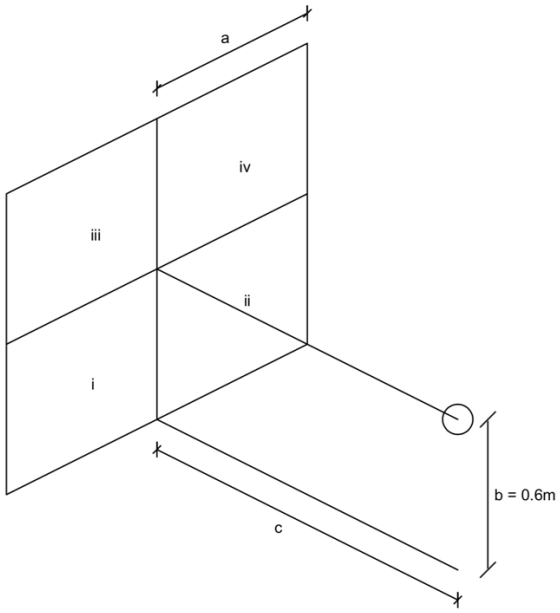

Figure 5.4 – *Surface breakdown to occupant node*

The surface breakdown applies to all surfaces including horizontal ceiling and floor producing front left, front right, back left, and back right surfaces. In evaluating a node(person), the surrounding geometry must be broken down in terms of both node position as well as surface materiality, such that each unique surface (material, orientation, emissivity, etc.) receives a unique view factor. Given the 0.6m height of a seated person, the surrounding surface breakdown method shown in Figure 5.4 yields two rectangles below the node 0.6m in height representative of the wall, and two rectangles above the node 2.4m in height, representative of 1.2m of wall and 1.2m of window, as shown in Figure 5.5. The width of the surrounding surface is equal to the width of the room (i.e. entire planar area evaluated at

once). Due to the difference in materiality of the surfaces above the node (wall and window), the area above the node was further subdivided into two 1.2m sections to separate the wall and window. The view factor to the occupant was then determined in three steps – view factor to wall below node; view factor to wall above the node; and view factor to the window. The view factor to the windows was determined through deduction equal to the view factor to the 2.4m section above the node minus the view factor to the 1.2m section above the node due to the view factor determination method requiring all distances to be from the node.

Using the view factor algorithm developed by Cannistraro et al. (1992) and the above view factor algebra to break down the wall into opaque and transparent components, the following view factors were obtained:

$$F_{vo} = \begin{bmatrix} 0.0700 \\ 0.0164 \\ 0.0754 \\ 0.0164 \\ 0.0232 \\ 0.0077 \\ 0.0307 \\ 0.0077 \\ 0.4343 \\ 0.3183 \end{bmatrix}$$

The operative temperature metric used to evaluate occupant comfort is highly dependent on radiative heat transfer to the occupant. Additionally, the SV scenario has a localized cooled zone (inside hollow core) during ventilation, resulting in a relatively asymmetric radiant field in the simulated zone compared to the that of the NV scenario. Therefore, the radiant heat transfer within the simulated zone was evaluated using the single-order reflectance radiosity model.

Recalling eq(31), the radiation of any given surface is the sum of the sum of the irradiances reflected by the surrounding surfaces and the radiation produced by the surface; and the radiative heat flux to that surface is equal to the net unit radiosity of the surface multiplied by the area of the surface.

$$J_i = (1 - \varepsilon_i)(\sum_{N=1}^{j} F_{j \to i} J_j) + \sigma \varepsilon_i {T_i}^4 \qquad (41)$$

$$Q_R = A_i[\,(\sum_{N=1}^{j} F_{j \to i} J_{i,j}) - J_i] \qquad (42)$$

The summation operator in the above equations can be eliminated for variables in the following matrix form:

$$\vec{J} = \begin{bmatrix} J_1 \\ J_2 \\ \vdots \\ J_j \end{bmatrix}; \qquad [I] = \begin{bmatrix} 1 & 0 & \cdots & 0 \\ 0 & 1 & \cdots & 0 \\ \vdots & \vdots & \ddots & \vdots \\ 0 & 0 & \cdots & 1 \end{bmatrix}; \qquad [\varepsilon] = \begin{bmatrix} \varepsilon_1 \\ \varepsilon_2 \\ \vdots \\ \varepsilon_j \end{bmatrix}; \qquad [F] = \begin{bmatrix} F_{11} & F_{12} & \cdots & F_{1j} \\ F_{21} & F_{22} & \cdots & F_{2j} \\ \vdots & \vdots & \ddots & \vdots \\ F_{i1} & F_{i2} & \cdots & F_{ij} \end{bmatrix}; \qquad \vec{T} = \begin{bmatrix} T_1 \\ T_2 \\ \vdots \\ T_j \end{bmatrix}$$

The radiosity and radiative heat flux equations are then represented in matrix notation:

$$\vec{J} = \left[[I] - ([I] - [\varepsilon]) [F] \right]^{-1} (\sigma [\varepsilon] \vec{T}^4) \tag{43}$$

$$\vec{Q}_R = [A] \left[([F] - [I]) \vec{J} \right] \tag{44}$$

Power Sources

The power sources considered in the simulation include internal gains from occupants, lighting, and equipment; as well as solar gains on the exterior and through transparent assemblies. As mentioned in section 4.2, radiative internal gains were assumed to be diffuse in nature, and were therefore distributed to all interior surfaces using a weighted area method outlined in eq(45).

$$G_i = G_{total} \frac{A_i}{\sum A_n} \tag{45}$$

Conversely, the solar gains to the interior space were assumed to be direct, and was therefore distributed solely to the floor finish node. These gains were then redistributed to the interior air via convection and the surrounding surfaces via radiation at each subsequent timestep.

Interior Temperature Boundary

Given that a body interacts with nearly transparent air, the heat flow rate to the surroundings is governed by convection to the air and radiation to the surrounding opaque surfaces. The sum of convective and radiative heat transfer must be equal to the net heat produced by the body in order to maintain a stable body temperature and therefore achieve occupant comfort. The heat transfer rate from a body via convection and radiation are dependent on the temperature of the ambient air and surroundings surfaces respectively. To relate these different temperatures, the operative temperature is introduced as a measure of the surface and air temperatures of an imaginary blackbody enclosure that would achieve the same heat transfer rate with a body as the body experiences in an environment.

$$T_o = \frac{h_r T_{mr} + h_c T_a}{h_r + h_c} \quad (46)$$

Given an average interior ambient air temperature of 23°C and an average mean radiant temperature of 25.5°C in the baseline model, the operative temperature was found to be 24.8°C. The operative temperature requires the knowledge of the mean radiant temperature, which is the weighted average of the temperatures of the surrounding surfaces raised to the fourth power.

$$T_{mr,i} = \sqrt[4]{\sum_{j=1}^{n} {T_j}^4 F_{j \to i}} \quad (47)$$

The desired operative temperature was set equal to the operative temperature in the baseline EnergyPlus model in order to compare the thermal comfort of occupants for each scenario. Rearranging eq(46) to solve for air temperature results in the following:

$$T_a = \frac{T_{op}(h_r + h_c) - h_r T_r}{h_c} \quad (48)$$

5.4: Zone Temperature Evolution

Heat transfer through the exterior walls and slab as well as within the simulated zone was analyzed through the Euler forward step method in which the initial conditions of the system are known and the change in the system is evaluated at every time step. The conditions at the subsequent time step are defined as the conditions at the previous time step plus the change in the conditions during the time step. The general form of time and the temperature evolution are as follows:

$$t_{n+1} = t_n + t \quad (49)$$

$$T_{t+1} = T_t + \Delta T_t \quad (50)$$

$$\Delta T_t = \frac{1}{m c_p} \int_{t_n}^{t_{n+1}} Q\, t \quad (51)$$

The time step was defined based on a maximum temperature change criterion of 0.1K for any given node, considering that any energy introduction to the system will induce a temperature change of the body, which will then result in a heat flux out of the body, as demonstrated though eq(52).

$$t = \frac{\Delta T_t\, m\, c_p}{Q} \quad (52)$$

The maximum temperature change will occur due to a large energy introduction or low heat capacity, or a combination thereof. In the simulated system, the greatest power source is solar incident radiation on the east wall in the early morning; and the lowest thermal mass exposed to this source is the glass pane capacitor. However, the maximum solar incidence occurs when the sun is low and therefore assume to be normal to the glass pane, resulting in an absorption index of 0.05 (Hutcheon & Handegord, 1995). Conversely, the brick used on the building exterior (and most typical building materials) has an emissivity of 0.90. In accordance to Kirchoff's law of thermal radiation, emissivity is assumed to be equal to absorptivity in the temperature range being explored, resulting in an absorption index of 0.90 or for the brick. Therefore, the time step was defined as the lower of the time required for the west wall exterior glass pane or brick to achieve a temperature increase of 0.1C during the greatest magnitude of solar incident radiation. It should be noted that the absorption index of the glass increases to around 0.5 when the incident angle to the pane of the glass approaches zero. This could theoretically be the case when the sun is at its highest, but is not likely to be realized due to the shading effects of the window frame and surrounding assemblies.

The maximum solar incidence occurs on the morning of the 3rd day of the simulation on the east wall with a value of 1000 W/m^2 as displayed in Figure 5.6. Using eq(52), the maximum time step value was found to be 20.1s for the glass pane and 30.2s for the brick. Given the uncertainty of the angle of incidence at the time of maximum solar incidence, the 20.1s value was reduced to 15s to compensate for the error associated with the absorptivity estimate.

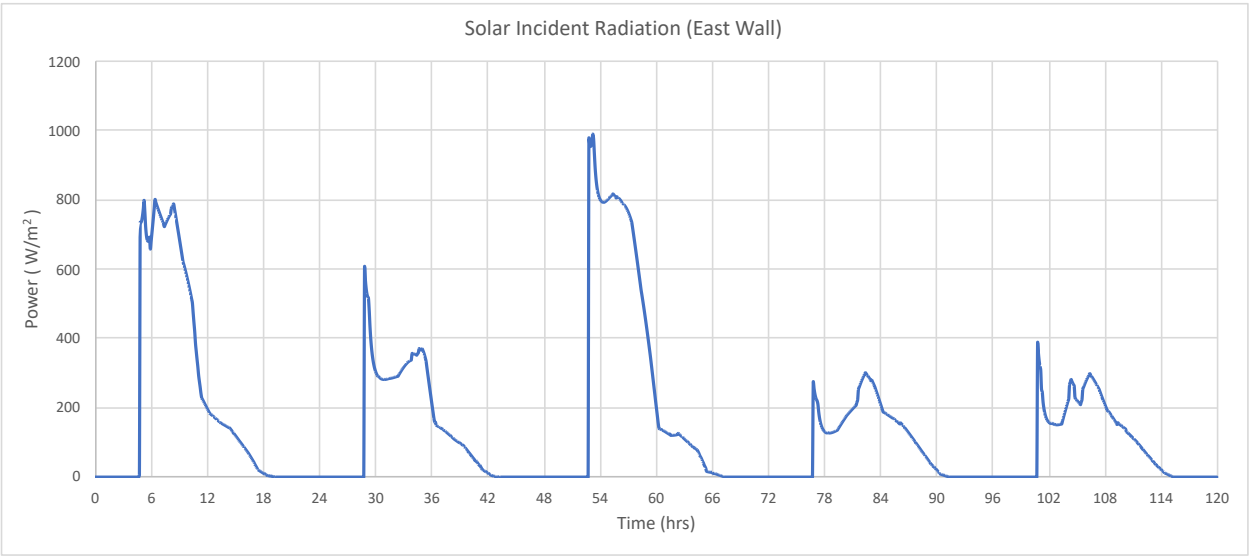

Figure 5.5 – *Magnitude of Solar Incident Radiation on East Wall During Design Week*

The rate of heat net heat flow to a body is directly proportional to the temperature evolution of the body. This necessitates the knowledge of the boundaries of the system as well as the thermal network to determine the net flux to each node, yielding the temperature change of the system. The thermal networks and boundaries of the evaluated system (presented in section 4.4) were used to determine the flux to each node. The geometric and themophysical properties of the materials employed in each assembly are summarized in Table 5.2.

The heat flux to each node is defined as the sum of the heat flux to the node imposed by the boundary and energy introduction to the system during the time step is defined as the net flux multiplied by the time step. Finally, the temperature change of the node during the time step is equal to the energy delivered to the system during the time step divided by the energy capacity. The temperature change of any given node in terms of boundary and node properties is described in eq(53).

$$dT_i = \frac{1}{m_i c_{pi}} t \left[U_{(i-1)\to i}(T_i - T_{i-1}) - U_{i\to(i+1)}(T_{i+1} - T_i) + P_i \right] \qquad (53)$$

Table 5.3 – Assembly Material Thermophysical Properties by Node

Assembly Index	Assembly Type	Node Index	Node	k	l	U_i	R_i	ρ	c_p
			Material	$\frac{W}{m\,K}$	m	$\frac{W}{m^2\,K}$	$\frac{m^2\,K}{W}$	$\frac{kg}{m^3}$	$\frac{J}{kg\,K}$
1-4	*Wall*	1	GWB	0.40	0.013	30.77	0.0325	1000	1000
		2	Conc Blk	0.51	0.10	5.1	0.1961	1400	1000
		3	XPS	0.034	0.0792	0.4293	2.3294	35	1400
		4	Brick	0.84	0.10	8.4	0.119	1700	800
5-8	*Window*	1	Glass	0.8	0.006	133.33	0.0075	2500	670
		2	Glass	0.8	0.006	133.33	0.0075	2500	670
9	*Floor*	1	Wood	0.16	0.019	8.4210	0.11875	750	1750
10	*Slab*	1	Concrete	1.8	0.05	36	0.0278	2400	880
		2	Concrete	1.8	0.01	180	0.0056	2400	880

Table 5.4 – Assembly Convection Coefficients by Surface

Type	Surface	Node	Fluid	cHTC (W/m2K)
Forced Convection	Hollow Core	0_2	Outdoor air	**13.5**
Free Convection	Ceiling	0_1	Indoor Air	**2.9**
Free Convection	Floor	9_1	Indoor Air	**2.9**
Free Convection	Wall (Interior)	(1-4)_1	Indoor Air	**2.5**
Free Convection	Window (Interior)	(5-8)_1	Indoor Air	**1.75**
Forced Convection	Wall (Exterior)	(1-4)_4	Outdoor Air	**15**
Forced Convection	Window (Exterior)	(5-8)_2	Outdoor Air	**15**
Free Convection	At Occupant	n/a	Indoor Air	**2.25**

Cooling Load

The cooling load of the evaluated system neglected ventilation demand as well as the latent load associated with occupants, and was thus set equal to the sum of the total heat flux though the assembly and the total gains imposed on the system air, as well as the cooling powered required to achieve the desired ambient air temperature at the current timestep.

$$Q_{c,i} = \sum Q_{i,j} + \sum F_f G_i + P_{dT_i} \quad (54)$$

Given the nodal separation of the interior air to the interacting surfaces, the convective heat flux was defined based on the potential difference between the inferior air and surface nodes.

$$\sum_{N=1}^{j} Q_{i,j} = h_f * (T_{a,i} - T_{j.i}) \quad (55)$$

The power required to meet the temperature differential of the time step, independent of internal gains and flux, is defined as follows

$$P_{dT_i} = \frac{dT_i \rho_a V_a c_{p,a}}{tA} \quad (56)$$

5.5: Occupant Comfort

Due to the difference in dynamic operative temperature achieved in both the SV and NV scenarios, the level of comfort experienced by occupants is variable, dependent on the interior conditions (temperature, relative humidity, etc) as well as individual attributes (metabolic rate, activity level, clothing, etc). For this reason, the *Predicted Mean Vote (PMV)* comfort metric (Fanger, 1972) was used to evaluate occupant comfort in both simulated scenarios. The PMV is measured on a scale in the domain {-3 < x < 3} with negative values representing cold sensation and positive values representing warm sensation. PMV values in the domain {-1 < x < 1} are considered acceptable for occupant comfort.

The PMV was calculated based on constant interior conditions apart from interior temperatures. That is to say, the ambient air and mean radiant temperatures were updated at every time step, while the air velocity (0.5m/s); relative humidity (50%); and partial pressure of air (1.013mmHg) remained constant. Individual attributes including metabolic rate, clothing level, DuBois area, and mechanical efficiency remained also remained constant due to the assumption of consistent behaviour aligned with office work (sitting position, relaxed, etc.). The power balance of the body is defined as the following:

$$L = q_{met} - q_{SD} - q_{SS} - q_{LR} - q_{SR} - q_{rad} - q_{conv} \quad (57)$$

Based on these power sources and losses, the PMV was calculated using Fanger's comfort equation:

$$PMV = 0.352 \exp\left(-0.042 \frac{M}{A_{Du}} + 0.032\right) L \quad (58)$$

While the PMV metric aim to describe the thermal sensation that the population experiences on average, the Predicted Percent Dissatisfied (PPD) metric (Fanger, 1972) is a metric used to determine the proportion of occupants within a population that will experience thermal discomfort in a given environment.

$$PPD = 100 - 95 * \exp\left(-0.03353\ PMV^4 - 0.2179\ \ PMV^2\right) \quad (59)$$

5.6: Simulation Engine Logic

The custom engine used to evaluate the heat transfer occurring in the simulated system using geometric attributes and initial conditions to determine the temperature evolution of the system. The initialization inputs of the system are as follows:

- Start time (t0); End time (tFinal); Time Step Size (h)
- Building assembly geometric attributes (areas, height/thickness, etc.)
- Material thermophysical properties (thermal conductivity, specific heat capacity, etc.)
- Node initial temperatures
- View factors among surfaces; View factors to occupant

These inputs were then fed into an iterative solver (Euler forward step method) to determine the temperature evolution of all simulated nodes as well as the associated conditioning load in each scenario. The logic first evaluated the hollow core surface temperature and compared it against the exterior air temperature. If the outdoor air was cooler than the slab surface, the heat transfer rate was set equal to the rate determined though eq(52); otherwise, the heat transfer rate was set to zero. The radiosity of each interior surface was then evaluated in order to determine the net radiative heat transfer rate to each surface. The mean radiant temperature was then determined using the interior surface temperatures as well as the surface view factors to the occupant, yielding the operative temperature of the time step given the air temperature. The heat flux through the exterior assemblies as well as the internal gains to the space were then resolved to determine the heat rate to the zone in the given time step. The required post-cooled ambient air temperature was determined based on the heat rate to the zone as well as desired ambient air temperature.

During periods of occupancy and cooling, the change in air temperature was defined as the difference between the air temperature and the required post-cooled air temperature. During all other periods (non-occupied or no cooling required), the temperature change was defined by the heat rate to the zone. Therefore, during periods of occupancy and cooling, the cooling load was set equal to the heat rate to the zone plus the heat rate required to achieve the required air temperature change in the given time step. During all other periods, the cooling load was off and the ambient air temperature naturally evolved. The heat transfer rate to, and temperature change of all other nodes were then evaluated and the process was repeated at the next time step. Upon completion of the simulation, the PMV and PPD metrics were evaluated using the simulation results as an input. The scripts for the heat transfer engine and thermal comfort calculator can be found in Appendices A and B respectively.

6.0: Results and Analysis

6.1: Interior Surface Temperatures

Average Surface Temperature by Assembly:

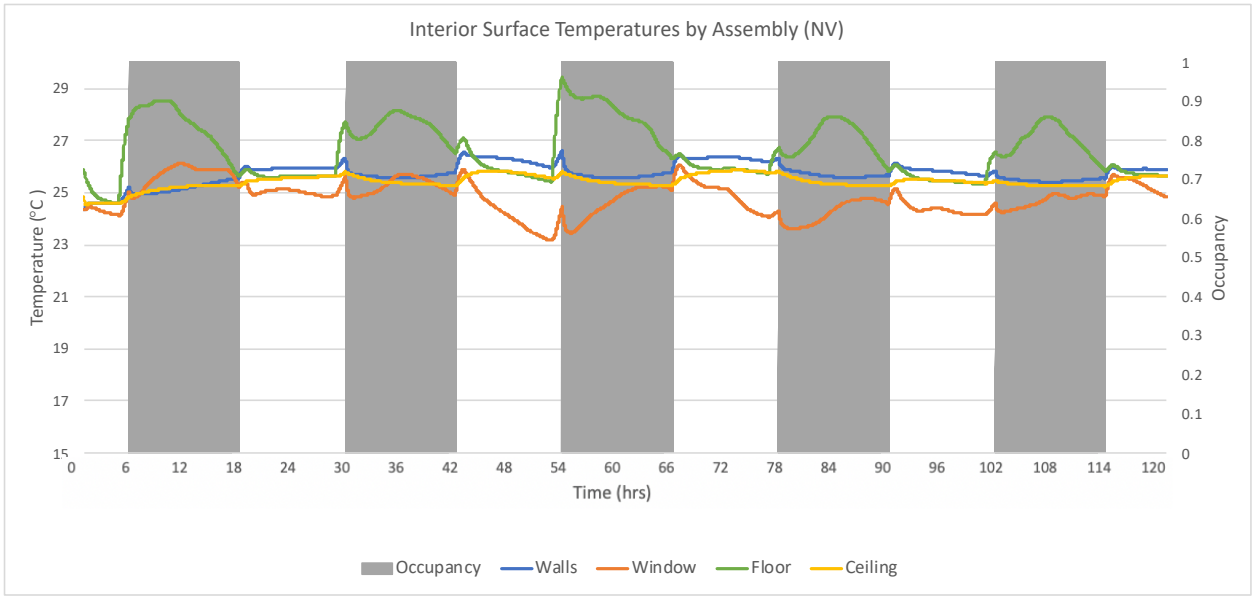

Figure 6.1 *– Average Interior Surface Temperatures by Assembly; Summer Design Week (NV)*

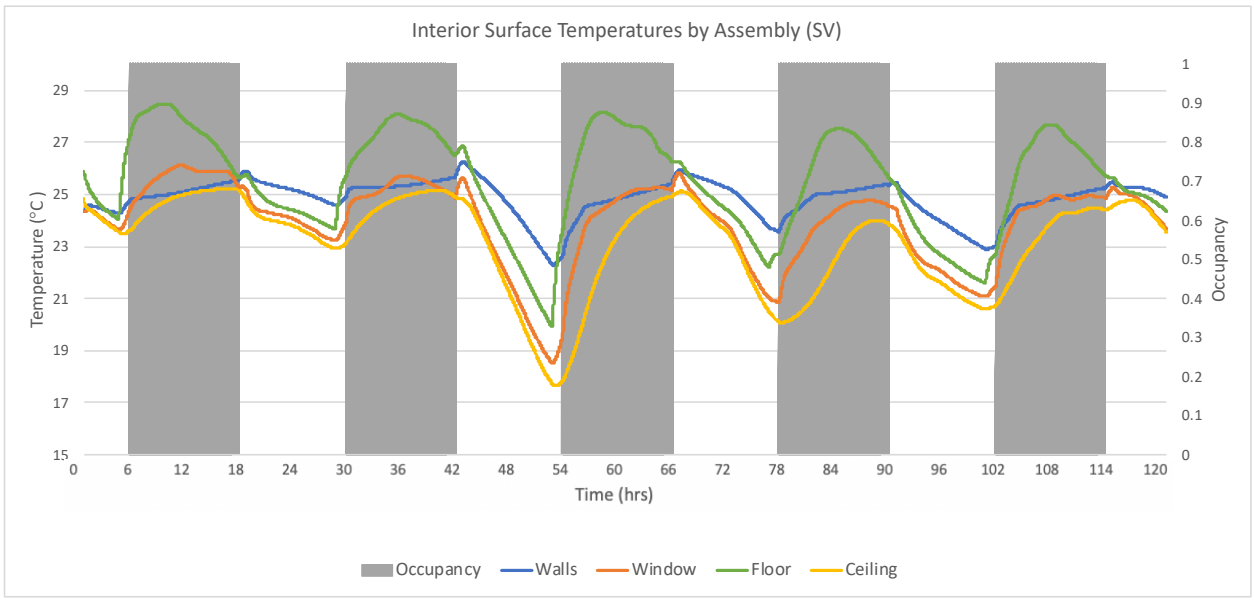

Figure 6.2 *– Average Interior Surface Temperatures by Assembly; Summer Design Week (SV)*

For proof of concept of the system, equal initial conditions are imperative to demonstrate the effect of the system on the surroundings. Lower initial temperatures in the SV comparison are expected in reality as the idea of the system is to cool the slab which will then cool the surrounding interior surfaces. However, artificially reduced initial temperatures would skew the results of the system in favour of the desirable outcome (reduced cooling load associated with SV). For this reason, the initial surface temperatures of the NV and SV scenarios were set to be equal, as can be observed in Figures 6.1 and 6.2 It should also be noted that all node temperatures were set to equal amongst the explored scenarios. That is to say, the initial temperature of any node was equal in both the NV and SV scenarios. Initial temperatures were determined through iteration of the NV model in which initial temperatures were increased/decreased by 0.5°C until stability amongst all initial temperatures was achieved. Temperatures were deemed stable when the heat flux between nodes was less than the heat flux imposed by the boundary conditions. This was done to minimize heat transfer associated with the initial conditions of the system, minimizing the initialization period of the NV scenario. Initial temperatures of all nodes in both SV and NV scenarios are summarized in Table 6.1.

Table 6.1 – Initial Temperature of Nodes by Assembly and Node (°C)

Surface	**1**	**2**	**3**	**4**	**5**	**6**	**7**	**8**	**9**	**0**
Node										
1	24.5	24.5	24.5	24.5	24.5	24.5	24.5	24.5	26	25
2	24.5	24.5	24.5	24.5	23	23	23	23	-	23
3	28	28	27	27	-	-	-	-	-	-
4	32	33	30	35	-	-	-	-	-	-

From the Figures 6.1 and 6.2, it can be observed that the average assembly temperatures are quite similar during the first day, while the temperatures of the SV scenario drop lower than that of the NV scenario during the first night. The phenomenon is also observed to a greater extent in the second, third, and fourth nights; suggesting that the slab experiences less cooling during the first night than the second, third, and fourth nights. As illustrated in Figure 4.10, the boundaries of node 2 of the slab are the exterior air temperature and the temperature of node 1 of the slab. The temperature profile of node 2 of the slab as well as associated influencing parameters are shown in Figures 6.3 and 6.4 respectively.

Slab – Node 2

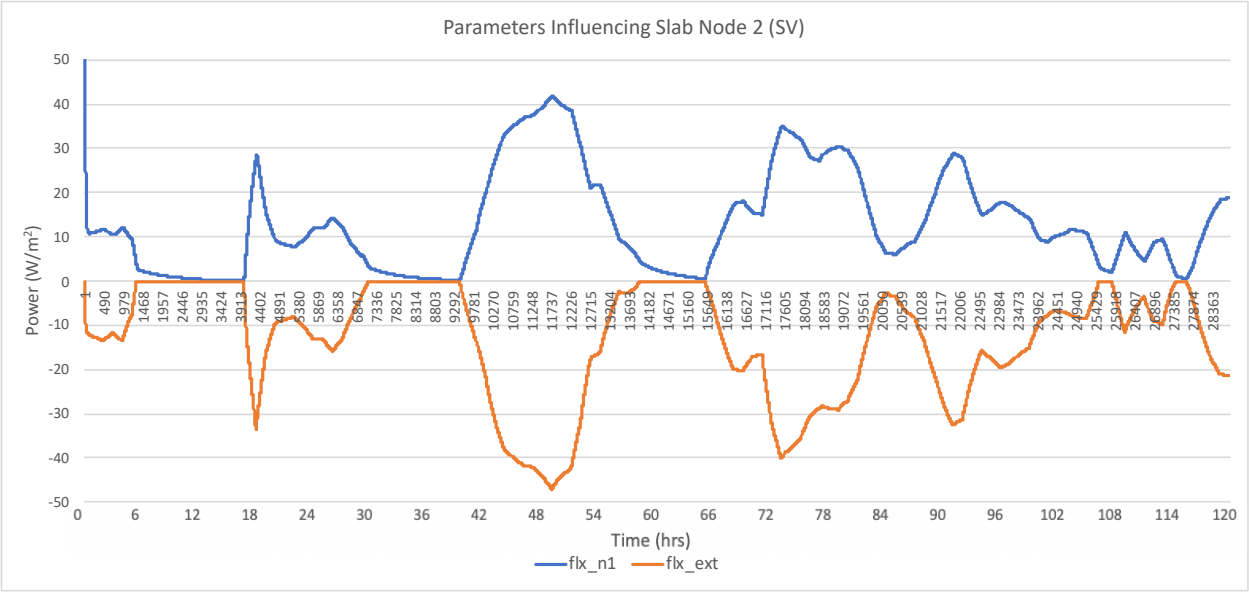

Figure 6.3 *– Parameters Influencing Slab Node 2 (SV)*

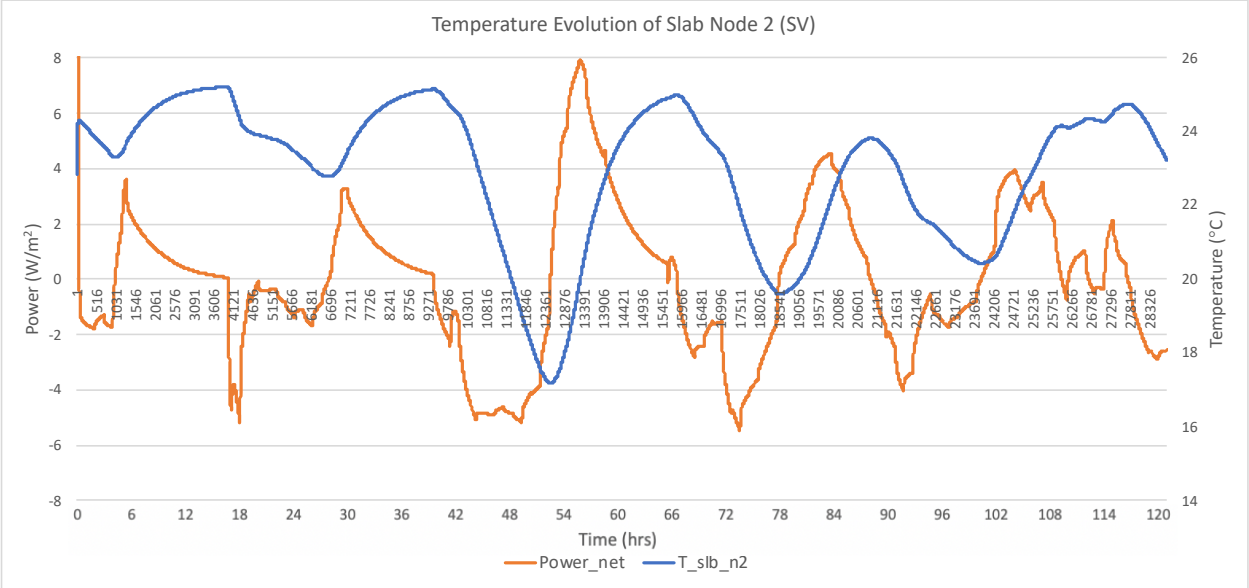

Figure 6.4 *– Temperature Evolution of Slab Node 2 (SV)*

Flx_n1 and flx_ext denote the heat flux from slb_n2 to slb_n1 and the outdoor air stream respectively. Power_net and T_slb_n2 denote the net energy flow to, and temperature of slb_n2. The thermal resistor coupling slab node 2 (slb_n2) to the exterior air is equal to half the resistance of slb_n2 plus the resistance of the forced convection heat transfer coefficient realized in the slab, while the resistor coupling slb_n2 to slab node 1 (slb_n1) of the slab is equal to half the resistance of slb_n2 and

half the resistance of slb_n1. Recalling that the slab is considered homogeneous in composition and thickness across the section and the thicknesses of n1 and n2 are 5cm and 1cm respectively, the thermal resistance between slb_n2 and slb_n1 is approximately four times smaller than the thermal resistance between slb_n2 and the exterior.

As illustrated in Figure 6.3, the power from slb_n1 to slb_n2 seems to be equal to the power from slb_n2 to the exterior. Upon further investigation, it can be observed that the power from slb_n1 is slightly lower, and lags slightly behind the power to the exterior. This is due to the thermal inertia inherent to the high thermal mass of the slab, as well as the thermal coupling between nodes. When the slab under goes ventilation, negative power (cooling) is imposed by the exterior boundary of the system. In a perfectly coupled system that experiences zero thermal resistance between boundaries of infinite heat capacity, this negative power would instantaneously (as opposed to over the course of the time step) evolve the temperatures of the nodes in the network such that the power between all nodes is equal to the negative power imposed by the exterior boundary. However, because the modelled system experiences thermal resistance, the power imposed by the exterior results in a temperature change of slb_n2, which then causes a flux between slb_n1 and slb_n2 proportional to the temperature difference; and inversely proportional to the thermal resistance between the nodes. The thermal resistance between the nodes (limiting power) and heat capacity of the nodes (limiting temperature change) results in a time lag and amplitude reduction in the power imposed by slb_n1 compared to the power imposed by the exterior boundary.

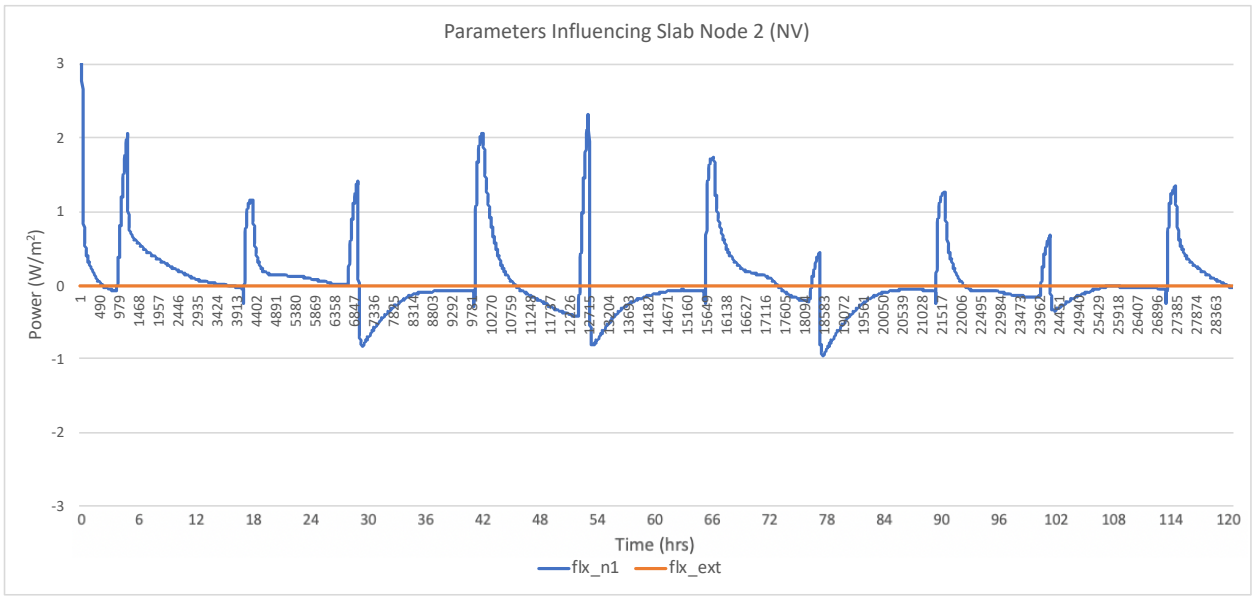

Figure 6.5 *–Parameters Influencing Slab Node 2 (NV)*

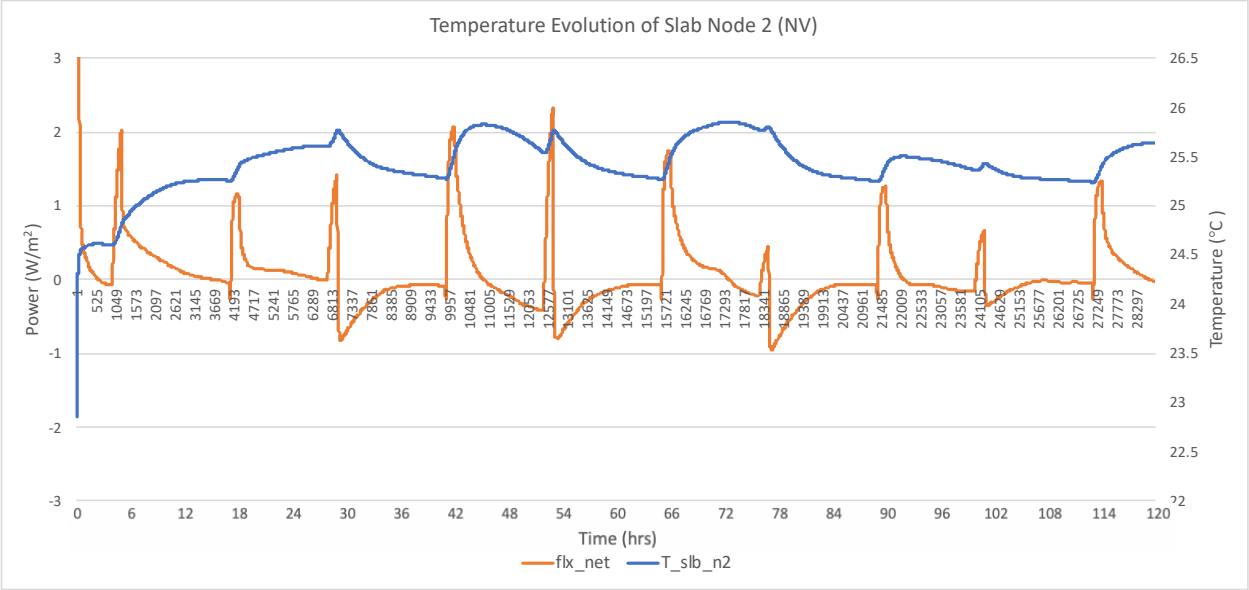

Figure 6.6 *–Temperature Evolution of Slab Node 2 (NV)*

In the NV scenario, the power to the exterior is eliminated as the temperature in the hollow core is assumed to be equal to the temperature of slb_n2. Unlike the SV scenario, the power to slb_n2 is at its greatest at the beginning and ends of the day, aligning with the high solar gain periods; while the SV scenario experiences greatest power at night, when the temperature difference between the slab and the exterior air is greatest. This is a direct result of the slab night cooling overpowering the solar gains in the ventilated scenario. For the same reason, the magnitude of power to slb_n2 is rather small compared to the power experienced by slb_n2 in the ventilated scenario. From this, it can be deduced that the temperature evolution of slb_n2 is primarily impacted by the exterior boundary when undergoing ventilation; and is primarily impacted by interior conditions otherwise, which dictate the temperature evolution of slb_n1. The effects of interior conditions on the temperature evolution of slb_n1 are discussed in the next section.

Node 1 Naming Convention

Flux_int and flux_n2 denote the heat flux from the node in question to the interior air and adjacent node in the assembly respectively. Phi_Rad represents radiative heat transfer from surrounding surfaces while Gains_int represent internal gains being delivered to the node being evaluated. Power_net and T_slb_n1 denote the net energy flow to, and temperature of the node being evaluated.

Slab – Node 1

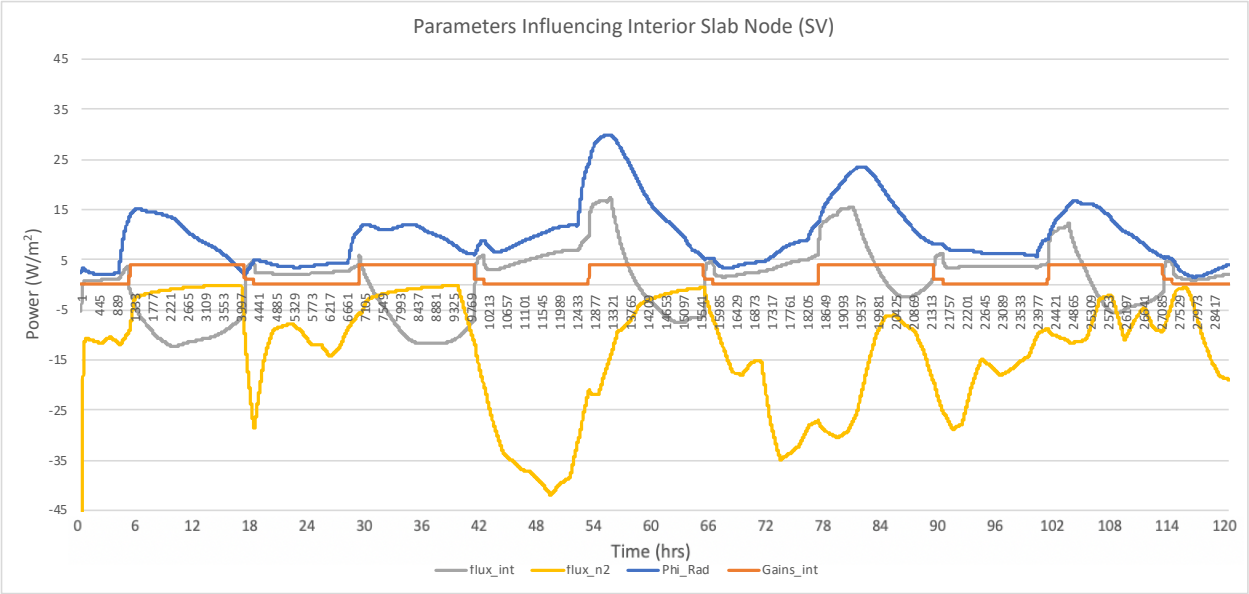

Figure 6.7 *– Parameters Influencing Slab Node 1 (SV)*

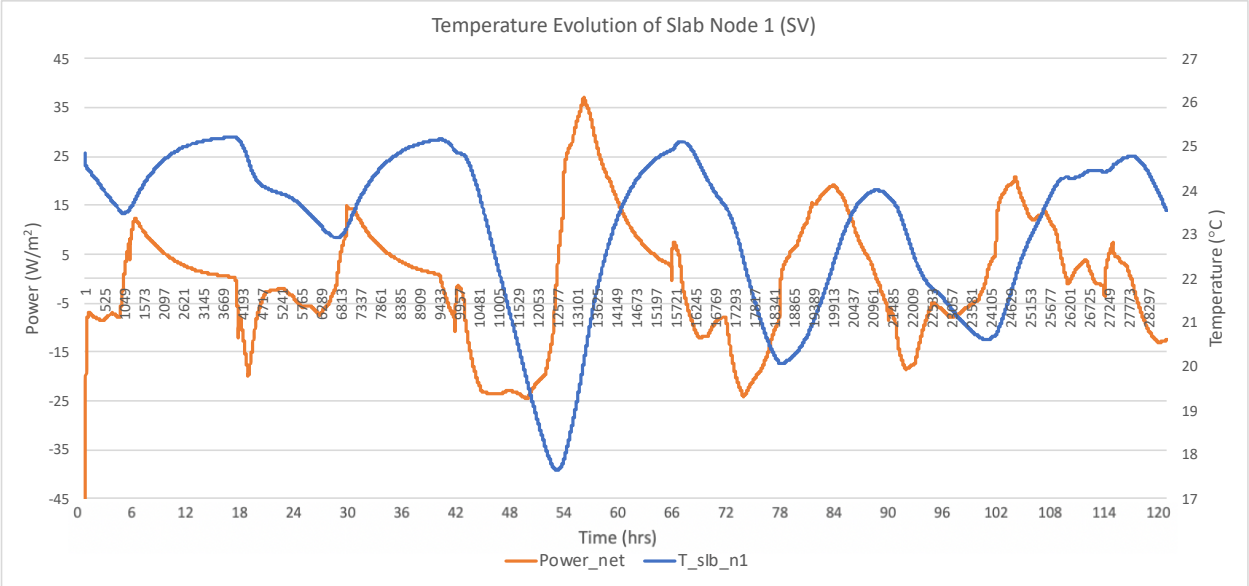

Figure 6.8 – *Temperature Evolution of Slab Node 1 (SV)*

The interior slab surface temperature (node 1) is influenced by conductive heat transfer across the slab nodes, as well as convective and radiative heat transfer with the interior air and surrounding surfaces respectively. Slb_n1 is coupled to the interior surface by a resistor equal to half the resistance of slb_n2, and slb_n1 is coupled to the interior air and surfaces by convective and radiative thermal

resistors. The power delivery to slb_n1 is shown in Figure 6.7, while the temeprature evolutuion of slb_n1 is illustrated in Figure 6.8.

From Figure 6.8 and the previously discussed Figure 6.4, the net power to nodes slb_n2 and slb_n1 are extremely similar due to the large power imposed on slb_n2 by the exterior and the low thermal resistance coupling the nodes. Although slb_n1 experiences substantial internal power sources, the occurance of these power sources (primarily lighting and interior radiaiton) are misaligned with the power to slb_n2 imposed by the exterior. This results in a temperature reduction of the slab at night when the building is unoccupied (low internal gains and solar radiaiton) and exterior temperature is low (high power out of slab), and a temperature increase during the day when the opposite is true. Given the temperature reduction at night, the slab has the ability to act as a heat sink to the inteior air during the day, as it evidenced through periods of positive flux to the slab from the interior during the day. This flux is reduced as the slab increases in temperature throughout the day (absorbing gains) and eventually becomes negative when the slab temperature exceeeds the interior air temperature. This heat sink behaviour is also exhibited through the high and positive radiative heat tranfer to the slab from the interior surfaces, stemming from a greater and consistently positive temperature difference between the slab and surrounding surfaces.

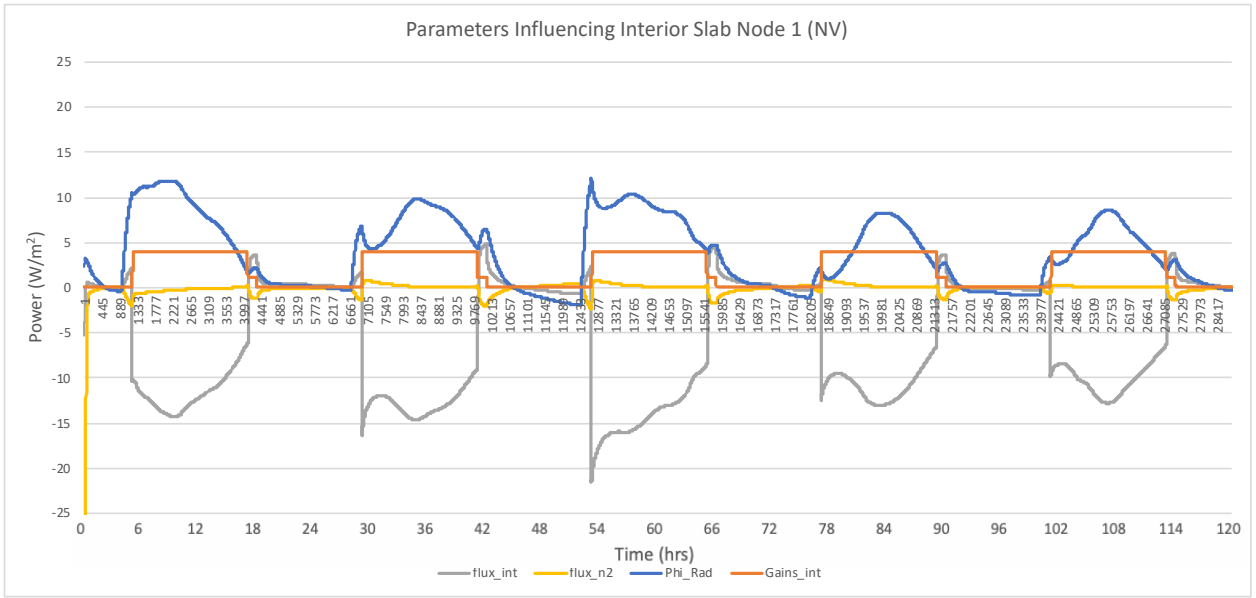

Figure 6.9 *– Parameters Influencing Slab Node 1 (NV)*

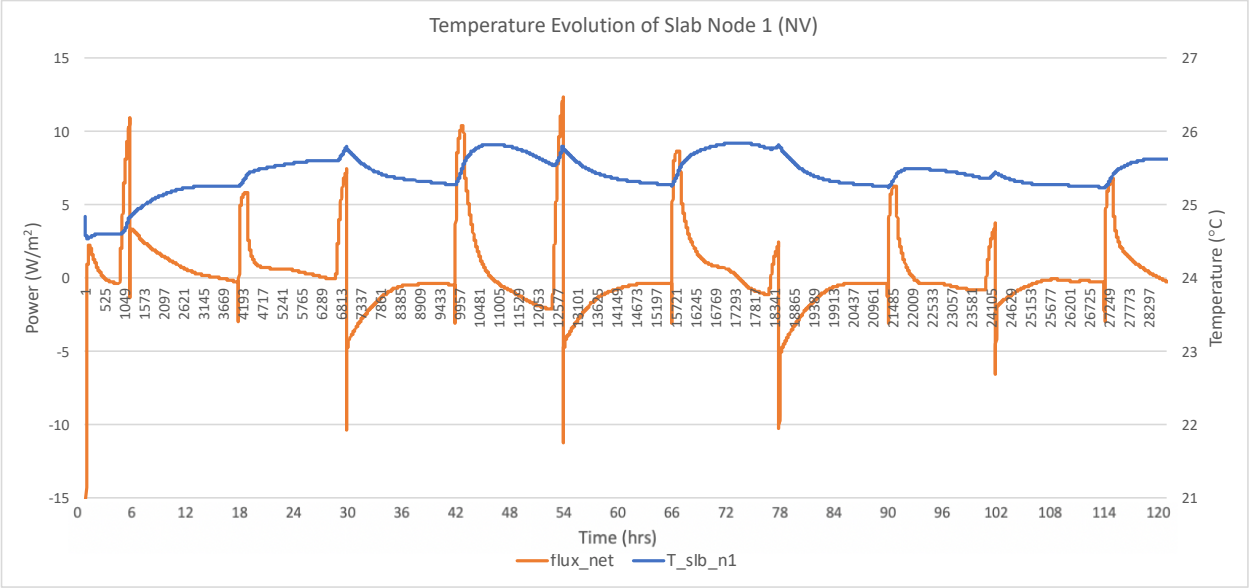

Figure 6.10 *– Temperature Evolution of Slab Node 1 (NV)*

In contrast to the SV scenario, the NV scenario experiences significantly lower power range, resulting in a reduced net power and temperature range. While in the SV scenario, the flux to slb_n2 was the primary power source, the NV scenario is primarily dominated by convective heat transfer to the interior air and radiative heat transfer from the surrounding surfaces. What's more, the power to the air seems to align well with the power from surrounding surfaces. This is explained by the operative temperature condition, which calls for an inverse proportionality between mean radiant temperature and interior air temperature. That is to say, and increase in mean radiant temperature requires a reduction in interior air temperature, resulting in both an increase in radiative heat transfer to the slab and convective heat transfer to the interior air. As discussed in the temperature evolution of slb_n2 in the SV scenario, the slb_n1 experiences a lag in temperature evolution due to the difference in thermal resistance between the slab and the air, and the slab and the surrounding surfaces. This results in a high power delivery in the morning when occupancy begins and solar gains are high, with power being reduced over time as the slab increases in temperature form absorbing the gains. The power delivery to the slab is positive for most of the duration of occupancy, then becomes negative when the internal and solar gains are no longer present to offset the negative power to the interior air and surrounding surfaces. The net heat flux experiences an abrupt increase in the early morning aligning with the increase in interior radiative heat transfer associated with the solar gains entering the space. An abrupt decrease is observed when the interior space is conditioned (aligning with the decreased in interior flux) then increases again at occupancy (aligning with the increase in internal gains).

Floor – Node 1

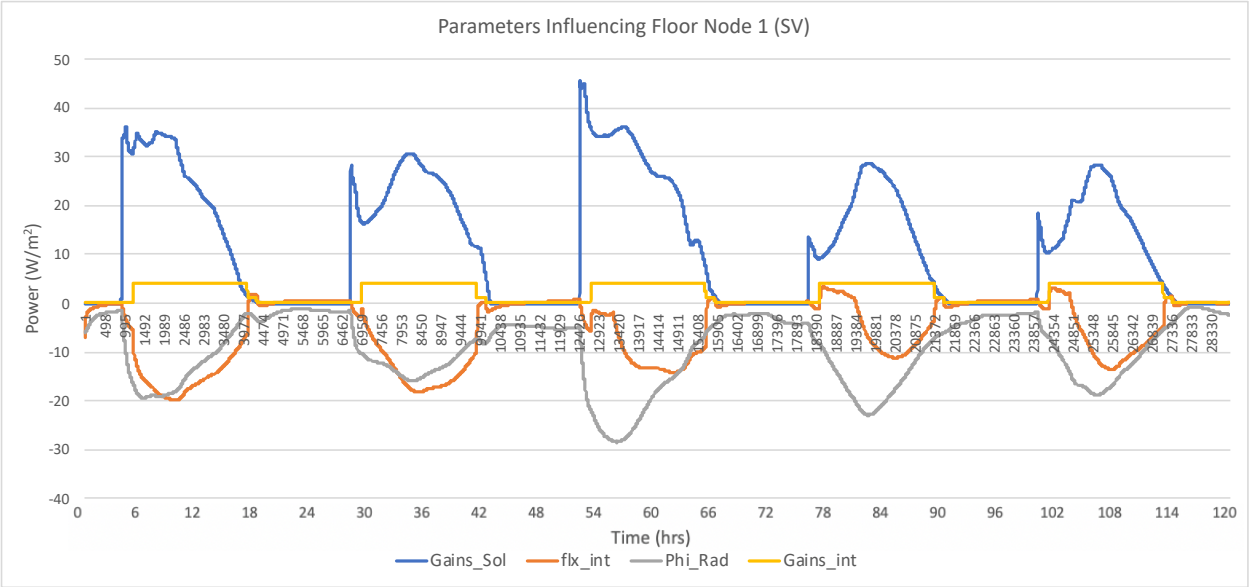

Figure 6.11 – *Parameters Influencing Floor Node 1 (SV)*

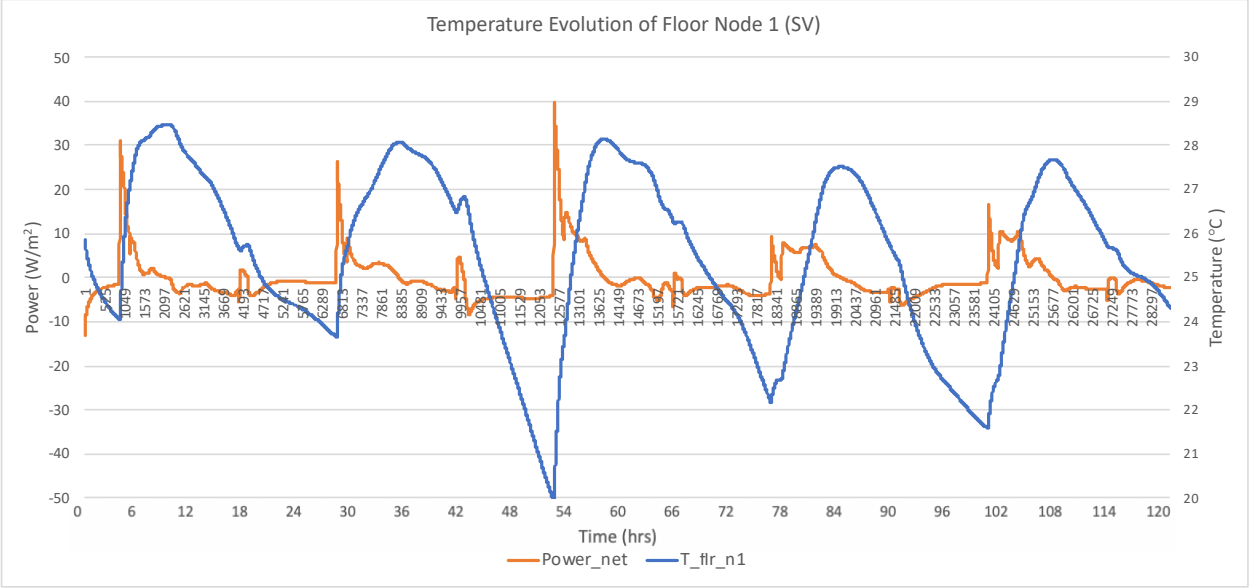

Figure 6.12 – *Temperature Evolution of Floor Node 1 (SV)*

As illustrated in Figures 6.11 and 6.13 the floor temperature increases dramatically and abruptly in the mornings of both the SV and NV scenarios due to the high amount of solar radiation entering the simulated zone, shown in Figure 5.6. The building experiences a high amount of solar gain to the interior in the morning when the sun is low and in the east due to the east/west orientation of the building; resulting in maximum solar gains though transparent assemblies to the interior. This solar gain rapidly

increases the temperature of the floor, increasing the convective and radiative heat transfer to the air and surrounding surfaces respectively. The convective heat flux reduces to a negative value when the floor temperature is greater than that of the interior ambient air; as does the radiative heat transfer when the floor temperature is greater than that of the mean radiant temperature experienced by the floor.

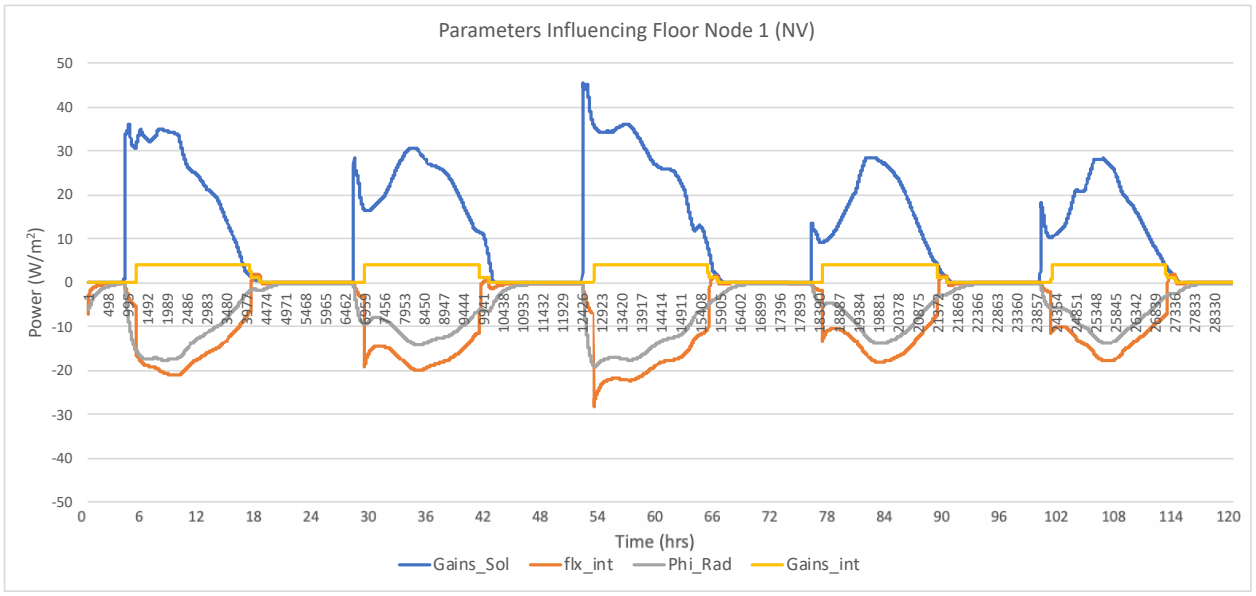

Figure 6.13 – *Parameters Influencing Floor Node 1 (NV)*

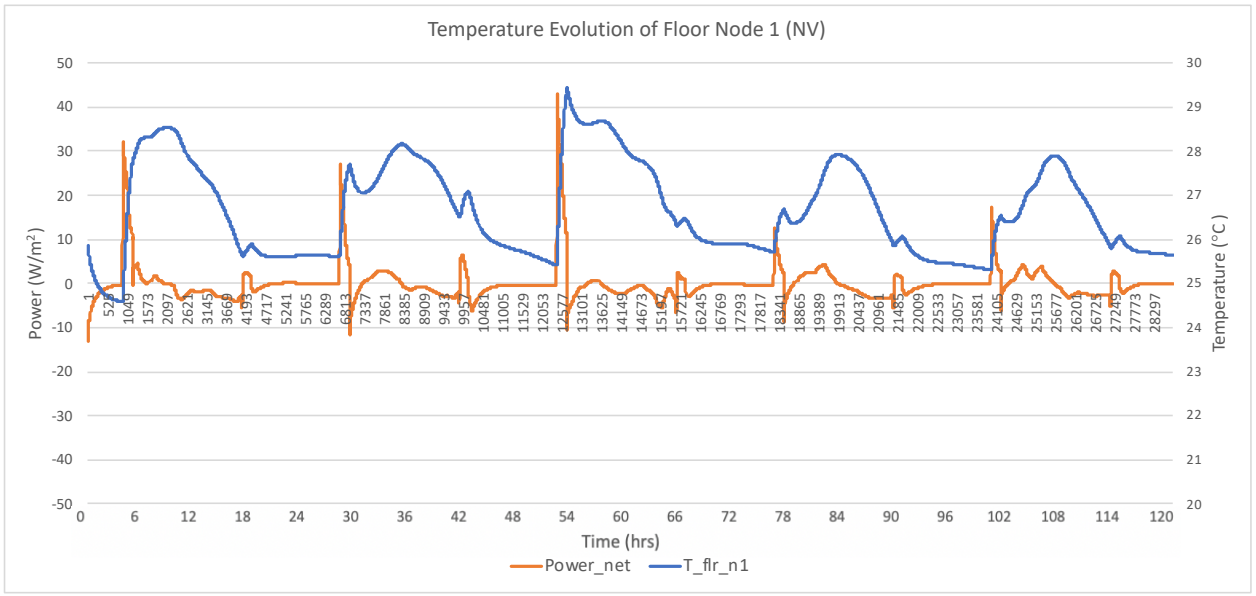

Figure 6.14 – *Temperature Evolution of Floor Node 1 (NV)*

The same rapid warming that occurs in the SV scenario is also evident in the NV scenario, however, the NV scenario experiences a narrower temperature range. Furthermore, it can also be observed that the SV scenario experiences lower minimum and maximum floor surface temperatures, specifically during the second night and third day of the simulation. This is due to the slabs high degree of thermal mass activation during the second night, as illustrated through the low slab temperature in the SV scenario discussed earlier; supporting the ability to act as a heat sink for the surrounding environment.

Given the large view factor of the floor to the ceiling, the slab has the ability to cool the warm floor effectively through radiation, evidenced though the substantially lower minimum floor surface temperature in the SV scenario (<20C) compared to the NV scenario (>25C) during the third night. The effect of this precooling is also observed in the maximum temperature experienced by the floor in a given period. After the coolest night (2nd night), the floor experiences the maximum solar load of the simulation period. The ability of the slab to purge excess heat to the exterior during the cool night in the SV scenario precools the interior surfaces, increasing the ability for these surfaces to act as a heat sink during the day. In the SV scenario, the floor experiences a lower surface temperature (~28C) compared to the NV scenario (>29C) due to the ability for the surrounding surfaces to absorb the re-radiated solar gains. Although this peak temperature difference is lower than the difference in minimum temperatures, it can be observed that the peak temperature in the SV scenario occurs slightly later in time than the NV scenario. Furthermore, the NV scenario experiences a lower duration of floor high temperatures, as shown in the gradual increase of floor temperature in the SV scenario compared to the abrupt temperature increase in the NV scenario. This rather significant difference in the rate of change of the floor temperature is a direct result of the cooling capacity of the slab in the SV scenario, allowing the floor to radiate to the comparatively cooler surfaces. In the NV scenario, the surrounding surfaces have the ability to absorb radiation from the floor, but to a lesser degree due to the greater surface temperatures compared to the SV scenario. Once the cooling capacity of the slab and surrounding surfaces is exhausted and the net power delivery to the node is negative, the floor temperature decays at roughly the same rate in the both the SV and NV scenarios. The floor continues to cool to a lower temperature in the SV scenario than in the NV scenario due to the radiative cooling effects of the cooled slab associated with night ventilation.

Walls – Node 1

Due to the variation in solar radiation striking each wall associated with the sun path, each wall was treated as a unique surface in the simulation. This treatment was vital in evaluating the exterior surface temperature due to the significant difference in solar power delivery among the surfaces. The effect of varying solar power has reduced impact on interior node temperatures due to the high thermal mass of the brick and high thermal resistance of the assembly. Given that the magnitude of temperature change of a node is inversely proportional to the thermal resistance between nodes and the heat capacity of the node, thermally massive and highly insulative materials have the ability to moderate the temperature change of nodes within the assembly.

The presence of brick on the outer surface of the wall allows the wall assembly to absorb the intense solar radiation striking the surface in exchange for a small temperature change in a given time step compared to a material of lesser heat capacity. Furthermore, the presence of XPS inboard of the brick further reduces the temperature change of the node inboard of the XPS due to the high thermal resistance of the XPS impeding energy flow. For these reasons, the heat transfer occurring inboard of the XPS layer was assumed to be similar among all walls (eliminating the unique effects of solar radiation), and the walls were therefore treated as similar for the analysis. All parameters discussed in this section consider the average values of the four walls being explored.

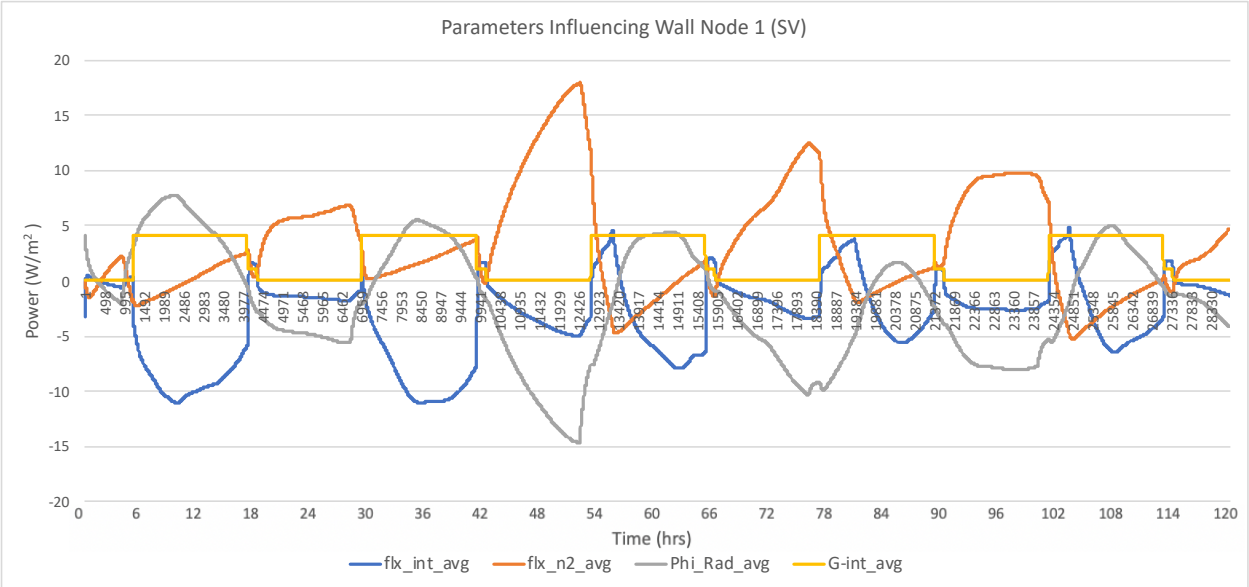

Figure 6.15 – *Parameters Influencing Wall Node 1 (SV)*

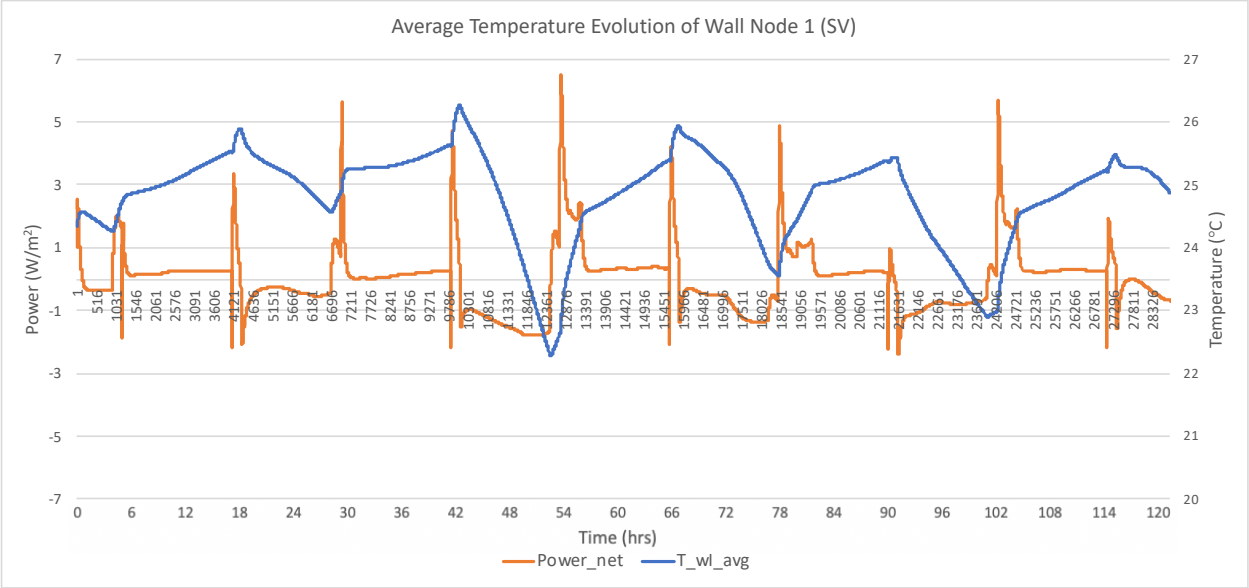

Figure 6.16 – *Average Temperature Evolution of Wall Node 1 (SV)*

From Figure 6.15, it can be observed that the flux to the interior is almost solely negative, and the flux from the adjacent node (n2) is primarily positive, suggesting that the interior ambient air temperature is almost always cooler than the wall temperature; and the concrete block node is almost always warmer than the interior surface node. This notion is supported by the high solar heat gain imposed on the exterior during the day, and the low internal heat sources during the night. The flux to the adjacent node reaches a negative value shortly after sunrise when solar gains are the highest as well as subsequent to occupancy when internal gains are high. This is caused by the solar/internal gains warming the interior surface to a temperature greater than the adjacent node, causing heat flux from the adjacent node to reduce to below zero.

Radiative heat transfer from surrounding surfaces can also be observed to be primarily negative, only reaching positive values for a period within the occupied period, as is pronounced in the third, fourth, and fifth days. Due to the cooling of the slab and thus surrounding interior surfaces, the net radiation reaching the surface is primarily negative (i.e. the wall is warmer than the experienced mean radiant temperature). However, during the day, the surfaces increase in temperature due to the high solar radiation reaching the zone through the windows and increased internal gains. The conductive heat flux to the adjacent node typically becomes negative when the radiative heat transfer to the interior node is positive; however, due to the action of the exterior boundary and the thermal inertia of the nodes, a slight lag is observed.

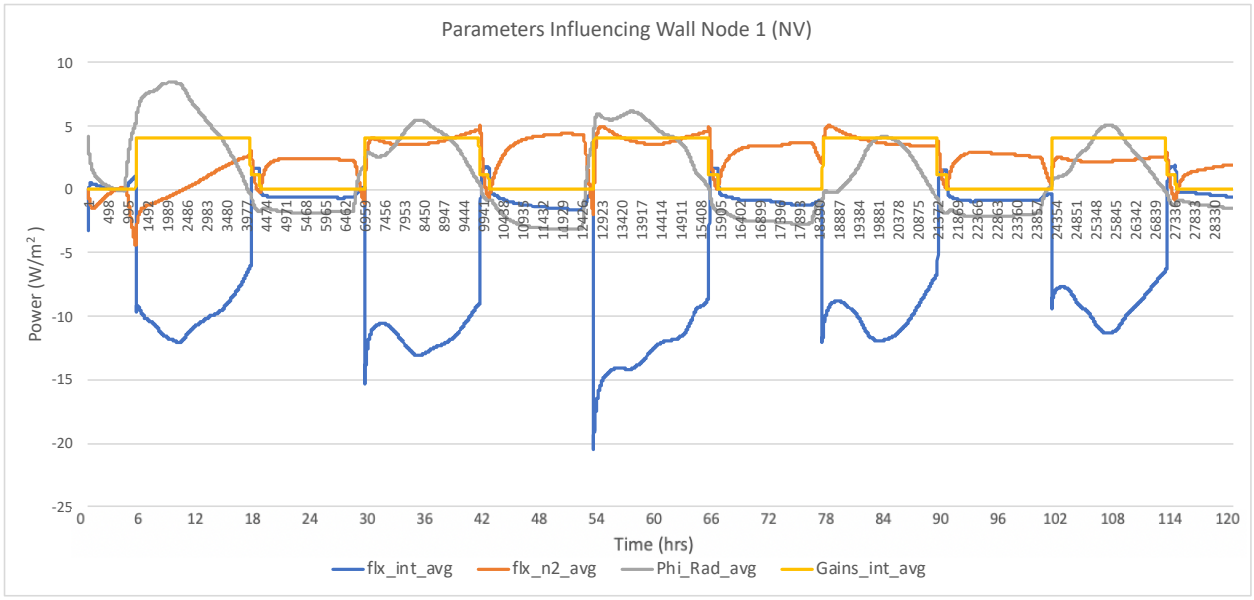

Figure 6.17 – *Parameters Influencing Wall Node 1 (NV)*

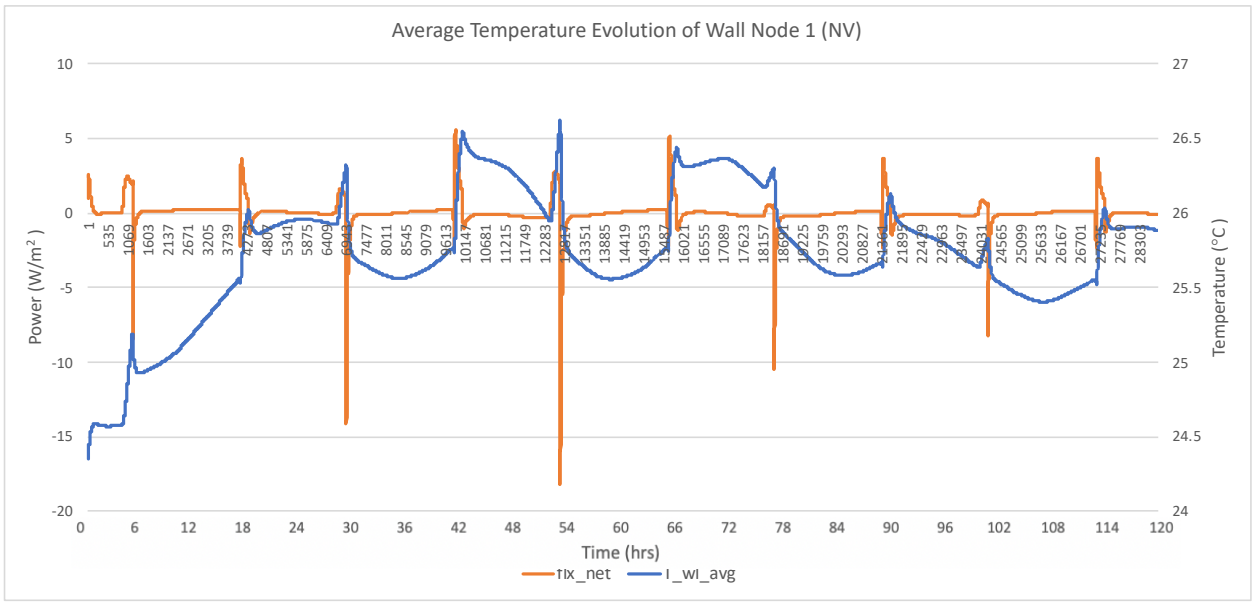

Figure 6.18 – *Average Temperature Evolution of Wall Node 1 (NV)*

As in the SV scenario, the flux to the interior air is primarily negative and the flux to the adjacent node is primarily positive in the NV scenario for the same reasons discussed above. In contrast, the radiative heat transfer from surrounding surfaces is shifted up and the amplitude is decreased due to the lack of radiative cooling available. Although the peak temperature in the SV scenario is only about 0.25C cooler than in the NV scenario (end of second day), a much lower minimum temperature is realized; supporting radiative cooling to surrounding surfaces and the occupant.

Windows – Node 1

As with the walls, the windows were treated as unique surfaces in the simulation to address the difference in solar radiation striking each surface based on the sun path. Unlike the wall assemblies, the windows lack layers with temperature attenuating effects of high thermal mass and thermal resistance layers, negating the ability to treat these surfaces as a single surface. However, unlike the walls, the windows are mostly transparent to shortwave solar radiation, resulting in only about 5% absorption of solar radiation. Although the magnitude of solar radiation is large, the amount absorbed by the glass surface is small, resulting in a small temperature change of the glass. Furthermore, the glass panes and window assembly as a whole have a low thermal resistance, resulting in heat being conducted through the assembly at a comparatively higher rate than the brick/XPS combination in the wall.

The brick/XPS combination allowed for similar temperatures of the node outboard the interior, resulting in similar heat transfer between the outboard node (n2) and the interior node, thus allowing for the simplification of all wall nodes to a single node. In contrast, the exterior window node absorbs significantly less solar radiation but distributes this radiation to a lower thermal mass. This heat is conducted rapidly through the window compared to through the wall, and is then distributed among all interior surfaces. The use of a small time step attenuates the drastic temperature change of the window when exposed to solar radiation, allowing for the simplification of all window nodes to a single node.

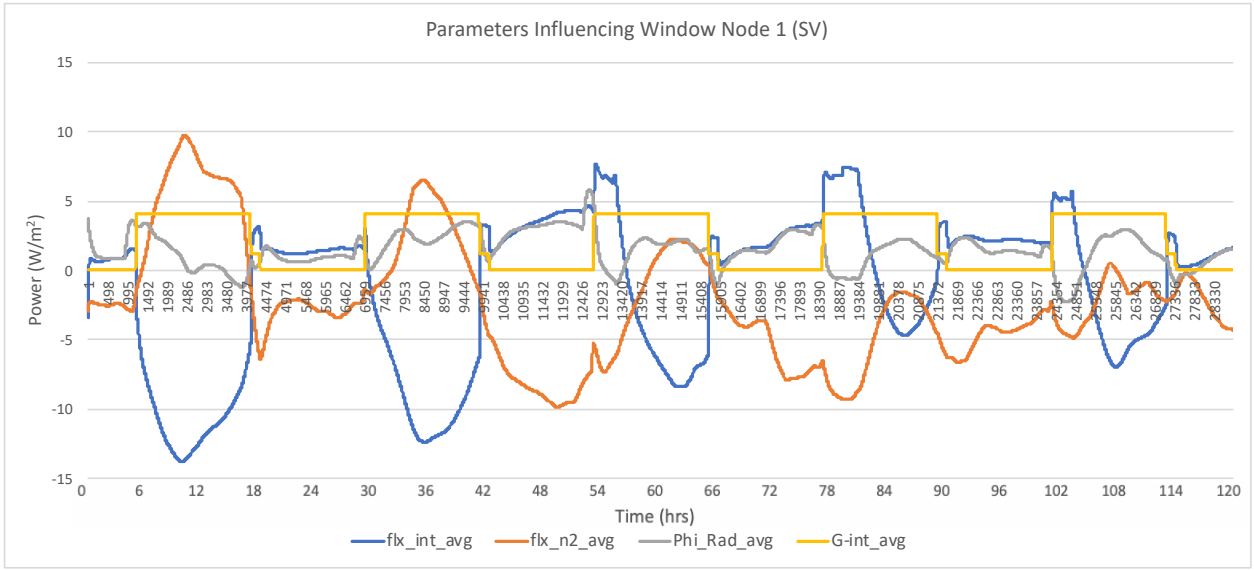

Figure 6.19 – *Parameters Influencing Window Node 1 (SV)*

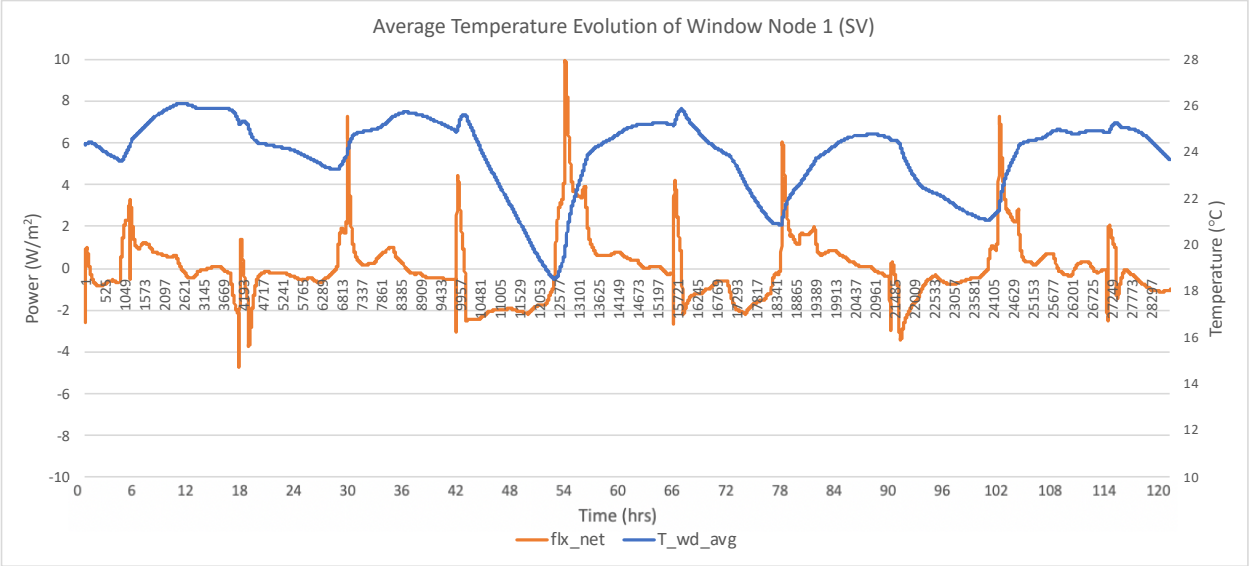

Figure 6.20 – *Average Temperature Evolution of Window Node 1 (SV)*

Unlike the behaviour of the wall, the window interior node experiences primarily negative flux from the adjacent outboard node in the SV scenario. This is due to the high interior node temperature during the day associated with internal gains; and the low exterior node temperature during the night, associated with the low thermal resistance of the window assembly and the low exterior temperature at night compared to the interior. Similarly, the window experiences a positive heat flux from the interior air until sunrise, after which, the slope decreases to a negative and the flux is reduced to a negative value until the late evening. This phenomenon is explained though the high degree of solar radiation striking the exterior of the window in the early morning as well as the increased exterior air temperature, warming the window and thus decreasing the temperature difference between the interior node and the ambient interior air. The temperature of the window surface continues to increase primarily due to the high exterior air temperature, surpassing the interior air temperature and resulting in negative flux from the interior air.

The radiative heat transfer from surrounding interior surfaces exhibits interesting behaviour in that it is primarily positive for the duration of the simulation. Recalling the low thermal mass and high conductivity of the window, there is minimal ability for heat to be trapped in the window assembly as any energy absorbed from the interior can easily be conducted through the assembly and removed through convection and radiation at the exterior. This is a unique attribute of the window as any energy absorbed by the wall assembly from the interior must overcome the high thermal resistance of the XPS layer and the high temperature of the exterior brick in order to be purged to the exterior. The

consistently positive value of radiative heat transfer suggests that although the interior surfaces are cooled by the slab, the mean radiant temperature experienced by the window is consistently higher than the interior surface temperature of the window. The wall experiences positive radiative HT during the day, suggesting that the floor warmed via solar radiation is overpowering the cooled slab. Because the window temperature is closely related to the exterior ait temperature due to the low thermal resistance, it is cooled to below the MRT it experiences by the time the heat of the floor is distributed.

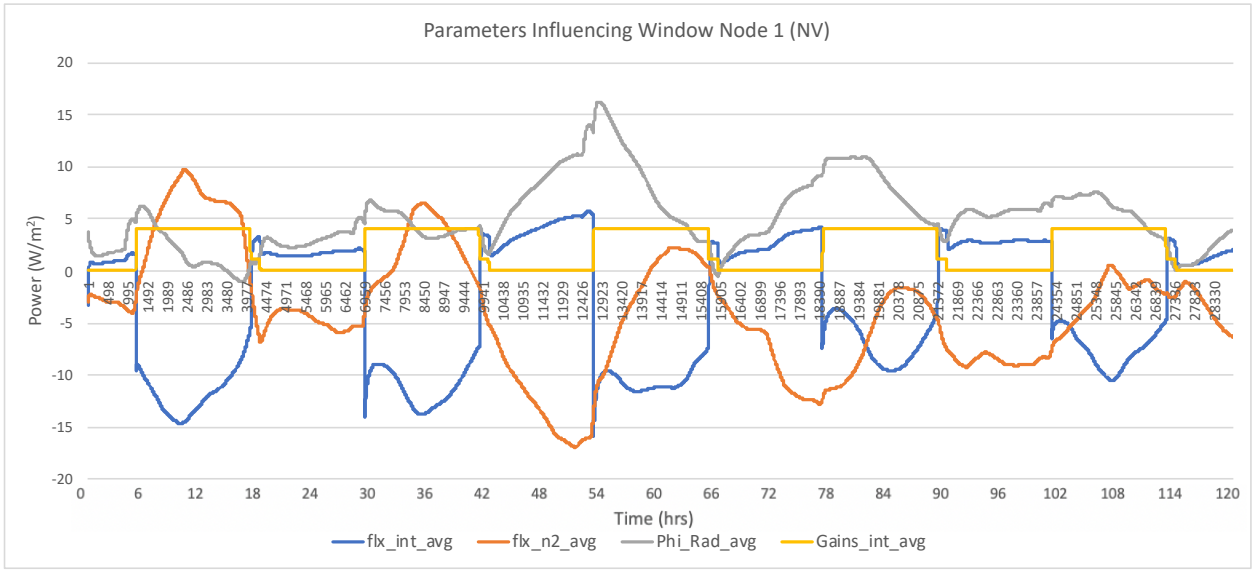

Figure 6.21 – *Parameters Influencing Window Node 1 (NV)*

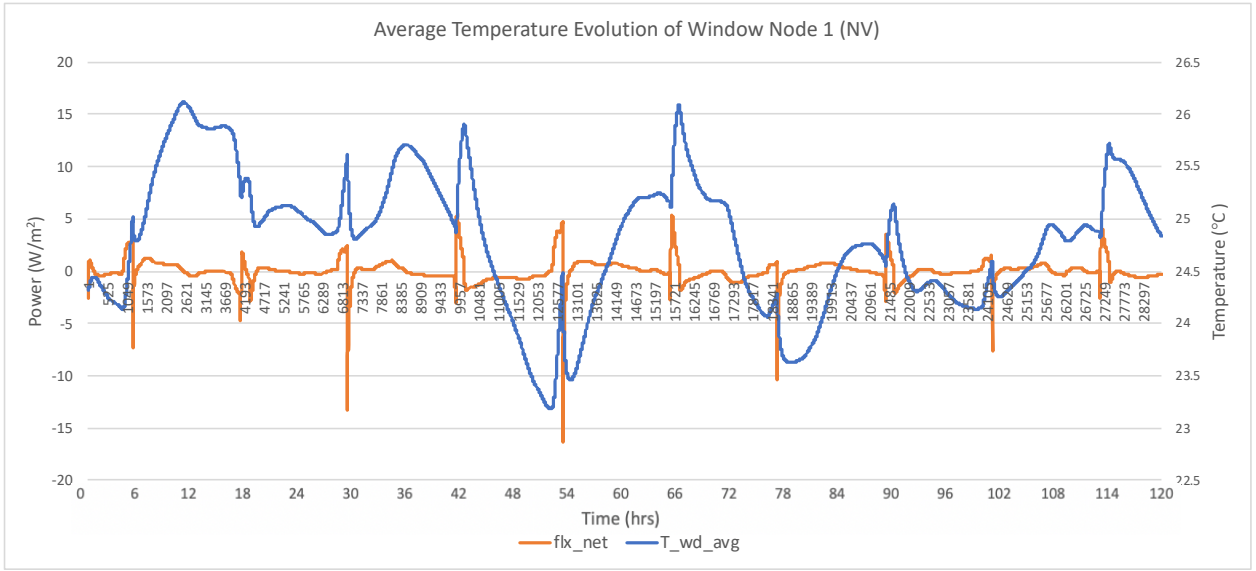

Figure 6.22 – *Average Temperature Evolution of Window Node 1 (NV)*

In comparison to the ventilated scenario, the interior node of the windows in the NV scenario experience a narrower temperature range and higher temperatures at each time step. This behaviour is similar to the wall in that the windows are radiatively cooled by the cooled slab. Additionally, the temperature difference between the NV and SV scenarios after the second night is about 4°C for both the walls and windows. This is somewhat counter intuitive as it is expected that the low thermal resistance between the window nodes would yield an interior temperature closer to that of the exterior temperature when compared to the interior and exterior node temperatures of the walls, given the substantially higher thermal resistance.

Evaluating the power sources acting on the interior window node, it can be observed that both scenarios experience a high negative flux from the exterior node, however, the SV scenario experiences substantially lower radiative heat transfer due to the cooled interior surfaces. This results in a reduced flux to the adjacent (exterior) node compared to the NV scenario due to the lower interior node temperature. The same phenomenon occurs with the walls during the second night such that in the SV scenario, the interior node experiences lower radiative heat transfer from the surrounding surfaces, reducing the heat flux to the adjacent outboard node. From this, it can be deduced that the effectiveness of purging energy to the exterior at night through the assembly is hindered by the radiative cooling of the interior surfaces present in the SV scenario. Therefore, although the windows have substantially lower thermal resistance than the walls, their ability to reduce in temperature through conduction through the assembly is hindered by the radiation received from the interior surfaces. In order for the windows to experience similar minimum temperatures at night between scenarios, the NV scenario would have to remove as much energy from the interior through the windows as the SV scenario achieves through the combination of windows and night ventilation.

6.2: Interior Conditions

As discussed in the previous section, the night cooling of the slab resulted in consistently cooler interior surface temperatures in the SV scenario than the NV scenario, reinforcing the idea that precooling building thermal mass can reduce the cooling load required by the space. In addition to the ability of the cooled surfaces to deliver less convective heat flux to the interior air, the cooled surfaces also have the ability to reduce radiative heat transfer to the occupant. As discussed in section 5.3, the operative temperature metric was used to evaluate the convective and radiative effects of reduced interior temperatures. Given that the interior surface temperatures are lower in the SV scenario than in the NV, the SV scenario can afford a higher interior ambient air temperature, not only decreasing the cooling load imposed by convective heat transfer from interior surfaces, but also reducing the cooling load of the system due to the increased setpoint temperature.

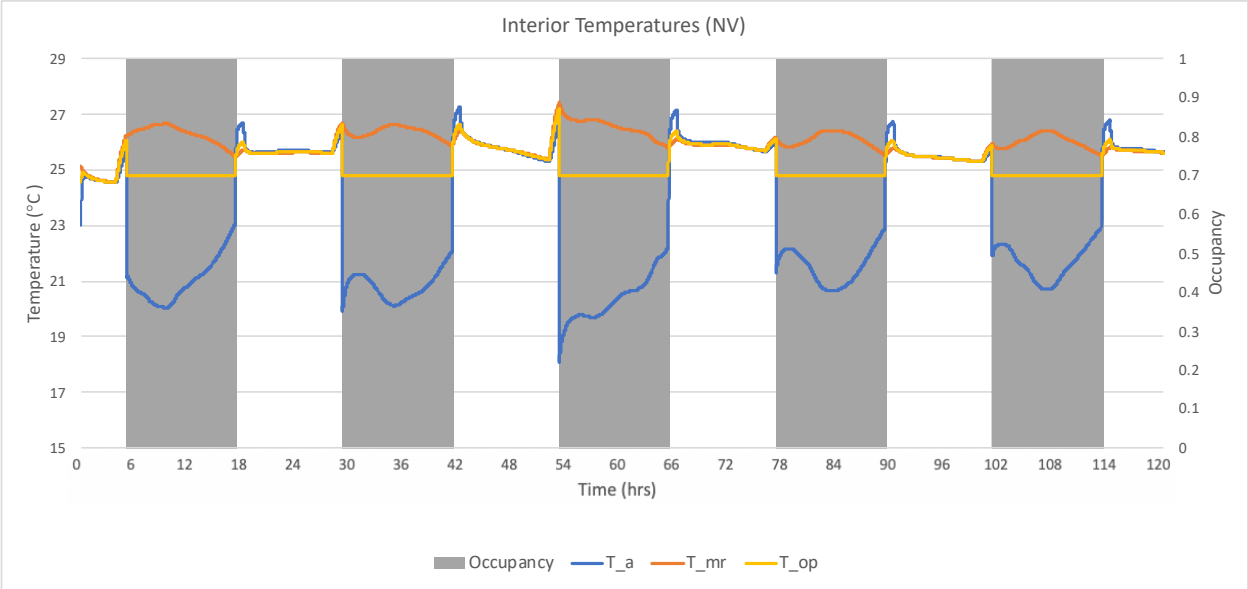

Figure 6.23 *– Interior Temperatures; Summer Design Week (NV)*

In the NV scenario, the operative temperature increases above the setpoint temperature in the evening during unoccupied periods when the building conditioning system is off and solar gains are present. The operative temperature reaches a local maximum then decreases once net power to the interior is negative due to the absence of solar gains and comparatively cooler exterior air. When the exterior air temperature increases and solar gains are imposed on the space in the early morning, the operative temperature increases. Upon occupancy, the conditioning system is turned on and cools the interior air to the temperature required to achieve the setpoint operative temperature based on the mean

radiant temperature. When the building is unoccupied, the conditioning system shuts off and the operative temperature is allowed to evolve naturally.

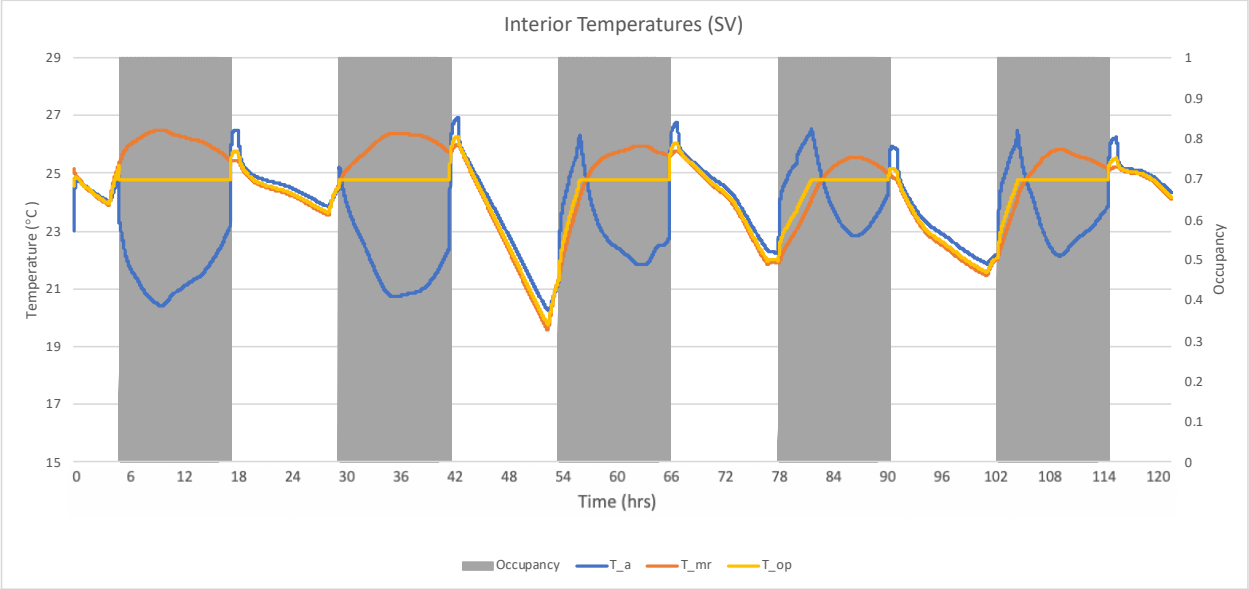

Figure 6.24 *– Interior Temperatures; Summer Design Week (SV)*

Unlike the NV scenario, the operative temperature in the SV scenario decreases below the setpoint operative temperature during the night due to the radiative cooling effects of the ventilated slab. This precooling effect is observed in the first night where the mean radiant temperature drops below the interior air temperatures, as is also observed to a greater extent during the second, third, and fourth nights. The mean radiant temperature (and associated operative temperature) then increases at a lower rate than in the NV scenario due to the precooled building thermal mass's ability to absorb interior gains. As in the NV scenario, the operative temperature is allowed to naturally evolve until cooling is required, after which the conditioning system cools the air to the required temperature. As can be observed in Figures 4.1 and 4.2, the duration of maximum operative temperature is much greater in the NV scenario than in the SV scenario due to the "overcooling" of the building thermal mass, resulting in a lower operative temperature than the setpoint operative temperature upon occupancy in the SV scenario. Given that the setpoint operative temperature is the temperature that *should* achieve the greatest level of occupant comfort, any temperature below the setpoint could result in reduced occupant comfort. It should be noted that the operative temperature can be increased by opening the ventilation system to the warm exterior air, introducing heat to the space. However, the dehumidifying energy cost would likely outweigh the benefit to the system. For this reason, heating via exterior air was not considered.

6.3: Occupant Comfort

Predicted Mean Vote (PMV) Comfort Metric

The PMV of a theoretical population exposed to the interior conditions produced in the simulated scenarios are outened in figure 6.25.

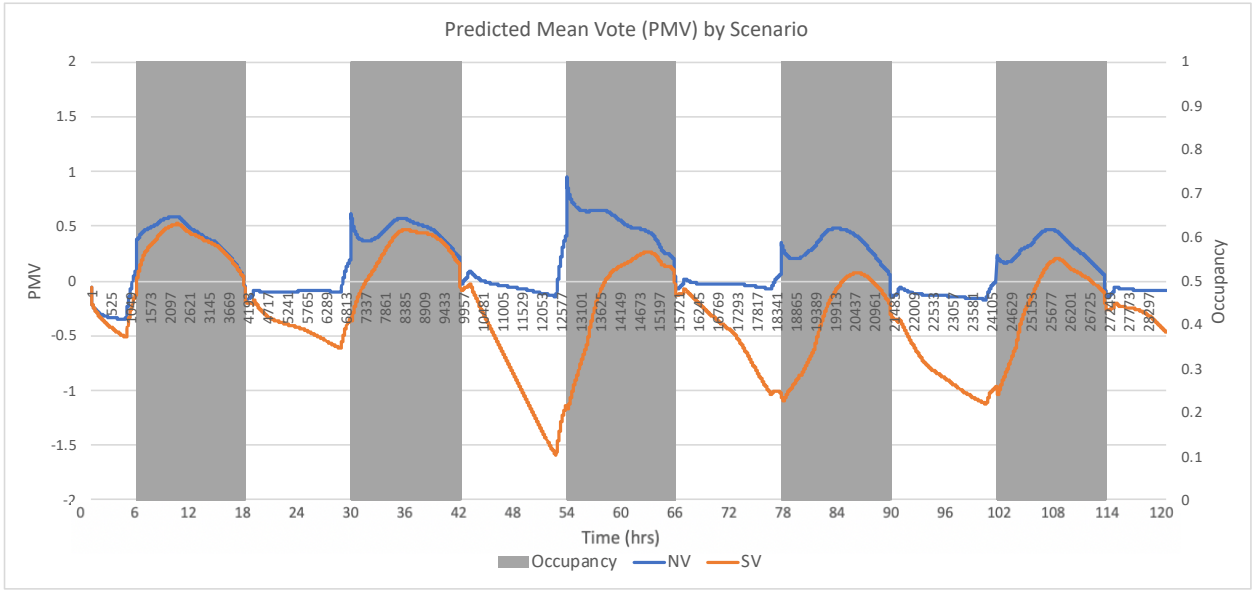

Figure 6.25 *– Instantaneous PMV of Simulated Interior by Scenario*

From Figure 6.25, it is evident that the PMV of the SV scenario is consistently lower than that of the NV scenario, aligning with the cooled surfaces associated with the SV scenario. Although this results in a greater degree of discomfort during low temperatures such as in the early morning and at night, the PMV of the SV scenario results in a greater level of comfort during high temperatures due to the radiative cooling of the surrounding surfaces. The ability to reduce positive PMV votes is a desirable attribute of the SV scenario as occupants experience a greater degree of comfort during a period of reduced energy use compared to the NV scenario. This increased comfort during warm periods comes at the cost of reduced comfort during colder periods, in which occupants experience a cool sensation in both scenarios, but to a greater degree in the SV scenario. This trade-off is considered tolerable as the building does not experience occupancy during the night and the overcooling is overcome by the time the building experiences occupancy, evidenced through PMV > -1 during occupied periods. Furthermore, the cool sensation experienced by occupants in the morning can be addressed by increasing the level of clothing of occupants. Additionally, the duration that occupants are expected to wear increased clothing is small and therefore reasonable. Moreover, the overcooling effects of the SV scenario is desirable over

the NV scenario due to the capability of occupants to augment their clothing insulation level to retain the internal heat produced. This ability to augment comfort is not present in PMV values greater than 0 as environmental conditions would have to change in order to remove excess heat.

Predicted Percent Dissatisfied (PPD)

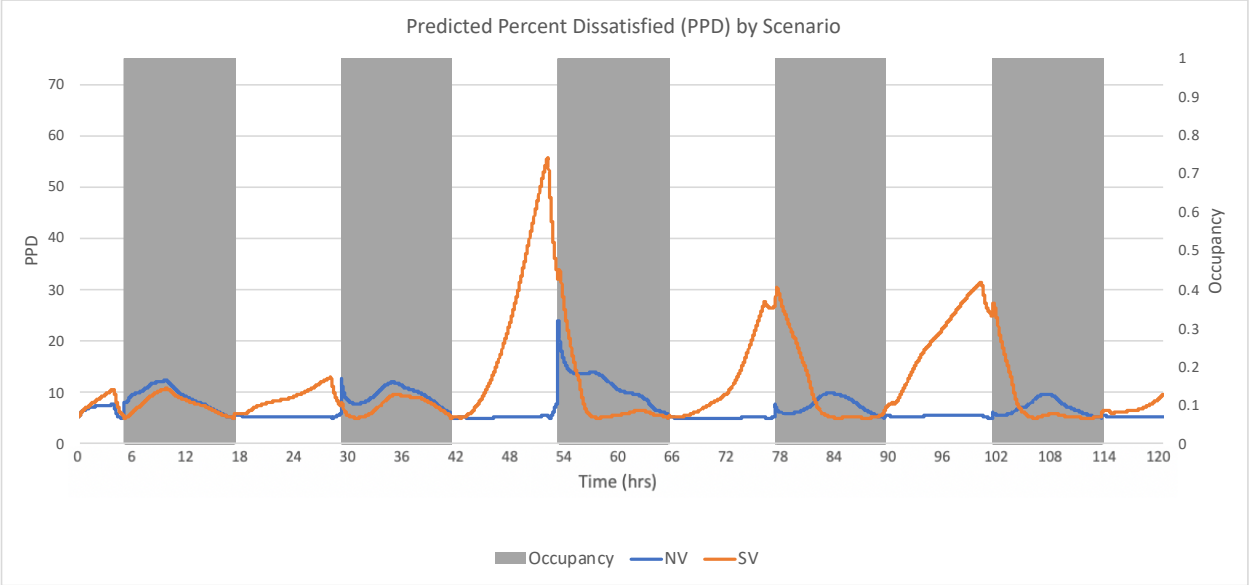

Figure 6.26 *– Instantaneous PPD of Simulated Interior by Scenario*

From the PPD estimates in Figure 6.26, it can be observed that the NV scenario is theoretically more comfortable due to the consistently low estimate compared to the SV scenario. In contrast, the SV scenario experiences a broad range of PPD estimate due to the "overcooled" building thermal mass. Although the SV scenario experiences a PPD as high as greater than 50% during the second night, this value is experienced during an unoccupied period, and therefore will not result in discomfort as there is nobody present to experience discomfort. Upon occupancy, the PPD reduces to about 30%, and continues to reduce to about 15% around 9am, 2 hours after the onset of occupancy. Interestingly, the PPD of the SV scenario continues to reduce to about 5% at around 10am, while at the same time, the PPD of the NV scenario increases to about 15%. This trend of the third day is also observed in the fourth and fifth days. From this, it can be inferred that the NV scenario is typically more comfortable in the first quarter of the day, while the SV scenario is more comfortable during the rest, aligning with the temperature trends of overcooling of the building thermal mass discussed earlier.

6.4: Cooling Load

As discussed in section 5.4, the cooling load was defined as the sum of internal gains, heat flux from interior surfaces, and energy required to meet the required air temperature at the end of the time step to achieve the desired operative temperature. Due to the cooled interior surfaces in the SV scenario, a greater interior air setpoint was allowed due to the comparatively lower mean radiant temperature. This results in a reduced load associated with achieving the temperature differential of the time step, as well as a reduced heat flux to the interior air from surrounding surfaces. The cooling load profiles of the SV and NV scenarios are visualized in Figure 6.27.

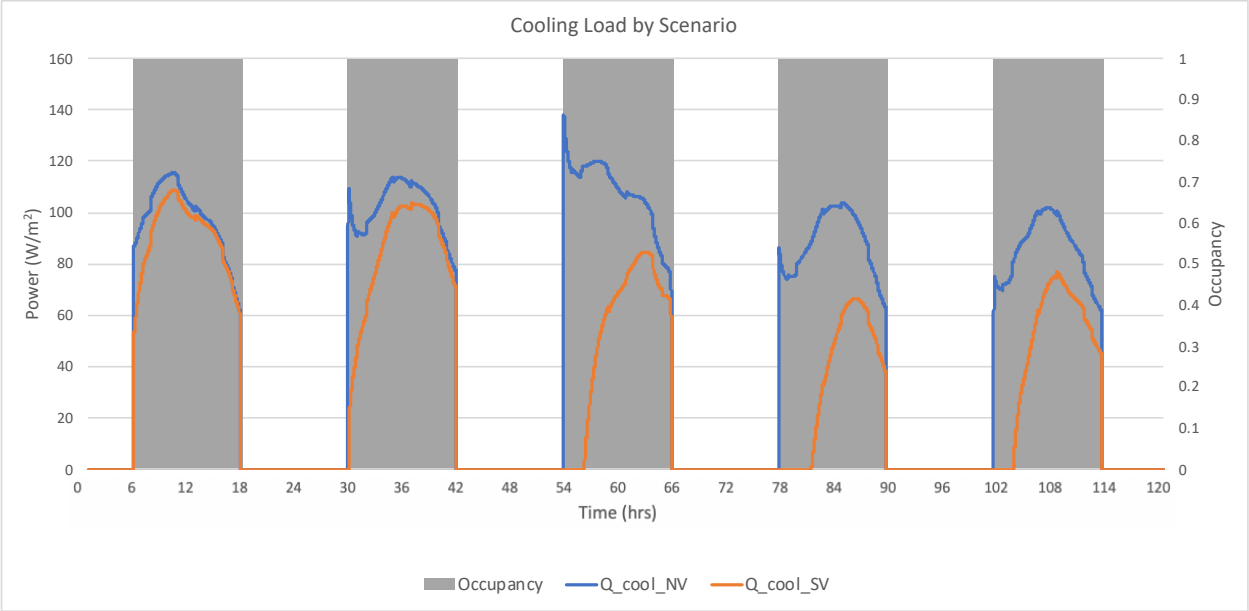

Figure 6.27 – *Cooling Load by Scenario*

In addition to reduced flux and required air temperature change, the radiant temperature is consistently lower in the SV scenario than the NV scenario, allowing the building thermal mass to act as a heat sink for internal gains for a greater period of time and to a greater extent. This is clearly illustrated through the difference in shape of the cooling load profiles.

The NV scenario experiences a spike in the cooling load in the early morning at the onset of occupancy due to the need for the system to reduce the interior air temperature to the required temperature. The cooling load then reduces as the system must only match the gains to the zone as well as the load required to achieve the temperature drop of the time step. The cooling load experiences a local minimum after the initial cooling due to the need for the system to overcome the radiative warming caused by the interior surfaces. Once the interior air cools the interior surfaces, cooling load

increases proportionally to the net power delivered to the space and the required air temperature change. Upon completion of occupancy, the cooling system is shut off and the air as well as assembly node temperatures is allowed to decay naturally

In comparison to the NV scenario, the cooling load profile in the SV scenario exhibits a significantly different trend. Unlike in the NV scenario, the SV scenario does not experience the initial spike in cooling load as the space does not experienced an operative temperature greater than the setpoint temperature. Therefore, the cooling system must only match the load imposed on the system to maintain the desired operative setpoint temperature, rather than having to first achieve the setpoint temperature then maintain it as in the NV scenario. Given that the interior surfaces were cooled at night, the SV scenario doesn't experience the local minimum in cooling load as the NV scenario. In the SV scenario, as the building thermal mass warms due to internal gains, the cooling load increases, but at a much lower rate than in the NV scenario. This is due to the greater weighting of the radiative heat transfer coefficient in the operative temperature definition, resulting in an even greater allowable air temperature than if the convective and radiative heat transfer were equally weighted. As the interior temperatures warm and the mean radiant temperature increases, the required air temperature decreases in proportion to the difference in mean radiant temperature and the ratio of radiative to convective heat transfer. That is to say, during periods of radiative cooling, as the mean radiant temperature increases, the required air temperature decreases at a lower rate. Similarly, during periods of radiative heating, the required air temperature decreases at an increased rate, evidenced by the greater negative slope at the end of day in the SV simulation compared to the NV. The cooling load of the SV scenario increases at a steady rate throughout the day as the building thermal mass warms. The cooling load then reaches a peak value at the end of the day just prior to occupancy reduction, after which the cooling load is reduced for the same reasons as in the NV scenario, and conditioning is terminated once occupancy is concluded. There are two significant phenomena occurring in the comparison of the SV and NV scenarios – the reduction in peak cooling load as well as the shift in start time of the cooling system. The cooling load system start-up is delayed by 2-4 hours and the peak load is reduced by about one third to one quarter in the third, fourth, and fifth days of the SV scenario.

From these trends in the cooling load profiles, it can be deduced that the overcooling of the interior thermal mass has the ability to allow for the thermal mass to act as a heatsink for the duration of occupancy. In order to achieve this, the thermal mass must be precooled to such a temperature that the building thermal mass is acting as a heat sink for the majority, if not for all, of the next day.

7.0: Discussion

7.1: Model Behaviour

From on the above analysis, it can be observed that the consistently low interior surface temperatures in the SV scenario compared to the NV scenario yields a lower mean radiant temperature to the occupant, increasing the required interior air temperature for the desired operative temperature, and thereby reducing the cooling load through reduced heat flux to the interior air from surrounding surfaces, as well as reduced temperature change required for the cooling system to achieve in a given time step. The ventilated slab exhibits high potential for precooling of building thermal mass due to the high heat transfer rate within the slab (high potential for charging); as well as the high thermal mass of the slab (high charge capacity), allowing the system to act as a heat sink for a substantial fraction of the occupied period before the interior thermal mass is fully charged.

Given that exterior air is used as the HTF within the slab hollow core, the exterior temperature boundary imposed on the system has substantial impact on the level of charging of the system. This is evidenced through the minor effects of night ventilation on the cooling load during the first two days of the simulation. From Figure 7.1, it is evident that during the first night, the difference in hollow core surface and exterior air temperature as well as the duration in which this difference occurs is small compared to the difference observed in the second, third, and fourth nights.

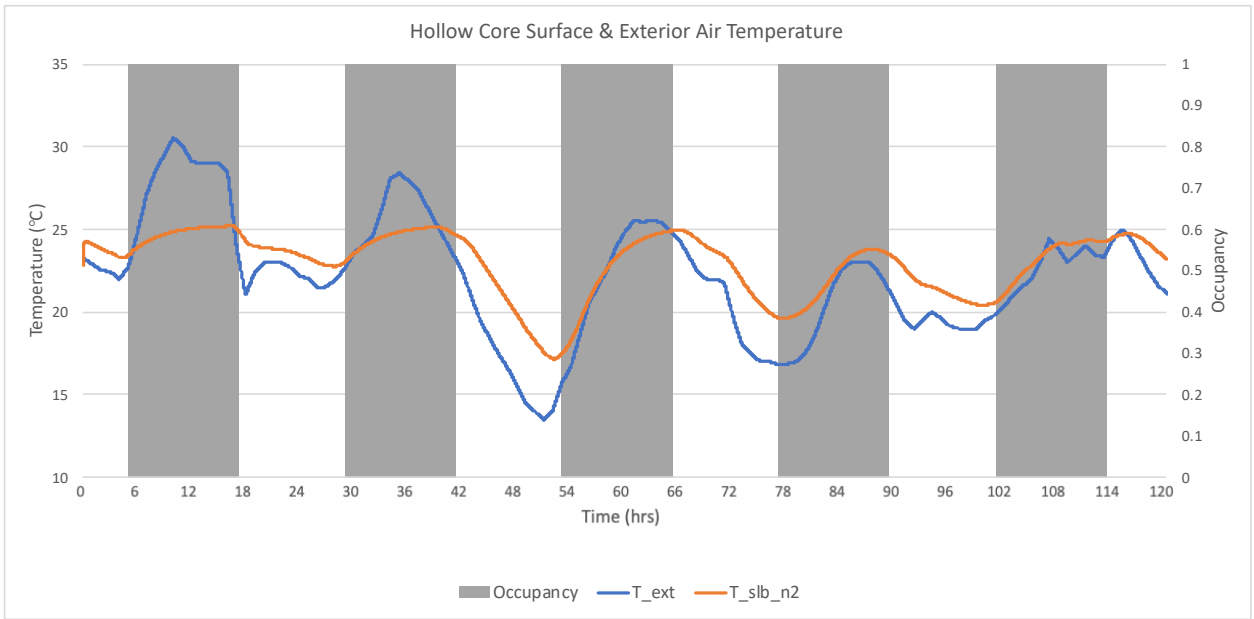

Figure 7.1 *– Hollow Core Surface & Exterior Air Temperatures; Summer Design Week (SV)*

Recalling that the heat flux from the slab to the exterior is proportional to the temperature difference between the HTF (exterior air) and the slab hollow core surface temperature, the potential for thermal mass precooling is represented by the area between the curves when the exterior air is cooler than the slab temperature (ventilation is on), visualized from the origin in Figure 7.2.

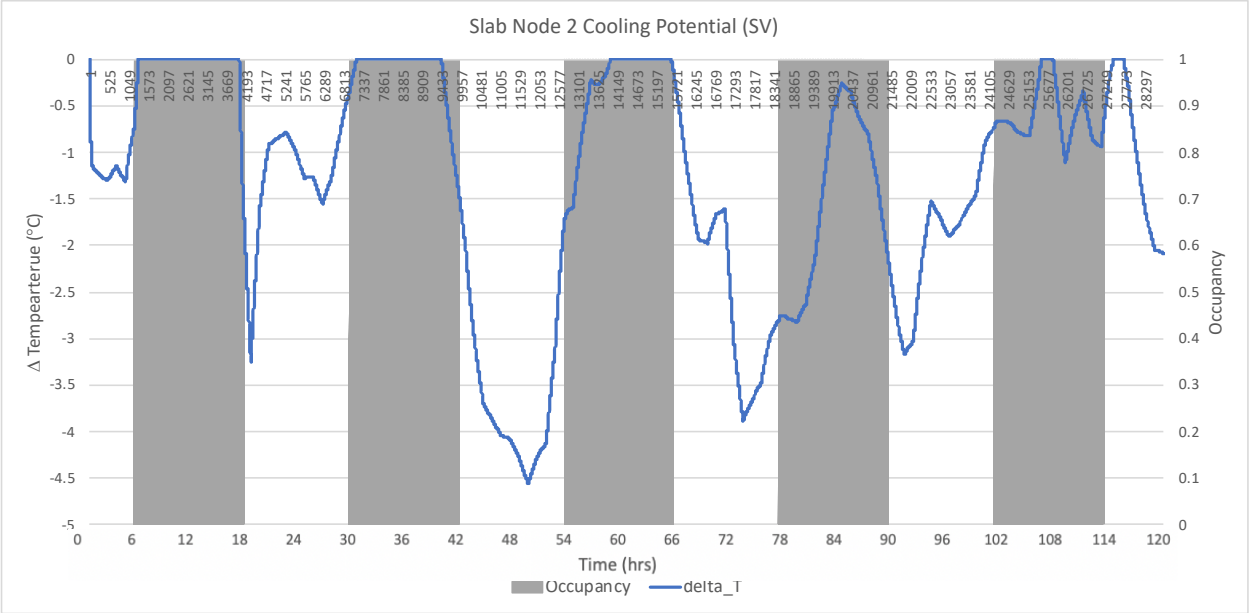

Figure 7.2 *–Temperature Difference of Slab and Exterior Air; Summer Design Week (SV)*

The improved performance of the NV scenario after the first night is a direct result of the increased slab cooling potential realized by the temperature difference increase after the first night, illustrated in Figure 7.2. Comparing the slab cooling potential (Figure 7.2) and cooling load in the SV scenario (Figure 6.27), it is evident that the performance of the SV scenario is a direct product of the cooling potential experienced the previous night. Furthermore, the consistent positive slope in the interior slab node temperature during day illustrated in Figure 6.8 suggests that the slab increases in temperature at a relatively constant rate due to the consistent interior gains. In contrast, the negative slope of the interior slab node temperature is inconsistent due to the dependence of heat transfer rate on temperature difference. From this, it can be concluded that the slab experiences similar total energy delivery during the non-ventilated occupied periods, but energy removal is dependent on the exterior air temperature. This suggests that if the SV slab experiences a total energy removal greater than the typical energy introduction, the slab will experience a temperature lower than of the NV scenario at every time step, while if the slab experiences energy removal less than the typical energy introduced, the slab will experience the maximum temperature of the NV scenario at some time step(s).

7.2: Effect on Occupant Comfort

The occupant comfort assessment discussed above revealed significant deviations from the ideal scenario (PMV & PPD = 0) during the third, fourth, and fifth days due to the overcooling of the slab during the previous nights. The PVM was found to be about -1 (slightly cool) at the onset of occupancy, resulting in a corresponding PPD of 20% – 30% as shown in Figure 7.3.

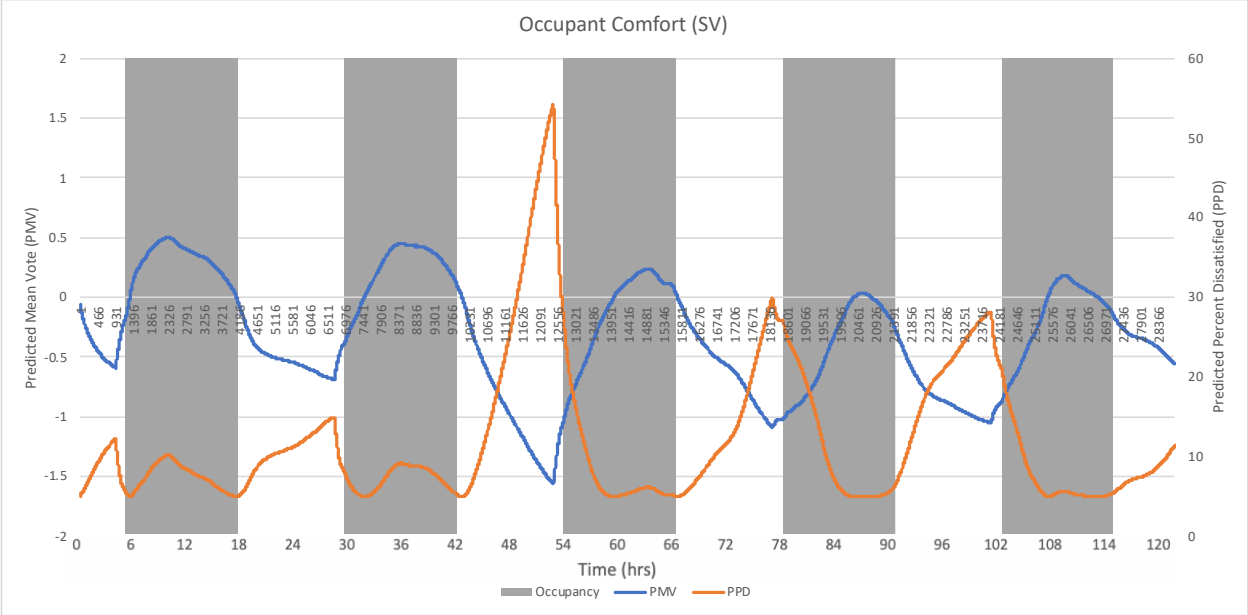

Figure 7.3 *–Occupant Comfort in SV Scenario*

The results of the occupant comfort analysis reveal that night ventilation overcools the building thermal mass significantly in the second, third, and fourth nights. Observing the second night, the PMV and PPD reach about -1.5 and 55% respectively, resulting in a substantial compromise in occupant comfort compared to the NV scenario. However, this global maximum occurs during a presumably unoccupied period, which should result in minimal impact on experienced occupant comfort compared to theoretical. Upon occupancy, the PMV and PPD reduce to about -1.0 and 25% respectively; similar to the local maxima occurring in fourth and fifth days. Compared to the NV scenario, the SV scenario experiences significantly reduced occupant comfort during occupied periods due to the comparatively lower mean radiant temperature. In order to address this, the clothing level of occupants can be increased to retain the internally produced heat of the occupant. Given that the modelled clothing level was 1.0 – representative of typical office wear (long sleeve shirt and pants for male and female), augmentation of clothing level is more appropriate in the SV scenario (addition of clothing) compared to the NV scenario (removal of clothing).

7.3: Cooling Load Reduction

The SV scenario exhibits a reduced cooling load in terms of both magnitude and duration, significantly reducing energy consumption compared to the SV scenario. Outlined in Figure 7.4, the NV scenario consistently consumes less energy than that of the SV scenario, specifically in the third, fourth, and fifth days after precooling initialization has occurred.

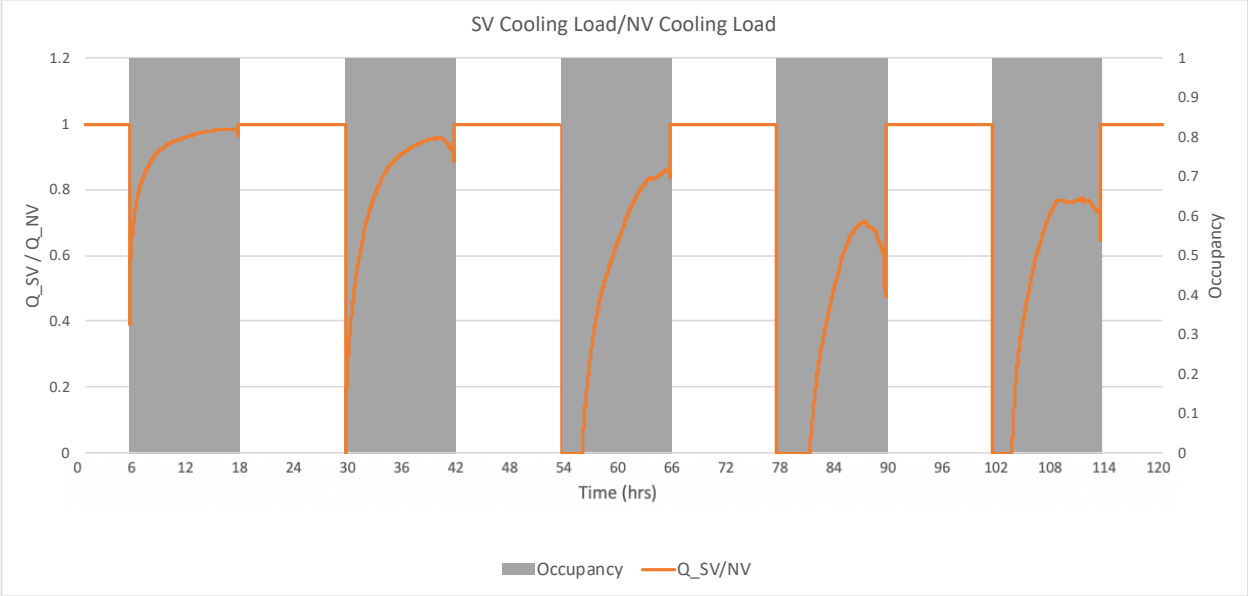

Figure 7.4 *– SV Cooling Load as Fraction of NV Cooling Load*

As discussed earlier, the similar initial temperatures of the system resulted in low cooling load reduction in the first two days due to the need for the system to precool the building thermal mass. Still, the cooling load at the beginning of the first day is substantially lower in the SV scenario than in the NV. The cooling load of the second day is also substantially reduced, shifting the start-up time of the conditioning system forward in time and reducing the peak load experienced by the system. After the cool second night, the third day experiences a dramatic reduction in peak and total cooling load. This reduction is carried over to the fourth day due to the substantial charging of the thermal mass and the cool night temperature's ability to maintain the degree of charging. Figure 7.5 displays total cooling energy consumption over time by scenario, and Figure 7.6 visualizes the SV cooling load as a fraction of the NV cooling load. Figure 7.6 exhibits an interesting trend in that the greatest energy savings occurs at the onset of occupancy during the simulation period (i.e. beginning of first day. The fractional energy consumption then increases to a local maximum at the end of the first day and remains constant at night as no energy is being consumed. In the next days, the fractional total energy consumption

decreases to a local minimum around mid-day, then increases slightly. This behaviour is due to the thermal masses greatest ability to act as a heat sink occurring at the beginning of the day, and reducing (increasing in charge) as the day progresses. The local minimum therefore represents the point in time in which the cooling load ratio is equal to the total energy consumption ratio amongst scenarios. From figure 7.5, it can be seen that the SV scenario results in about 35% energy savings.

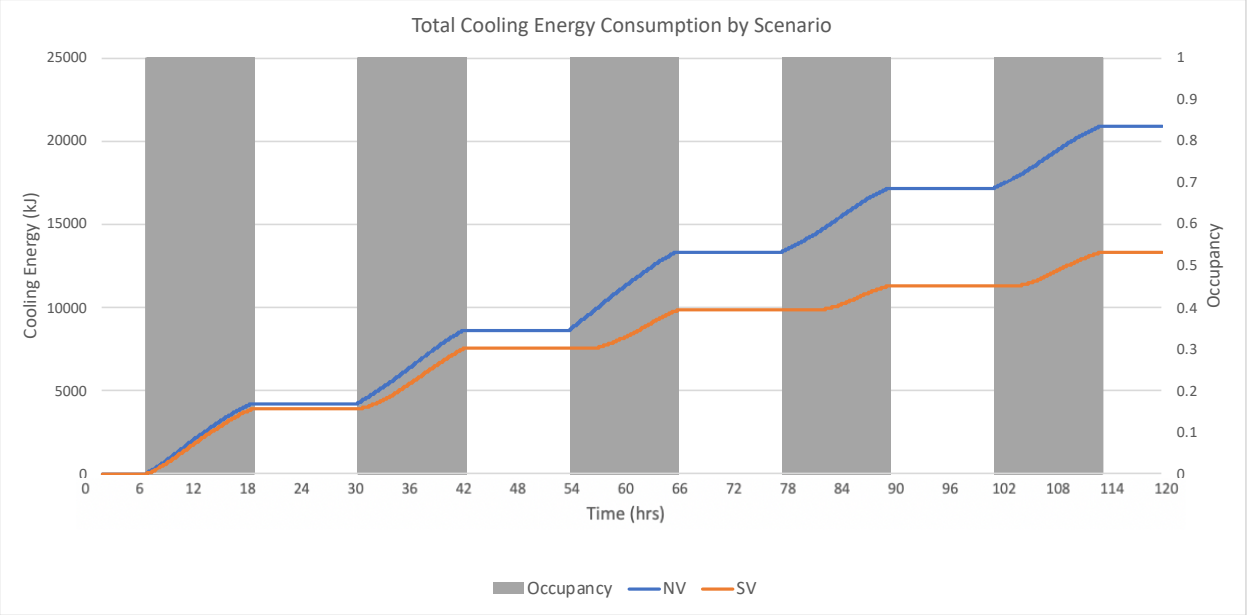

Figure 7.5 *– Total Cooling Energy Consumption by Scenario*

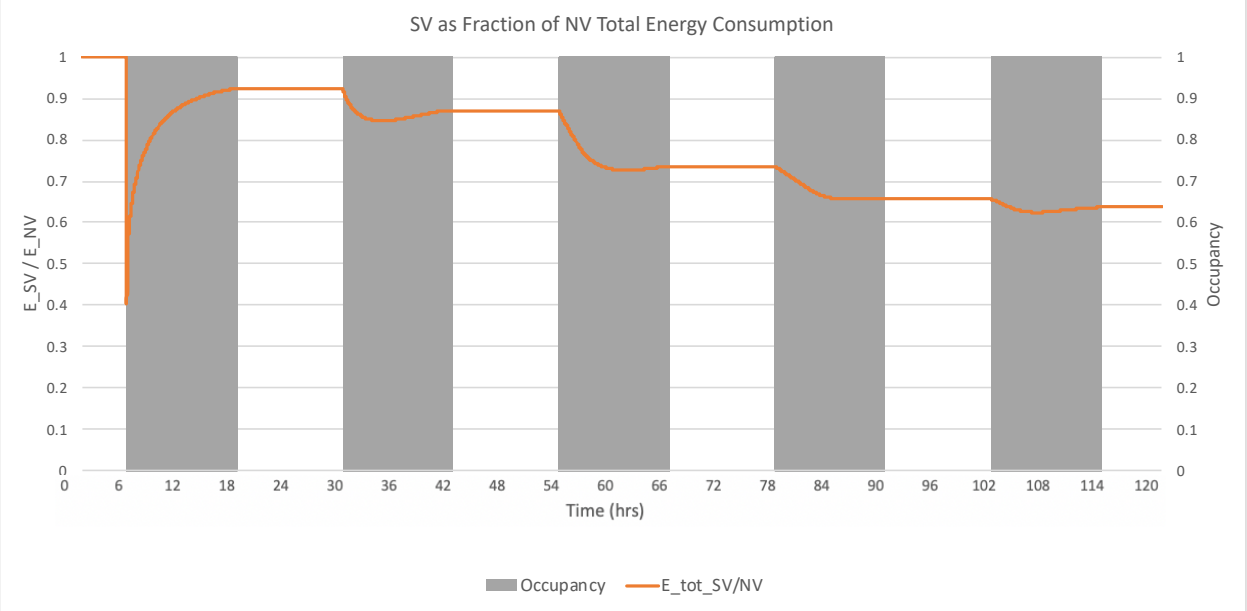

Figure 7.6 *– SV Energy Consumption as Fraction of NV Energy Consumption*

7.4: Limitations of Study

Geometry Discretization and Time Step Definition

The simulated system was broken down by surface (i.e. wall, ceiling, floor), assembly (i.e. opaque wall, window, etc.) and material (i.e. concrete block, glass, etc.) in order to obtain nodes for which the model evaluated the temperature evolution. Recalling the heat equation, heat flux is calculated through a differential thickness, resulting in an infinite quantity of nodes. To simplify this, homogeneous thicknesses in the direction parallel to heat transfer were simplified to a single node. This simplification introduces error in the temperature evolution assessment as it fails to recognize the rate at which heat is introduced to, and conducted through a medium. Furthermore, the definition of the time step was based on the estimate that a temperature change of 0.1C would result in greater than negligible heat flux induced by said temperature change. A finite difference method should be conducted in future research to reduce the error associated with these inputs.

Static Heat Transfer Coefficient

Convective and radiative heat transfer coefficients are temperature dependent, as outlined in equations 13 and 30. However, these coefficients were simplified to a constant value to increase computational efficiency in the simulation. Given that the temperature range explored in this study is narrow and therefore yields minimal change in coefficient values along the domain of the experienced temperature range, the use of static HTCs should result in minimal error. Although the use of a static turbulent forced convection HTC in the hollow core is suspected to over-estimate the precooling potential of the slab due to the reduced HTC at the end of the flow path associated with the temperature increase of the air stream reducing the temperature difference between the air stream and hollow core surface, this error is suspected to be less than the error inherent to the HTC estimation.

Material Interface Thermal Resistance

The interface between materials in assemblies assumed perfect contact between materials, and therefore neglected any thermal resistance introduced at the interface between materials.

Exterior Boundary Condition

The high variability of exterior ambient conditions presented significant uncertainty in this study as the simulation was reliant on exterior conditions to solve for the thermal network at every time step. Although the use of weather data is a common practice, the error inherent to the method is assumed to

be rather large, especially in the SV scenario which relied on direct heat transfer between the exterior air and hollow core slab. It should be noted that the exterior temperatures used were a “best guess” and the results will vary significantly in a system exposed to differing exterior conditions. Similarly, the sky temperature used to determine radiative heat transfer to the exterior surroundings also presents error inherent to the calculation method. Again, this “best guess” boundary does not consider sporadic events such as cloud cover, smog, etc. Furthermore, the radiative boundary condition did not consider the temperature of surrounding buildings due to the uncertainty of location and complexity of view factor determination. This is expected to have significant impact on the radiative exchange between exterior surfaces, however, this should result in minimal impact to the results of the simulation due to the high thermal resistance of the wall and low thermal mass of the window, discusses earlier.

Use of Design Week

The simulated design week was selected in order to consider the worst-case scenario of the cooling season. This design week contained a cool night (second night) followed by a morning with high solar gains (third day) which benefited the simulated system, but might not be representative of typical weather. The SV scenario was able to charge the thermal mass to a high degree during the second night in order to absorb the gains imposed on the system during the morning of the third day, however, this resulted in what could be considered as an exaggerated reduction in cooling load compared to the NV scenario as the NV scenario had to meet the solar load as well as the radiative load caused by the building preheating in the early morning before occupancy; while the SV scenario was discharged (precooled) to such a degree that it was able to absorb all solar gains during the morning without requiring the conditioning system.

Room Geometry Simplification

In a real-world scenario, the simulated office would contain furniture, equipment, occupants, etc. that would have a significant impact on the radiative heat transfer occurring in the zone associated with increased surface quantities (additional view factors), and shading of surrounding surfaces. The effects of these items on inter-zone radiative heat transfer were neglected to simplify the simulation and minimize view factor calculations. Further investigation is required to determine the effects of this assumption on the validity of the model. Although the additional surfaces are suspected to be similar in temperature to the modeled exterior wall surfaces, the additional thermal mass associated with these items is suspected to have an effect on interior conditions (mean radiant and operative temperature).

Fan Power Consumption

The forced convection in the hollow core slab requires fan-induced velocity to achieve the require flow rate. The energy required to produce this flowrate was neglected in this research due to the high variability in the installed condition (single fan per core vs large central fan serving many cores). Although suspected to be low, the fan power consumption will indeed reduce the total energy savings compared to the NV scenario, however, positive energy savings is still expected to be realized.

Lack of Ceiling Finish/Plenum

Due to the high degree of thermal coupling required between the thermal capacitor (slab) and heat source (interior zone) and exterior air (hollow core), an exposed ceiling design was required to ensure maximum heat transfer. Conventionally in office buildings, the space above the drop ceiling conceals duct work as serves as the return air plenum. Therefore, a raised floor set-up is required in the simulated system to maximize thermal coupling between the interior space and slab while also supporting the requirements of the HVAC system.

Risk of Condensation

As shown in Figure 6.8, the interior slab node experiences a minimum temperature of about 18°C in the SV scenario. Given that the dew-point temperature of 23°C at 50% relative humidity is 18°C, condensation could occur on the underside of the slab. To avoid this risk, the hollow core fans should be calibrated such that ventilation is shut off when the interior slab node reaches the minimum desired temperature.

8.0: Conclusions

Building thermal mass presents an opportunity to passively cool interior spaces through the absorption of internal gains while providing a radiative cooling effect due to the reduced temperature increase of the mass. When activated, thermal mass can be further exploited to still absorb solar gains while also providing substantial radiative cooling. In order for the benefits of thermal mass activation to be fully realized, the mass must be sufficiently large such that it can retain its charge for a portion, if not all, of the analyzed period. The mass must also have a high degree of thermal coupling with the heat receptor, and the receptor be of a sufficient size to adequality charge the mass. Furthermore, the charged mass must also be adequately thermally coupled to the objects of interest in order to ensure value is produced from the charging/discharging of the mass.

In the case of a ventilated hollow core slab, the 10m flow path and air velocity of 2m/s resulted in substantial activation of the thermal mass during the charging period. The charging of the slab mass resulted in the charging of surrounding masses due to the convective and radiative coupling with the interior air and surrounding surfaces. This effectively reduced the mean radiant temperature experienced by an occupant seated in the center of the space, allowing for an increased interior ambient air temperature in order to achieve the same operative temperature as in a situation with a greater mean radiant temperature. Based on the operative temperature metric, night ventilation through the hollow core slab was able to reduce the total energy consumption of the system, while also achieving a narrower operating window for the conditioning system and reduced cooling load for the duration of the cooling period.

The simulated cooling load reduction is somewhat underestimated due to the same initial temperatures of nodes used in the SV and NV scenarios, requiring an initialization period for the first two days. The total energy savings is suspected to be higher in a simulation environment of greater duration, or if initialization took place before the start of the simulation. However, this initialization period highlights the need for the building thermal mass to effectively purge heat to the exterior environment every night in order for the capacity of the heatsink to be replenished. Given that the system is reliant on exterior air temperature, the cooling load and energy savings are highly dependent on the exterior boundary that the system is exposed to.

Although the simulation yielded consistently lower cooling loads after initialization, it is not recommended to reduce the size of the conditioning system due to the high possibility of periods of

zero or low thermal mass charging. Cooling load and energy savings described in this research are applicable only to Toronto, ON using the CN2014 weather file. The results of the simulation are suspected to vary significantly through the use of a different climate file and in real life.

The high degree of cooling load and energy reduction in the third day was due to the low night temperatures and high solar gain the subsequent morning. For this reason, the system is suspected to be most effective in climates that experience low night temperatures and high solar gains (i.e. high-altitude locations) or locations that experience a broad temperature range between day and night (i.e. desert/arid locations).

Future work for this research includes refinement of the numerical model to minimize the error associated with the assumptions presented in this research. Refinements include modelling dynamic convective HTCs, finite difference geometry discretization, and analytical distribution of internal gains to interior surfaces, among others. The MRT should also be evaluated at various locations within the floor plan to determine the average experienced MRT based on location, and furniture should also be modelled to determine the effects of increased internal mass and change in view factors on MRT. The fan power of the hollow core ventilation system must also be accurately modelled to determine the impact on conditioning energy savings. In order to do so, the ventilation system must be designed to evaluate the pressure losses (pipe bends, skin friction, etc.) that the ventilation system must overcome in order to provide the desired airstream velocity. Furthermore, a parametric analysis should be conducted on the room geometry to evaluate the effects of varying window to wall ratio, plan aspect ratio, ventilation path length, etc. Additionally, an experimental test chamber should be evaluated to compare the theoretical and actual slab cooling potential as well as the comfort experienced by occupants.

Appendix A

```
%Slab Heat Trasnfer - Constant h-coefficients (Euler Explicit)
%2 Node Slab; 4 Node Walls; Continuous Radiative Exchange
%Naming Convention: Surface#_Node#

%Simulation Parameters
t0 = 0
T0 = 296.15
tFinal = 601500
h = 15
N = ((tFinal-t0)/h)-1;

%Dimensions
l = 20
w = 10
A = l*w

h_o = 1.8
h_t = 1.2

%Surfaces Areas
A1 = w * h_o
A2 = l * h_o
A3 = A1
A4 = A2
A5 = w * h_t
A6 = l * h_t
A7 = A5
A8 = A6
A9 = w * l
A0 = w * l

%Material Thicknesses
L_conc1 = 0.05 %node1
L_conc2 = 0.01 %node2
L_brick = 0.10
L_xps = 0.0792
L_cblock = 0.10
L_gwb = 0.013
L_glass = 0.006
L_wood = 0.01905

%Material Denisities
rho_conc = 2400
rho_brick = 1700
rho_xps = 35
rho_cblock = 1400
rho_gwb = 1000
rho_glass = 2500
rho_wood = 750
rho_air = 1.225
```

```
%Material Volumes
V_air = w * l * (h_o + h_t)

V1_1 = w * h_o * L_gwb
V2_1 = l * h_o * L_gwb
V3_1 = V1_1
V4_1 = V2_1
V5_1 = w * h_t * (L_glass)
V6_1 = l * h_t * (L_glass)
V7_1 = V5_1
V8_1 = V6_1
V9_1 = l * w * L_wood
V0_1 = l * w * L_conc1

V1_2 = w * h_o * L_cblock
V2_2 = l * h_o * L_cblock
V3_2 = V1_2
V4_2 = V2_2
V5_2 = w * h_t * (L_glass)
V6_2 = l * h_t * (L_glass)
V7_2 = V5_2
V8_2 = V6_2
V9_2 = l * w * L_conc1
V0_2 = l * w * L_conc2

V1_3 = w * h_o * L_xps
V2_3 = l * h_o * L_xps
V3_3 = V1_2
V4_3 = V2_2
V9_3 = l * w * L_conc2

V1_4 = w * h_o * L_brick
V2_4 = l * h_o * L_brick
V3_4 = V1_2
V4_4 = V2_2

%Material Specific Heat (J/Kg*K)
cp_conc = 880
cp_brick = 800
cp_xps = 1400
cp_cblock = 1000
cp_gwb = 1000
cp_glass = 670
cp_wood = 1750
cp_air = 1005

%Heat Capacity
Cp_air = cp_air * rho_air * V_air

cp1_1 = cp_gwb * rho_gwb * V1_1
cp2_1 = cp_gwb * rho_gwb * V2_1
cp3_1 = cp1_1
cp4_1 = cp2_1
cp5_1 = cp_glass * rho_glass * V5_1
cp6_1 = cp_glass * rho_glass * V6_1
cp7_1 = cp5_1
cp8_1 = cp6_1
```

```
cp9_1 = cp_wood * rho_wood * V9_1
cp0_1 = cp_conc * rho_conc * V0_1

cp1_2 = cp_cblock * rho_cblock * V1_2
cp2_2 = cp_cblock * rho_cblock * V2_2
cp3_2 = cp1_2
cp4_2 = cp2_2
cp5_2 = cp_glass * rho_glass * V5_2
cp6_2 = cp_glass * rho_glass * V6_2
cp7_2 = cp5_2
cp8_2 = cp6_2
cp9_2 = cp_conc * rho_conc * V9_1
cp0_2 = cp_conc * rho_conc * V0_2

cp1_3 = cp_xps * rho_xps * V1_3
cp2_3 = cp_xps * rho_xps * V2_3
cp3_3 = cp1_2
cp4_3 = cp2_2
cp9_3 = cp_conc * rho_conc * V9_3

cp1_4 = cp_brick * rho_brick * V1_4
cp2_4 = cp_brick * rho_brick * V2_4
cp3_4 = cp1_4
cp4_4 = cp2_4

% PCM Content
x = 0

% Convective Heat Transfer Coefficient
h_Fo  = 13.5 %Forced (in hollow core)
h_cl  = 2.9  %at ceiling
h_Rad = 5.75 %Radiaiton at Ceiling
h_flr = 2.9  %at Floor
h_wl  = 2.5  %at wall (interior)
h_wd  = 1.75
h_ext = 15   %at wall (exterior) - SIMPLIFIED - USE DB VALUES?
h_f   = 2.25 %at occupant

%Thermal Conductance
k_conc = 1.8
k_brick = 0.84
k_xps = 0.034
k_cblock = 0.51
k_gwb = 0.40
k_glass = 0.8
k_wood = 0.16  %H&H

%Thermal Conductivity
C_conc1 = k_conc / L_conc1
C_conc2 = k_conc / L_conc2
C_brick = k_brick / L_brick
C_xps   = k_xps / L_xps
C_cblock = k_cblock / L_cblock
C_gwb = k_gwb / L_gwb
C_glass = k_glass / L_glass
C_wood = k_wood / L_wood
```

```
%Thermal Resistnance
R_Fo  = 1 / h_Fo
R_cl  = 1 / h_cl
R_Rad = 1 / h_Rad
R_flr = 1 / h_flr
R_wl  = 1 / h_wl
R_ext = 1 / h_ext

R_conc1 = 1 / C_conc1
R_conc2 = 1 / C_conc2
R_brick = 1 / C_brick
R_xps = 1 / C_xps
R_cblock = 1 / C_cblock
R_gwb = 1 / C_gwb
R_glass = 1 / C_glass  %Single glass pane (1 node)
R_wood = 1 / C_wood

R_air = 0.4981      %Utotal = 1.978 (DB) kglass = 0.8

%Network Resistance (to Node); Slab, Floor(wood w/ downward flux), Wall,
Window

        %1 denotes interior face (5cm); 2 denotes adj. hollow core
slb_Ri1 = R_cl + (R_conc1)/2
slb_R12 = (R_conc1)/2 + (R_conc2)/2
slb_R2e = (R_conc2)/2 + R_Fo

        %Wood finish
flr_Ri1 = R_flr + (R_wood)/2
flr_R12 = (R_wood)/2 + (R_conc1)/2
flr_R23 = (R_conc1)/2 + (R_conc2)/2
flr_R3e = (R_conc2)/2 + h_Fo

        %1 denotes C_gwb; 2 denotes C_cblock
wl_Ri1 = R_wl + (R_gwb)/2
wl_R12 = (R_gwb)/2 + (R_cblock)/2
wl_R23 = (R_cblock)/2 + (R_xps)/2
wl_R34 = (R_xps)/2 + (R_brick)/2
wl_R4e = (R_brick)/2 + R_ext

        %Window; 2 panes
wd_Ri1 = R_wd + (R_glass)/2
wd_R12 = (R_glass)/2 + R_air
wd_R2e = (R_glass)/2 + R_ext

%Heat Transfer Coefficient
slb_Ui1 = (1/slb_Ri1)
slb_U12 = (1/slb_R12)
slb_U2e = (1/slb_R2e)

flr_Ui1 = (1/flr_Ri1)
flr_U12 = (1/flr_R12)
flr_U23 = (1/flr_R23)
flr_U3e = (1/flr_R3e)
```

```
wl_Ui1 = (1/wl_Ri1)
wl_U12 = (1/wl_R12)
wl_U23 = (1/wl_R23)
wl_U34 = (1/wl_R34)
wl_U4e = (1/wl_R4e)

wd_Ui1 = (1/wd_Ri1)
wd_U12 = (1/wd_R12)
wd_U2e = (1/wd_R2e)

%Forced Conv. (Nonisothermal) Heat Transfer Rate
q = 5333.014148
alpha = exp(-slb_U2e*A/q)
qF = q*(1-alpha)

%Temperature Initialization
    %Structure: T(Surface#)_(Node#)((timestep))
        %Node# increases from indoor to outdoor (i.e. _1 is closest to int)

%Ambient Zone
T_a(1)  = 296.15
T_op_mx = 297.95

%Node 1
T0_1(1) = 298;  %T0_1 represents ceiling interior node (5cm)(1) = T0;
T1_1(1) = 297.5;
T2_1(1) = 297.5;
T3_1(1) = 297.5;
T4_1(1) = 297.5;
T5_1(1) = 297.5;
T6_1(1) = 297.5;
T7_1(1) = 297.5;
T8_1(1) = 297.5;
T9_1(1) = 299;

%Node 2
T0_2(1) = 296;  %T0_2 represents node adj. hollow core (1cm)(1) = T0;
T1_2(1) = 297.5;
T2_2(1) = 297.5;
T3_2(1) = 297.5;
T4_2(1) = 297.5;
T5_2(1) = 296;
T6_2(1) = 296;
T7_2(1) = 296;
T8_2(1) = 296;

%Node 3
T1_3(1) = 301;
T2_3(1) = 301;
T3_3(1) = 300;
T4_3(1) = 300;

%Node 4
T1_4(1) = 305;
T2_4(1) = 305;
T3_4(1) = 303;
T4_4(1) = 308;
```

```
%Surface - Occupant View Factors (North or South Facing)
Fv_occ_1 =  [ 0.318285733  0           0           0           0           0
0           0           0           0 ;
            0            0.070094314 0           0           0           0
0           0           0           0 ;
            0            0           0.016376706 0           0           0
0           0           0           0 ;
            0            0           0           0.075398869 0           0
0           0           0           0 ;
            0            0           0           0           0.016376706 0
0           0           0           0 ;
            0            0           0           0           0
0.023163958 0           0           0           0 ;
            0            0           0           0           0           0
0.007663723 0           0           0 ;
            0            0           0           0           0           0
0           0.030705842 0           0 ;
            0            0           0           0           0           0
0           0           0.007663723 0 ;
            0            0           0           0           0           0
0           0           0           0.434270428 ]

Fv_occ =  [ 0.070094314 ;
            0.016376706 ;
            0.075398869 ;
            0.016376706 ;
            0.023163958 ;
            0.007663723 ;
            0.030705842 ;
            0.007663723 ;
            0.434270428 ;
            0.318285733  ]

Fv_occ_t = Fv_occ.'

%Surface - Surface View Factors
Fv = [ 0        0.089   0.0132  0.089   0       0.0366  0.0087  0.0366
0.4044  0.3224 ;
       0.0445   0       0.0445  0.0629  0.0183  0       0.0183  0.0405
0.4241  0.3469 ;
       0.0132   0.089   0       0.089   0.0087  0.0366  0       0.0366
0.4044  0.3224 ;
       0.0445   0.0629  0.0445  0       0.0183  0.0405  0.0183  0
0.4241  0.3469 ;
       0        0.0549  0.0131  0.0549  0       0.067   0.0084  0.067
0.3056  0.4285 ;
       0.0275   0       0.0275  0.0608  0.0335  0       0.0335  0.0421
0.3297  0.4454 ;
       0.0131   0.0549  0       0.0549  0.0088  0.067   0       0.067
0.3056  0.4285 ;
       0.0275   0.0608  0.0275  0       0.0335  0.0421  0.0335  0
0.3297  0.4454 ;
       0.0364   0.0763  0.0364  0.0763  0.0183  0.0396  0.0183  0.0396  0
0.6587 ;
       0.029    0.0625  0.029   0.0625  0.0257  0.0535  0.0257  0.0535
0.6587  0 ]
```

```
%Surface Emmisivities
eps = [ 0.90    0       0       0       0       0       0       0       0
0 ;
        0       0.90    0       0       0       0       0       0       0
0 ;
        0       0       0.90    0       0       0       0       0       0
0 ;
        0       0       0       0.90    0       0       0       0       0
0 ;
        0       0       0       0       0.90    0       0       0       0
0 ;
        0       0       0       0       0       0.90    0       0       0
0 ;
        0       0       0       0       0       0       0.90    0       0
0 ;
        0       0       0       0       0       0       0       0.90    0
0 ;
        0       0       0       0       0       0       0       0       0.90
0 ;
        0       0       0       0       0       0       0       0       0
0.90 ]

%Surface Areas
S = [   18      0       0       0       0       0       0       0       0
0 ;
        0       36      0       0       0       0       0       0       0
0 ;
        0       0       18      0       0       0       0       0       0
0 ;
        0       0       0       36      0       0       0       0       0
0 ;
        0       0       0       0       12      0       0       0       0
0 ;
        0       0       0       0       0       24      0       0       0
0 ;
        0       0       0       0       0       0       12      0       0
0 ;
        0       0       0       0       0       0       0       24      0
0 ;
        0       0       0       0       0       0       0       0       200
0 ;
        0       0       0       0       0       0       0       0       0
200 ]

I = eye(10,10)

sig = 5.67 * 10^(-8)


for i = 1:40080

%Specific Heat Condition
cpi = 2112000.*(1-x) + 11083333.33.*x
cpo = 2112000.*(1-x)
```

```
    if T0_1(i) > 297.15
            cp(i) = cpo
        elseif T0_1(i) < 294.15
            cp(i) = cpo
        else
            cp(i) = cpi
    end

    if T0_2(i) > 297.15
            cp(i) = cpo
        elseif T0_2(i) < 294.15
            cp(i) = cpo
        else
            cp(i) = cpi
    end

%Slab Heat Capacity
cp0_1(i) = cp(i).*(l*w*0.05)
cp0_2(i) = cp(i).*(l*w*0.01)

%Ventilation Condition
    if Te(i) < T0_2(i)
           slb_U2e_NITF(i) = qF;
        else
           slb_U2e_NITF(i) = 0;
    end

%Node 1 Temperature Array
Tj_1(:,i)  = [ T1_1(i) ; T2_1(i) ; T3_1(i) ; T4_1(i) ; T5_1(i) ; T6_1(i) ;
T7_1(i) ; T8_1(i) ; T9_1(i) ; T0_1(i) ]
Tj_1_exp(:,i) = Tj_1(:,i).^4

%Radiosity
J(:,i) = (I-(I-eps) * Fv) \(5.67 * 10^(-8) * eps * ( (Tj_1(:,i)).^(4) ) )

%Radiant Heat Transfer (W)
Phi_Rad = S * (Fv - I) * J

%Mean Radiant Temperature
T_mrt(i) = ( Fv_occ_t * Tj_1_exp(:,i) ) ^ (1/4)

%Operative Temperature
T_op(i) = (T_a(i) * h_f + T_mrt(i) * h_Rad) / (h_f + h_Rad)

%Gains(W) to Zone
G_a(i) = ( G_occ(i) + 0.8 * G_equip(i) + 0.58 * G_light(i) ) * A

%Convetive Heat Transfer(W) to zone
Q_a_wl(i)  = ( T1_1(i) + T2_1(i) + T3_1(i) + T4_1(i) - 4 * T_a(i) ) * h_wl *
( A1 + A2 + A3 + A4 )
Q_a_wd(i)  = ( T5_1(i) + T6_1(i) + T7_1(i) + T8_1(i) - 4 * T_a(i) ) * h_wd *
( A5 + A6 + A7 + A8 )
Q_a_flr(i) = ( T9_1(i) - T_a(i) ) * h_flr * A9
Q_a_cl(i)  = ( T0_1(i) - T_a(i) ) * h_cl  * A0
```

```
%External Power(W) to Zone
Q_a(i) = Q_a_wl(i) + Q_a_wd(i) + Q_a_flr(i) + Q_a_cl(i) + G_a(i)

%Ambient Air
T_a(i)    = ( T_op(i) * (h_f + h_Rad) - T_mrt(i) * h_Rad ) / h_f
T_a_pr(i) = ( T_op_mx * (h_f + h_Rad) - T_mrt(i) * h_Rad ) / h_f
    if G_occ(i) > 0 && T_op(i) > (T_op_mx - 0.01)
            dT_a(i) = T_a_pr(i) - T_a(i)
        else
            dT_a(i) = Q_a(i) * h / Cp_air
    end
T_a(i+1) = T_a(i) + dT_a(i)

%Cooling Load
    if G_occ(i) > 0 && T_op(i) > (T_op_mx - 0.01)
            Q_cool(i) = Q_a(i) + ( -dT_a(i) * Cp_air / ( h * A ) )
        else
            Q_cool(i) = 0
    end

%Post Cooled T_op
T_op_pr(i) = (T_a(i+1) * h_f + T_mrt(i) * h_Rad) / (h_f + h_Rad)

%Temperature Evolution (Euler)
    dT1_1(i) = 1/cp1_1 * ( -wl_Ui1 * (T1_1(i)-T_a(i)) * (w*h_o)  - ( (-wl_U12
* (T1_2(i)-T1_1(i))) * (w*h_o) ) + Phi_Rad(1,i) + ( (18/580) * (
G_equip(i)*0.2 + G_light(i)*0.42) * A ) );
    dT2_1(i) = 1/cp2_1 * ( -wl_Ui1 * (T2_1(i)-T_a(i)) * (l*h_o)  - ( (-wl_U12
* (T2_2(i)-T2_1(i))) * (l*h_o) ) + Phi_Rad(2,i) + ( (36/580) * (
G_equip(i)*0.2 + G_light(i)*0.42) * A ) );
    dT3_1(i) = 1/cp3_1 * ( -wl_Ui1 * (T3_1(i)-T_a(i)) * (w*h_o)  - ( (-wl_U12
* (T3_2(i)-T3_1(i))) * (w*h_o) ) + Phi_Rad(3,i) + ( (18/580) * (
G_equip(i)*0.2 + G_light(i)*0.42) * A ) );
    dT4_1(i) = 1/cp4_1 * ( -wl_Ui1 * (T4_1(i)-T_a(i)) * (l*h_o)  - ( (-wl_U12
* (T4_2(i)-T4_1(i))) * (l*h_o) ) + Phi_Rad(4,i) + ( (36/580) * (
G_equip(i)*0.2 + G_light(i)*0.42) * A ) );
    dT5_1(i) = 1/cp5_1 * ( -wd_Ui1 * (T5_1(i)-T_a(i)) * (w*h_t)  - ( (-wd_U12
* (T5_2(i)-T5_1(i))) * (w*h_t) ) + Phi_Rad(5,i) + ( (12/580) * (
G_equip(i)*0.2 + G_light(i)*0.42) * A ) );
    dT6_1(i) = 1/cp6_1 * ( -wd_Ui1 * (T6_1(i)-T_a(i)) * (l*h_t)  - ( (-wd_U12
* (T6_2(i)-T6_1(i))) * (l*h_t) ) + Phi_Rad(6,i) + ( (24/580) * (
G_equip(i)*0.2 + G_light(i)*0.42) * A ) );
    dT7_1(i) = 1/cp7_1 * ( -wd_Ui1 * (T7_1(i)-T_a(i)) * (w*h_t)  - ( (-wd_U12
* (T7_2(i)-T7_1(i))) * (w*h_t) ) + Phi_Rad(7,i) + ( (12/580) * (
G_equip(i)*0.2 + G_light(i)*0.42) * A ) );
    dT8_1(i) = 1/cp8_1 * ( -wd_Ui1 * (T8_1(i)-T_a(i)) * (l*h_t)  - ( (-wd_U12
* (T8_2(i)-T8_1(i))) * (l*h_t) ) + Phi_Rad(8,i) + ( (24/580) * (
G_equip(i)*0.2 + G_light(i)*0.42) * A ) );
    dT9_1(i) = 1/cp9_1 * (-flr_Ui1 * (T9_1(i)-T_a(i)) * (l*w) + Phi_Rad(9,i)
+ A * ( (200/580) * ( G_equip(i)*0.2 + G_light(i)*0.42 ) ) + A * G_sol(i) );
    dT0_1(i) = 1/cp0_1(i) * (-slb_Ui1 * (T0_1(i)-T_a(i)) * (l*w)    - ((-
slb_U12 * (T0_2(i)-T0_1(i))) * (l*w)   ) + Phi_Rad(10,i) +( (200/580) * (
G_equip(i)*0.2 + G_light(i)*0.42) * A ) );
```

```
    dT1_2(i) = 1/cp1_2 * ( -wl_U12 * (T1_2(i)-T1_1(i)) * (w*h_o)  - ( (-
wl_U23 * (T1_3(i)-T1_2(i))) * (w*h_o) ) );
    dT2_2(i) = 1/cp2_2 * ( -wl_U12 * (T2_2(i)-T2_1(i)) * (l*h_o)  - ( (-
wl_U23 * (T2_3(i)-T2_2(i))) * (l*h_o) ) );
    dT3_2(i) = 1/cp3_2 * ( -wl_U12 * (T3_2(i)-T3_1(i)) * (w*h_o)  - ( (-
wl_U23 * (T3_3(i)-T3_2(i))) * (w*h_o) ) );
    dT4_2(i) = 1/cp4_2 * ( -wl_U12 * (T4_2(i)-T4_1(i)) * (l*h_o)  - ( (-
wl_U23 * (T4_3(i)-T4_2(i))) * (l*h_o) ) );
    dT5_2(i) = 1/cp5_2 * ( -wd_U12 * (T5_2(i)-T5_1(i)) * (w*h_t)  - ( (-
wd_U2e * (Te(i)-T5_2(i)))   * (w*h_t) ) + ( 0.05 * w*h_o * Sol_S(i) ) - ( -
0.05 * sig * ( (Te(i)^(4)) - (T5_2(i)^4) )) );
    dT6_2(i) = 1/cp6_2 * ( -wd_U12 * (T6_2(i)-T6_1(i)) * (l*h_t)  - ( (-
wd_U2e * (Te(i)-T6_2(i)))   * (l*h_t) ) + ( 0.05 * w*h_o * Sol_W(i) ) - ( -
0.05 * sig * ( (Te(i)^(4)) - (T6_2(i)^4) )) );
    dT7_2(i) = 1/cp7_2 * ( -wd_U12 * (T7_2(i)-T7_1(i)) * (w*h_t)  - ( (-
wd_U2e * (Te(i)-T7_2(i)))   * (w*h_t) ) + ( 0.05 * w*h_o * Sol_N(i) ) - ( -
0.05 * sig * ( (Te(i)^(4)) - (T7_2(i)^4) )) );
    dT8_2(i) = 1/cp8_2 * ( -wd_U12 * (T8_2(i)-T8_1(i)) * (l*h_t)  - ( (-
wd_U2e * (Te(i)-T8_2(i)))   * (l*h_t) ) + ( 0.05 * w*h_o * Sol_E(i) ) - ( -
0.05 * sig * ( (Te(i)^(4)) - (T8_2(i)^4) )) );
    dT0_2(i) = 1/cp0_2(i) * (-slb_U12 * (T0_2(i)-T0_1(i)) * (l*w)    - ((-
slb_U2e_NITF(i) * (Te(i)-T0_2(i)))   ) );

    dT1_3(i) = 1/cp1_3 * ( -wl_U23 * (T1_3(i)-T1_2(i)) * (w*h_o)  - ( (-
wl_U34 * (T1_4(i)-T1_3(i))) * (w*h_o) ) );
    dT2_3(i) = 1/cp2_3 * ( -wl_U23 * (T2_3(i)-T2_2(i)) * (l*h_o)  - ( (-
wl_U34 * (T2_4(i)-T2_3(i))) * (l*h_o) ) );
    dT3_3(i) = 1/cp3_3 * ( -wl_U23 * (T3_3(i)-T3_2(i)) * (w*h_o)  - ( (-
wl_U34 * (T3_4(i)-T3_3(i))) * (w*h_o) ) );
    dT4_3(i) = 1/cp4_3 * ( -wl_U23 * (T4_3(i)-T4_2(i)) * (l*h_o)  - ( (-
wl_U34 * (T4_4(i)-T4_3(i))) * (l*h_o) ) );

    dT1_4(i) = 1/cp1_4 * ( -wl_U34 * (T1_4(i)-T1_3(i)) * (w*h_o)  - ( (-
wl_U4e * (Te(i)-T1_4(i))) * (w*h_o) ) + 0.9 * w*h_o * Sol_S(i) - ( -0.9 * sig
* ( (Te(i)^(4)) - (T1_4(i)^4) )) );
    dT2_4(i) = 1/cp2_4 * ( -wl_U34 * (T2_4(i)-T2_3(i)) * (l*h_o)  - ( (-
wl_U4e * (Te(i)-T2_4(i))) * (l*h_o) ) + 0.9 * l*h_o * Sol_W(i) - ( -0.9 * sig
* ( (Te(i)^(4)) - (T2_4(i)^4) )) );
    dT3_4(i) = 1/cp3_4 * ( -wl_U34 * (T3_4(i)-T3_3(i)) * (w*h_o)  - ( (-
wl_U4e * (Te(i)-T3_4(i))) * (w*h_o) ) + 0.9 * w*h_o * Sol_N(i) - ( -0.9 * sig
* ( (Te(i)^(4)) - (T3_4(i)^4) )) );
    dT4_4(i) = 1/cp4_4 * ( -wl_U34 * (T4_4(i)-T4_3(i)) * (l*h_o)  - ( (-
wl_U4e * (Te(i)-T4_4(i))) * (l*h_o) ) + 0.9 * l*h_o * Sol_E(i) - ( -0.9 * sig
* ( (Te(i)^(4)) - (T4_4(i)^4) )) );

    T1_1(i+1) = T1_1(i) + h*dT1_1(i);
    T2_1(i+1) = T2_1(i) + h*dT2_1(i);
    T3_1(i+1) = T3_1(i) + h*dT3_1(i);
    T4_1(i+1) = T4_1(i) + h*dT4_1(i);
    T5_1(i+1) = T5_1(i) + h*dT5_1(i);
    T6_1(i+1) = T6_1(i) + h*dT6_1(i);
    T7_1(i+1) = T7_1(i) + h*dT7_1(i);
    T8_1(i+1) = T8_1(i) + h*dT8_1(i);
    T9_1(i+1) = T9_1(i) + h*dT9_1(i);
    T0_1(i+1) = T0_1(i) + h*dT0_1(i);
```

```
    T1_2(i+1) = T1_2(i) + h*dT1_2(i);
    T2_2(i+1) = T2_2(i) + h*dT2_2(i);
    T3_2(i+1) = T3_2(i) + h*dT3_2(i);
    T4_2(i+1) = T4_2(i) + h*dT4_2(i);
    T5_2(i+1) = T5_2(i) + h*dT5_2(i);
    T6_2(i+1) = T6_2(i) + h*dT6_2(i);
    T7_2(i+1) = T7_2(i) + h*dT7_2(i);
    T8_2(i+1) = T8_2(i) + h*dT8_2(i);
    T0_2(i+1) = T0_2(i) + h*dT0_2(i);

    T1_3(i+1) = T1_3(i) + h*dT1_3(i);
    T2_3(i+1) = T2_3(i) + h*dT2_3(i);
    T3_3(i+1) = T3_3(i) + h*dT3_3(i);
    T4_3(i+1) = T4_3(i) + h*dT4_3(i);

    T1_4(i+1) = T1_4(i) + h*dT1_4(i);
    T2_4(i+1) = T2_4(i) + h*dT2_4(i);
    T3_4(i+1) = T3_4(i) + h*dT3_4(i);
    T4_4(i+1) = T4_4(i) + h*dT4_4(i);

end
```

Appendix B

```
%PMV Calulator
vel = 0.5
RH  = 50
clo = 1
met = 1.0

A_Du = 2.06
PA = 1.013
ICL = 0.155 * clo
M_Du = met * 50 %M/A_Du
nu = 0 %mechanical efficiency

    if ICL < 0.078
        FCL = 1 + 1.29 * ICL
    else
        FCL = 1.05 + 0.645 * ICL
    end

for i = 1:28801

TA(i) = (T_a(i) - 273)
TR(i) = (T_mrt(i) - 273)

TAA(i) = TA(i) + 273
TRA(i) = TR(i) + 273
TCLA(i) = TAA(i) + (35.5 - TA(i)) ./ (3.5 * (6.45 * ICL + 0.1) )

EPS = 0.0015

TCL(i) = TCLA(i) - 273

%Internal Heat Production
H = M_Du * (1-nu)

%Skin Diffusion Loss
HL1(i) = 0.35 * (43 - 0.061 * M_Du * (1 - nu) - PA)
%Sweat Loss
    if M_Du > 50
        HL2 = 0.42 * (M_Du * (1 - nu) - 58.15)
    else
        HL2 = 0
    end

%Latent Respiration Loss
HL3(i) = 0.0023 * M_Du * (44 - PA)

%Sensible Respiraiton Loss
HL4(i) = 0.0014 * M_Du * (34 - TA(i))

%Radiaion Loss
HL5(i) = 3.4 * 10^(-8) * FCL * ((TCLA(i).^4 - TRA(i).^4))
```

```
%Convection Loss
    if ( 2.05 * ( TCL(i)-TA(i) ).^0.25 ) > ( 10.4 * vel^(1/2) )
        hc = ( 2.05 * (TCL-TA)^0.25 )
    else
        hc = 10.4 * (vel^(1/2))
    end
HL6 = FCL * hc * (TCL - TA)

%Thermal Seneation Skin Transfer Coefficient
TS = 0.352 * exp(-0.042 * M_Du) + 0.032

    if vel < 0.2
        TPO(i) = 0.5 .* TA(i) + 0.5 .* TR(i)
    else
        if vel < 0.6
            TPO(i) = 0.6 .* TA(i) + 0.4 .* TR(i)
        else
            TPO(i) = 0.7 .* TA(i) + 0.3 .* TR(i)
        end
    end

PMV(i) = TS * (H - HL1(i) - HL2 - HL3(i) - HL4(i) - HL5(i) - HL6(i))
PPD(i) = 100 - 95 * exp(-0.03353 * (PMV(i))^4 - 0.2179 * (PMV(i))^2)

end
```

Works Cited

Ahmed Faheem, G. R. (2016). A numerical study on the thermal performance of night ventilated hollow core slabs cast with micro-encapsulated PCM concrete. *Energy and Buildings*(127), 892-906.

Andresen, I., & Brandemuehl, M. J. (1992). Heat Storage in Building Thermal Mass: A Parametric Study. *ASHRAE Transactions.* ASHRAE.

ASHRAE. (2017). *ASHRAE Fundamentals .* Atlanta: W Stephen Comstock.

Barton, P., & Beggs, C. B. (2002). A theoretical study of the thermal performance of the ThermoDeck hollow core slab system. *Applied Thermal Engineering*, 1485-1499.

Barzin, R., Chen, J. J., Young, B. R., & Farid, M. M. (2015). Application of PCM energy storage in combination with night ventilation for space cooling. *Applied Energy*, 412-421.

Braun, J. E. (1990). Reducing Energy Costs and Peak Electrical Demand Through Optimal Control of Building Thermal Storage. *ASHRAE Transactions*, 876-887.

Braun, J. E. (2003). Load Control Using Building Thermal Mass. *ASME Journal of Solar Engineering*, 292-301.

Braun, J. E., & Kyoung-Ho, L. (2006). Assessment of demand limiting using building thermal mass in small commercial buildings. *ASHRAE Transactions*, 547-558.

Braun, J. E., Lawrence, T. M., Klaassen, C. J., & House, J. M. (2002). Demonstration of Load Shifting and Peak Load Reduction with Control of Building Thermal Mass. *Teaming for Efficiency.* Pacific Grove, CA: ACEEE.

Braun, J. E., Montgomery, K., & Chaturvedi, N. (2001). Evaluating the Performance of Building Thermal Mass Control Strategies. *International Journal of Heating, Ventilation, Air-Conditioning and Refrigeration Research*, 403-428.

Cannistraro, G., Franzitta, G., & Giaconia, C. (1992). Algorithms for the calculation of the view factors between human body and rectangular surfaces in parallelepiped environments. *Energy and Buildings*, 51-60.

Cengel, Y., & Ghajar, A. (2015). *Heat and Mass Transfer.* New York: McGraw-Hill Education .

David, D., Kuznik, F., Johannes, K., & Obrecht, C. (n.d.). *Selection of TES for real boundary conditions in building.* INSA.

Drake, J. (1987). *A study of the optimal transition temperature of PCM wallboard for solar energy storage.* Oak Ridge, TN: US Department of Energy.

Eames, E. (2016, August 14). *Intro to Phases and Intermolecular Forces.* Retrieved from LibreTexts - Chemistry: https://chem.libretexts.org/Bookshelves/General_Chemistry/Book%3A_General_Chemistry_Supplement_(Eames)/Phases_and_Intermolecular_Forces/Intro_to_Phases_and_Intermolecular_Forces

EngineeringToolBox. (2003). *Air - Dynamic and Kinematic Viscosity*. Retrieved from The Engineering Tool Box: https://www.engineeringtoolbox.com/air-absolute-kinematic-viscosity-d_601.html

Fanger, P. O. (1972). *Thermal Comfort: Analysis and Applications in Environmental Engineering .* New York: McGraw-Hill.

Hutcheon, N. B., & Handegord, G. O. (1995). *Building Science for a Cold Climate.* Ottawa: John Wiley & Sons.

Keeney, K. R., & Braun, J. E. (1997). Applicaiton of Building Precooling to Reduce Peak Cooling Requirements. *ASHRAE Transactions*, 463-469.

Kissock, J. K., & Limas, S. (2006). Diurnal load reduction through phase change building components. *ASHRAE Transactions*, 509-517.

Kuznik, F., David, D., Johannes, K., & Roux, J. (2011). A review on phase change materials integrated in building walls. *Renewable and Sustainable Energy*, 379-391.

Lauzier, N. (2005). *Math Works File Exchange*. Retrieved from View Factors with GUI: https://www.mathworks.com/matlabcentral/fileexchange/5683-view-factors-with-gui

Lee, K. H., & Braun, J. E. (2004). Development and application of an inverse building model for demand response in small commercial buildings. *SimBuild.* Boulder, CO: IBPSA.

Lee, K. H., & Braun, J. E. (2006). An Experimental Evaluation of Demand Limiting Using Building Thermal Mass in a Small Commercial Building. *ASHRAE Transactions*.

Morris, F. B., Braun, J. E., & Treado, S. J. (1994). Experimental and Simulated Performance of Optimal Control of Building Thermal Storage. *ASHRAE Transactions*, 402-414.

Park, B., & Krarti, M. (2015). Development of a simulation analysis environment for ventilated slab systems. *Applied Thermal Engineering*, 66-78.

Pasupathy, A. V. (2008). Phase change material-based building architecture for thermal management in residential and commercial establishments. *Renewable and Sustainable Energy Reviews*, 39-64.

Peippo, K., Kauranen, P., & Lund, P. (1991). A multicomponent PCM wall optimized for passive solar heating. *Energy and Buildings*, 259-270.

Pomianowski, M., Heiselberg, P., & Lund Jensen, R. (2012). Dynamic heat storage and cooling capacity of a concrete deck with PCM and thermally activated building system. *Energy and Buildings*, 96-107.

Rabl, A., & Norford, L. K. (1991). Peak Load Reduction by Preconditioning Buildings at Night. *Intrernational Journal of Energy Research*, 781-798.

Raj, V., & Velraj, R. (2010). Review on Free Cooling of Buildings Using Phase Change Materials. *Renewable & Sustainable Energy Reviews*, 2819-2829.

Snyder, M. E., & and Newell, T. A. (1990). Cooling Cost Minimization Using Building Mass for Thermal Storage. *ASHRAE Transactions*.

Stetiu, C., & Feustel, H. E. (2014). Phase-change wallboard and mechnical night ventilation in commerical buildings. *Heat Transfer Engineering*.

Straube, J., & Burnett, E. (2005). *Building Science for Building Enclosures.* Wedford, MA: Building Science Press.

Sun, Y., Wang, S., Xiao, F., & Gao, D. (2013). Peak load shifting using different cold thermal energy storage facilities in commercial buildings: A review. *Energy Conversion and Management*, 101-114.

Thompson, K. D. (2011, October 28). *Space Conditioning Options for Energy Efficient Buildings.* Retrieved from National Institute of Standards and Technology: https://www.nist.gov/programs-projects/space-conditioning-options-energy-efficient-buildings

Turpenny, J., Etheridge, D., & Ray, D. (2000). Novel ventilation cooling system for reducing air conditioning in buildings. Part 1: testing and theoretical modeling. *ROOMVENT2000.* Reading, UK: Elsevier.

Ulgen, K. (2002). Experimental and theoretical investigation of effects of wall's thermophysical properties on time lag and decrement factor. *Energy and Buildings*, 273-278.

Xu, X., Zhang, Y., Lin, K., Di, H., & Yang, R. (2005). Modelling and simulation on the thermal performance of shape-stabilized phase change material floor used in passive solar buildings. *Energy and Buildings*, 1084-1091.

Zeng, R., Wang, X., Di, H., Jiang, F., & Zhang, Y. (2011). New Concepts and Approach for Developing Energy Efficient Buildings: Ideal Specific Heat for Building Internal Mass. *Energy and Buildings*, 1081-1090.

Zhang, Y., Lin, K., Zhang, Q., & Di, H. (2006). Ideal Thermophysical Properties for Free Cooling (or heating) Buildings with Constant Thermal Physical Property Material. *Energy and Buildings*, 1164-1170.

Zhuang, S. Z. (2015). Experimental study on the thermal response of PCM energy storage block with hole ventilation. *Advances in Materials Science and Engineering*.